



# LUND UNIVERSITY

## Studies of aerosol particle formation from various sources using ion and electron beam analytical techniques.

Gharibi, Arash

2006

[Link to publication](#)

### *Citation for published version (APA):*

Gharibi, A. (2006). *Studies of aerosol particle formation from various sources using ion and electron beam analytical techniques*. [Doctoral Thesis (compilation)]. LUND UNIVERSITY Lund Institute of Technology, Department of Physics, Division of Nuclear Physics, Box. 118, SE-22100 Lund, Sweden.

### *Total number of authors:*

1

### **General rights**

Unless other specific re-use rights are stated the following general rights apply:

Copyright and moral rights for the publications made accessible in the public portal are retained by the authors and/or other copyright owners and it is a condition of accessing publications that users recognise and abide by the legal requirements associated with these rights.

- Users may download and print one copy of any publication from the public portal for the purpose of private study or research.
- You may not further distribute the material or use it for any profit-making activity or commercial gain
- You may freely distribute the URL identifying the publication in the public portal

Read more about Creative commons licenses: <https://creativecommons.org/licenses/>

### **Take down policy**

If you believe that this document breaches copyright please contact us providing details, and we will remove access to the work immediately and investigate your claim.

LUND UNIVERSITY

PO Box 117  
221 00 Lund  
+46 46-222 00 00

# Studies of aerosol particles formation from various sources using ion and electron beam analytical techniques

Arash Gharibi



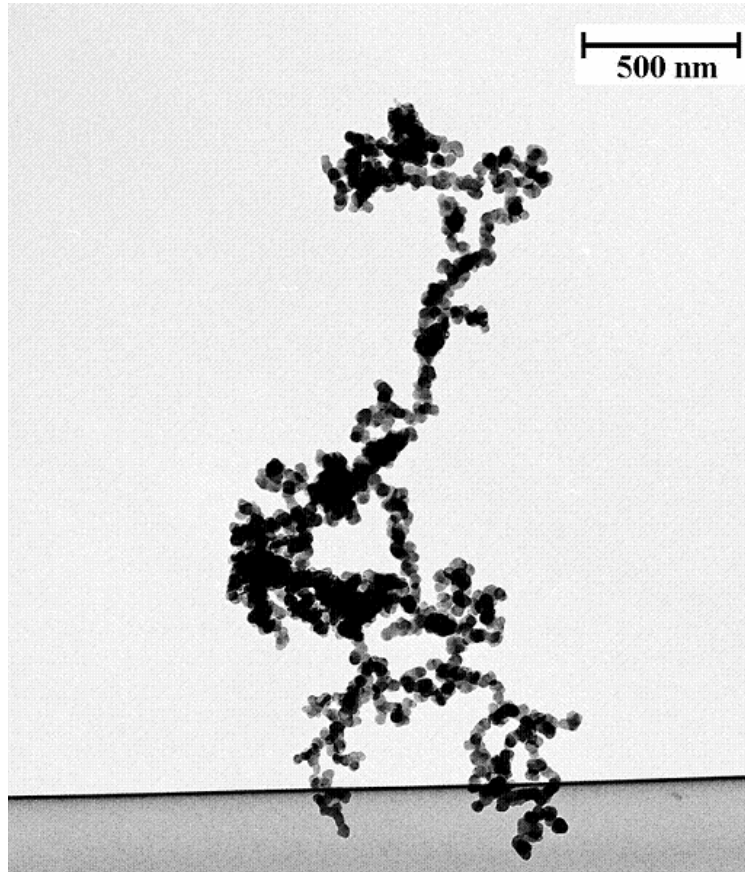
LUND INSTITUTE  
OF TECHNOLOGY  
Lund University

Doctoral Thesis  
Department of Physics  
Division of Nuclear Physics

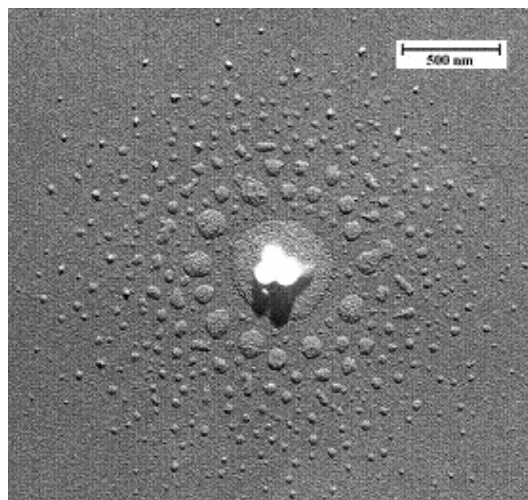
Lund, March 2006

What is on the cover?

A TEM image of aerosol particles produced by a kerosene lamp (a view from above). The agglomerate stretches out horizontally supporting itself on the edge of the carbon film (the dark part of the photo). This complex agglomerate is formed of soot particles 30-40 nm in size.




A group of 3 angular electron-dense particles (white) surrounded by a sulfuric acid halo.



<b>Organisation</b> LUND UNIVERSITY Lund Institute of Technology Department of Physics Division of Nuclear Physics Box. 118 SE-22100 Lund	<b>Document name</b> DOCTORAL THESIS	
	<b>Date of issue</b> <b>March, 2006</b>	
	<b>CODEN</b> LUTFD2 / (TFKF-1031) / 1-130 / (2006)	
<b>Author(s)</b> Arash Gharibi	<b>Sponsoring organization</b>	
<b>Title and subtitle</b> Studies of aerosol particle formation from various sources using ion and electron beam analytical techniques.		
<b>Abstract</b> - The thesis presents the results of studies of aerosol particle formation using ion and electron beam analytical techniques. The sources of aerosol particle formation studied are the following: <ol style="list-style-type: none"> <li>1. production of primary aerosol particles in the high Arctic region during summers</li> <li>2. emission of ultrafine aerosol particles from wear on the road-tire interface</li> <li>3. emission of aerosol particles from district heating units operating on three commonly-used biofuels.</li> </ol> <p>A source of primary and nearly hydrophobic aerosol particles within the Arctic pack ice region during summers with a composition similar to that of average crustal rock was identified.</p> <p>Wear on the road-tire interface was found to generate numerous ultrafine aerosol particles of varying morphology. The particle number emission factors per vehicle and kilometer driven are similar in magnitude to the tail-pipe exhaust emissions obtained by use of modern engine technology.</p> <p>Particle emissions from the combustion of biomass were characterized in terms of their elemental composition and particle formation mechanisms.</p>		
<b>Key words</b> Aerosol particles, sources, emission, PIXE, GUPIX, TEM, SEM, EDX, biomass combustion, Arctic, traffic, tire, road, jet droplets, film droplets.		
<b>Classification system and/or index terms (if any):</b>		
<b>Supplementary bibliographical information:</b>	<b>Language</b> English	
<b>ISSN and key title:</b>	<b>ISBN</b> 91-628-6757-1	
<b>Recipient's notes</b>	<b>Number of pages</b> 130	<b>Price</b>
	<b>Security classification</b>	

**Distribution by (name and address):** Department of Physics, see address above.

I, the undersigned, being the copyright owner of the abstract of the above-mentioned dissertation, hereby grant to all reference sources permission to publish and disseminate the abstract of the above-mentioned dissertation.

Signature Arash Gharibi 

Date: March 3, 2006



## ***Dedication***

*I dedicate this work to all children of the world especially my daughter Setare.  
I hope one day the world is clean environmentally and psychologically. Until then I  
share the 2003 Peace Nobel Winner Shirin Ebadi's wish.*



*A peace, which covers all children of the world, is my wish. (English)*

*En fred, som innefattar alla barn i världen, är min dröm. (Swedish)*

*Η ευχή μου είναι ειρήνη για όλα τα παιδιά του κόσμου. (Greek)*

*Mi deseo, una paz, que cubra a todos los niños del  
mundo. (Spanish)*

*Taika yra tai ko norečiau visiems vaikams pasaulyje. (Lithuanian)*

*Que todas as crianças do mundo tenham paz, esse é o meu  
desejo. (Portuguese)*

Пусть всегда будет солнце,  
Пусть всегда будет небо,  
Пусть всегда будет мама,  
Пусть всегда буду я.

**(Л. Ошанин, Russia)**

*Моя мечта – мир детям всего мира. (Russia)*

*Egy, a világ összes gyermeke számára elérhető béke a  
vágyam. (Hungarian)*

*Je souhaite la paix pour les enfants du monde  
entier. (French)*

*Uoc nguyen cua toi la "hoa binh den voi tre em tren toan the gioi". (Vietnamese)*

*和平，遍及世界上所有儿童的和平，是我的愿望 (Chinese)*

*Dass Friede sei mit allen Kindern dieser Erde, ist mein innigster Wunsch.(German)*

*Rauha, joka kattaa kaikki maailman lapset, on toiveeni.(Finnish)*

*世界中の子供たちに平和を！ それが私の願いです。(Japanese)*

## Table of contents

Chapter 1 .....	3
Introduction .....	3
1.1 Aerosols and climate .....	5
1.2 Aerosols and health .....	7
1.3 Aerosol particles produced by combustion .....	8
1.4 Aerosol particles produced by tire wear.....	10
1.5 Aerosol particles produced in the Arctic Ocean .....	11
1.6 Aim and outline of this work .....	13
Chapter 2 .....	15
Applied analysis methods (Electron Microscopy) .....	15
2.1 Scanning Electron Microscopy (SEM) .....	15
2.2 Transmission Electron Microscopy (TEM) .....	16
2.3 PIXE .....	18
2.4 The Lund Nuclear Microprobe Laboratory (NMP) .....	18
Chapter 3 .....	25
Sampling techniques for the aerosol particles studied.....	25
Chapter 4 .....	28
Chemical tests on collected aerosol particles.....	28
4.1 Wet test.....	29
4.2 Sulfate test: .....	29
4.3 Vapor tests:.....	30
4.4 Biological material: .....	31
4.5 Simple hydrocarbons:.....	31
4.6 Aromatic compounds: .....	31
4.7 Heat sensitivity:.....	31
4.8 Limitation to the wet chemical tests: .....	33
Chapter 5 .....	34
Supporting films for TEM analysis.....	34
5.1 To make Formvar supported grids .....	34
5.2 To make Carbon supported grids .....	35
5.3 To make Combination supported grids .....	35
Chapter 6 .....	36
6. Results and Conclusions .....	36
Acknowledgements.....	43
References.....	45
<b>Paper I:</b> .....	47
<b>Paper II:</b> .....	75
<b>Paper III:</b> .....	91

<b>Paper IV:</b> .....	102
<b>Paper V:</b> .....	115

# Chapter 1

## Introduction

There has been broad interest in research on aerosol particles, particularly because of the risk to the health of the earth's population and ecosystem that they represent.

An aerosol is a suspension of solid or liquid particles in a mixture of gases, normally air (Hinds, 1998). Aerosol particles are complex mixtures of many different chemical species originating from a variety of sources. The physical, compositional, morphological and thermodynamic properties of aerosol particles vary with the geographical area and with the season of the year (Finlayson-Pitts and Pitts, 1986).

Observations of aerosol particles can only be made if the time they remain suspended is sufficiently long. This limits the size of the aerosol particles that can be studied to the diameter range of roughly 1 nm to 100  $\mu\text{m}$ . Particles close to the lower limit represent thermodynamically stable clusters, whereas those close to the upper limit represent particles with a lifetime of reasonable length with respect to gravitational settling.

Particles generated by combustion processes, such as those produced by traffic emissions or by biomass burning, are in a size range of about 0.003  $\mu\text{m}$  to 2  $\mu\text{m}$  generally, although for particles originating from biomass burning the upper limit may be slightly higher than this. Also, soil dust is composed of particles most of which are larger than 2  $\mu\text{m}$ , and fly ash from coal combustion involves aerosol particles about 0.1 to 50  $\mu\text{m}$  in size.

Aerosol particles in the atmosphere undergo changes in their chemical composition and size, due mainly to the following physical and chemical processes:

- nucleation (formation of new particles)
- condensation
- evaporation
- coagulation
- wet and dry deposition

The air we breathe is an aerosol. The particle concentrations in urban air are typically  $\sim 10^5$  particles·cm<sup>-3</sup> of air. In Arctic air, concentrations as low as 10 cm<sup>-3</sup> are not uncommon during the summers. Aerosol particles vary in size, shape and chemical composition. Figure 1 shows the different size modes found in most atmospheric aerosols.

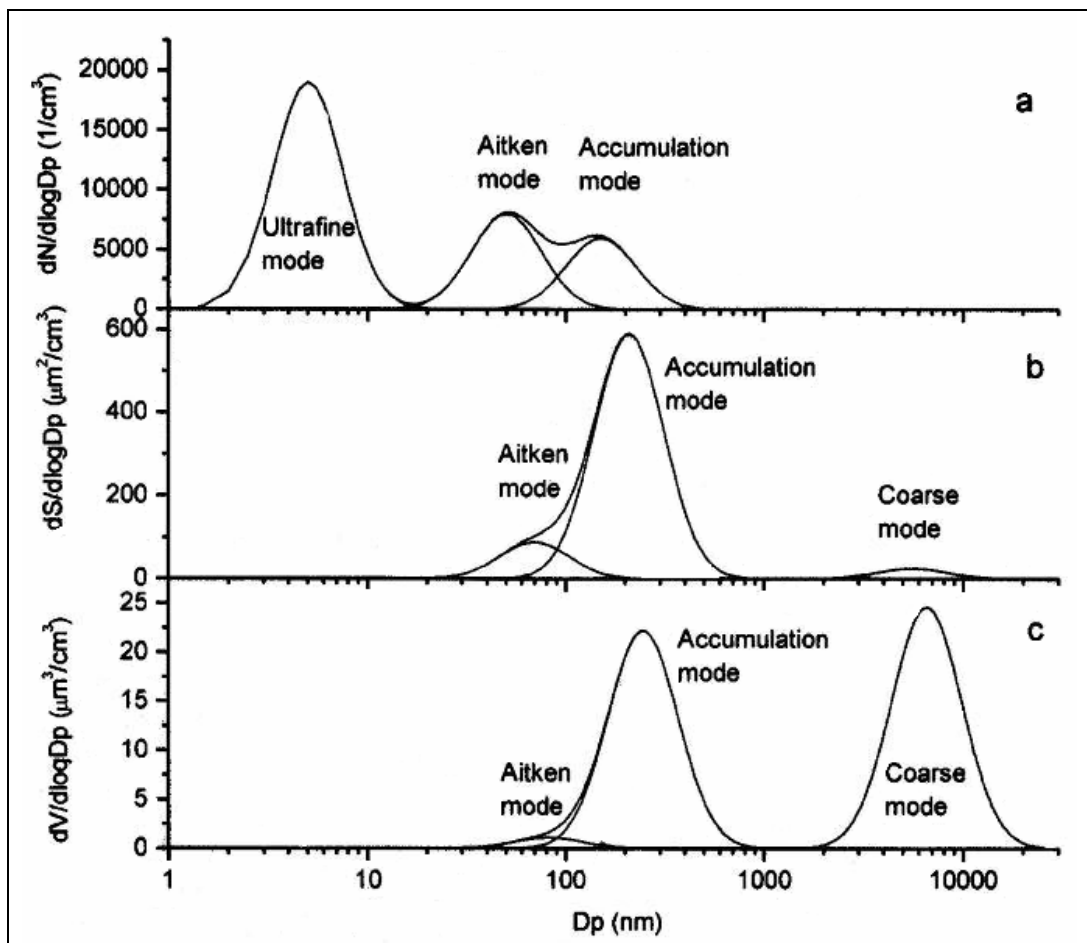


**Figure 1.** Example of a) an aerosol particle-number distribution, b) the corresponding surface distribution and c) the volume distribution.

## 1.1 Aerosols and climate

Aerosols are formed in different ways. One is by the emission of primary aerosol particles directly into the air at the source itself. Another is the formation of secondary aerosol particles (or secondary aerosol particle mass) in the air from condensable vapours. Aerosol particles are composed mostly of inorganic salts, crustal material, soot, organic compounds, metals and water. They are produced through both natural processes and human activities. Most aerosols from natural sources are spread around the globe, whereas aerosol particles from man-made sources are concentrated to industrialised and densely populated areas. Aerosol particles affect both the climate and the environment through many different processes. Atmospheric aerosols affect the climate in two major ways. One of these is through the direct effect of aerosol particles in scattering sunlight (short-waves) back into space, which affects the global radiation balance. This increases the earth's albedo and has a net cooling effect on the climate, an effect estimated to be comparable to the warming due to greenhouse gases (IPCC, 2001). Figure 2 shows a comparison of the radiative forcing effects of greenhouse gases to those of aerosols. A second way in which aerosols affect the climate, through their indirect effects, is related to the modification of cloud and fog droplet characteristics. When the relative humidity exceeds a certain level, aerosol particles are able to take up water and grow to become droplets, which results in cloud or fog formation. Aerosol particles which are able to do this are called Cloud Condensation Nuclei (CCN).

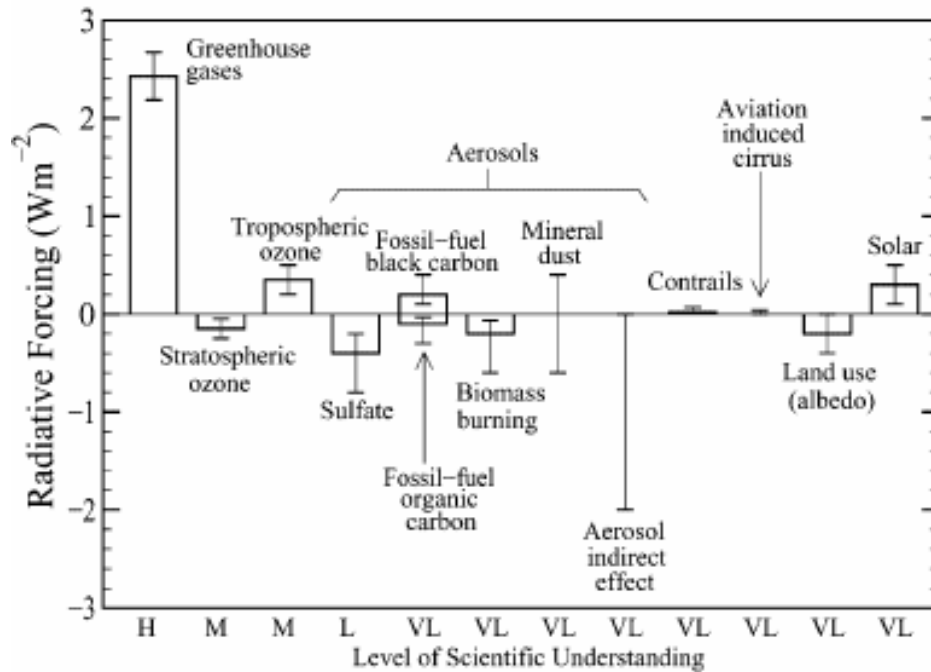


**Figure 2.** Global annual-mean radiative forcing effects ( $\text{W m}^{-2}$ ) due to a number of different agents, from pre-industrial (1750) to present (late 1990s, ~2000) times. H, M, L, and VL are the different LOSU (Levels of Scientific Uncertainty), where H=high, M=medium, L=low and VL=very low (Boucher and Haywood 2001).

Clouds reflect sunlight back into space and can stop infrared radiation emitted by the earth. In addition, clouds transport water from the atmosphere to the earth's surface through precipitation (e.g. rain and snowfall). In this way, aerosol particles have an impact on the earth's radiation balance and hydrologic cycle (an indirect effect) (Seinfeld and Pandis, 1998). There is also homogeneous nucleation which is believed to be responsible for the occurrence of new particle formation in clean environments in which the background aerosol particle concentrations are low. The indirect effects are more difficult to understand than the direct effects since the physical and chemical processes involved are highly complex.



## 1.2 Aerosols and health

It has long been documented that air pollution affects human well-being. Many recent investigations (summarized in WHO, 2003) have shown there to be a connection between increased mortality rates due to respiratory and cardiovascular diseases and increases in PM10 concentrations (i.e. the mass concentration of particles of an aerodynamic diameter  $< 10 \mu\text{m}$ ) (See Figure 4 below).

The coarse and the fine aerosol particle fractions differ completely in their characteristics and their potential influence on health. Large particles can gather in the upper parts of the human respiratory tract and cause health problems such as asthma. Fine particles can penetrate deeply into the alveolar region of the respiratory tract and are more likely to cause acute health problems.

The impact of aerosol particles on health can be divided in two categories:

- Short-term effects
- Long-term effects

The symptoms associated with short-term effects are those of asthma and bronchitis, whereas the symptoms of the long-term effects are chronic irritation of the respiratory tract and the development of lung cancer. The fact that aerosol particles have a negative effect on health and can greatly reduce our overall quality of life makes atmospheric aerosol research highly important. There is a need of gaining a better understanding of aerosol particles less than  $10 \mu\text{m}$  in size in terms of their impact on both morbidity and mortality rates.

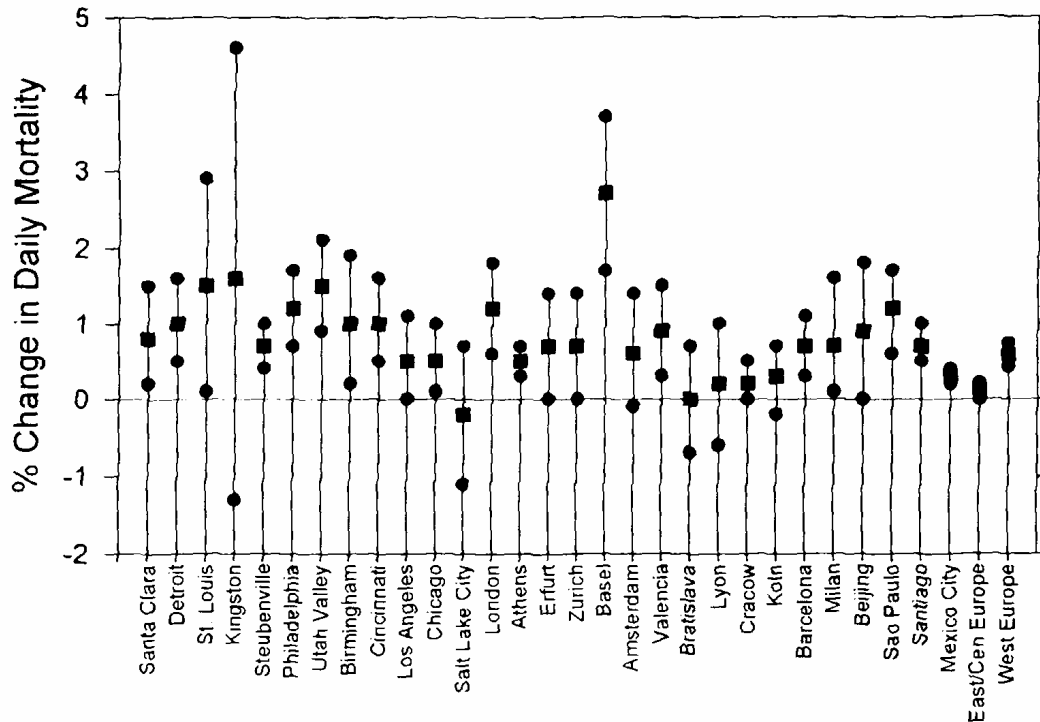


**Figure 3.** Estimated percentage-wise changes in daily mortality rates associated with a  $10 \mu\text{g m}^{-3}$  increase in PM<sub>10</sub> (together with 95% confidence intervals) for various cities (Pope and Dockery, 1999).

### 1.3 Aerosol particles produced by combustion

Combustion is a dominant energy source in our daily lives and in society generally. Common examples of energy conversion of this sort include the action of domestic burners, of car engines, and of industrial furnaces. Despite the continuing search for alternative energy sources, combustion still supplies more than 95 % of the energy consumed in the world. In addition, combustion is a source of the air pollution caused by the emission of soot, PAH, a toxic pollutant that produces smog and acid rain (Griffith and Barnard, 1995).

Biomass burning produces both particulate matter and various gases. The particulate matter containing carbons represents what are called carbonaceous aerosols (with the exception of carbonates). Carbonaceous aerosols are divided into two categories:

1. elemental carbon (EC )(also called "black carbon" BC or soot)
2. organic carbon (OC)

Elemental carbon is emitted as a result of the incomplete combustion of fossil and biomass fuels. Organic carbon, the most abundant carbonaceous aerosol species, can be emitted into the atmosphere directly in the form of particles through combustion, or can be produced in the atmosphere as a result of the gas-to-particle conversion of anthropogenic and biogenic hydrocarbons (Seinfeld and Pandis 1998). Examples of human activities that result in biomass burning are

- agriculture activities: burning of agriculture wastes, burning of forests to increase the areas of land available for agriculture, etc.
- cooking and heating.

It is generally believed that by far the greatest part (>90%) of biomass burning is initiated by humans and that it has increased considerably over the last 100 years.

District heating units operating on solid biofuels produce two fly ash fractions: coarse fly ashes and fine aerosol particles. These two fractions differ considerably in their particle size and their chemical composition, as well as in the mechanisms involved in their formation. Both coarse fly ashes, which are particles deriving from the fuel bed, and smoke gases consist mainly of refractory species. Their particle size varies between 2 and 100  $\mu\text{m}$ . The formation of fine aerosol particles in biomass burning is more sophisticated than the formation of coarse fly ashes. During the combustion process, it involves a part of the volatile compounds, such as alkali metals, S, Cl and heavy metals, being released from the fuel to the gas phase and undergoing homogeneous gas-phase reactions. The combined particle size distribution of coarse fly ashes and fine aerosol particles results in the

typical bimodal particle-size distribution of particulate emissions from solid fuel combustion processes (Strand 2004).

The increasing effects on the regional and global atmospheric chemistry, as well as on the energy budget of the earth, of the pollution produced by the burning of biomass and of fossil fuels will no doubt be a highly important issue in the future.

## **1.4 Aerosol particles produced by tire wear**

The particulate matter produced by motor vehicles originates mainly from the combustion of hydrocarbons and the wear on tires, brakes, and the road surface (*Camatini 2001*). Car tires are composed of many different materials that form the overall product, steel wire and nylon fibers being two of them, (*Kohls Beaucage 2002*). The main ingredients of car and truck tire treads are elastomers and additives. The elastomers, used in both the treads and the sidewalls of tires, represent a solution and an emulsion of styrene-butadiene rubber, natural rubber, and blends of these, and are usually composed of carbon and silica. The additives used, which include reinforcements, fillers, vulcanisers, accelerators, activators, antioxidants, and softening fillers, serve to increase the strength, wear resistance, overall performance, and processing of the rubber. As one can see, the combining of all these materials results in a final product very complex in its structure and rather complex in its properties. In addition, the processing of these materials affects the properties of the final products. Having more detailed knowledge of the size, shape, microstructure, and constituents of tire wear will help to eventually control and improve the tire manufacturing process and in estimating the potential impact of the aerosol particles produced on human health and on the environment (*Camatini 2001*).

## 1.5 Aerosol particles produced in the Arctic Ocean

Arctic aerosol particles are characterized by very low mass concentrations. It has been found that during the winter and spring the Arctic aerosol particles are influenced considerably by anthropogenic sources, leading to the formation of an Arctic haze and an increase in the mass concentrations of the type of aerosol particles producing it. The aerosol particles creating arctic haze are often of considerable age and contain carbonaceous material from pollution sources in the middle latitudes, together with sea salt and mineral material.

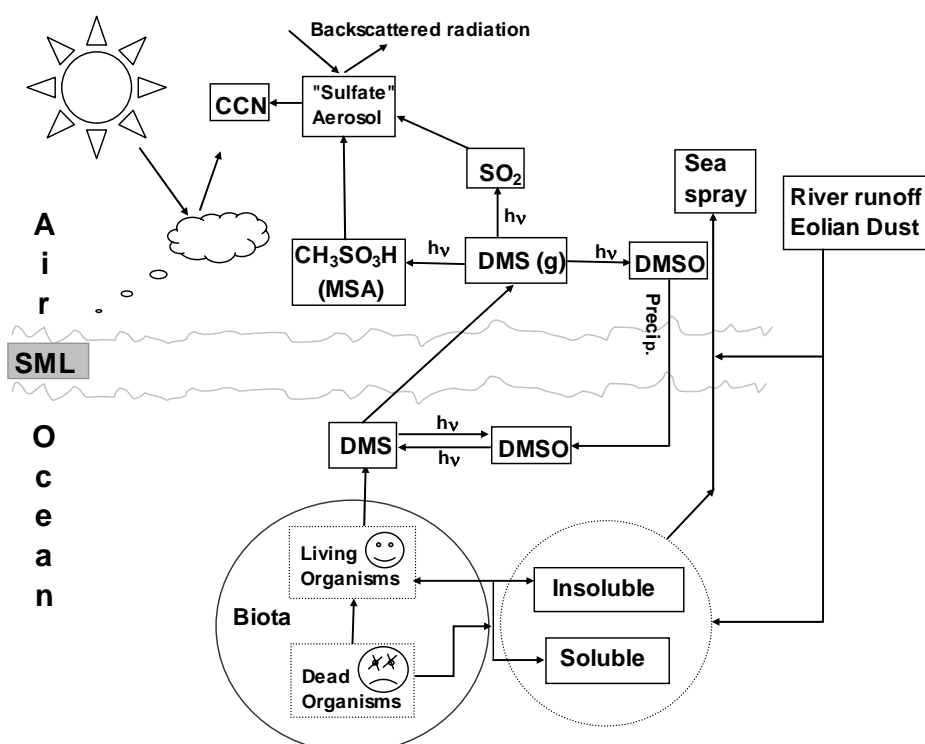


Figure 4. A schematic diagram of the air-ocean interaction. SML: surface microlayer. DMS: dimethyl sulfide. DMSO: dimethyl sulfide oxide. CCN: Cloud Condensation Nuclei. Taken from Stuart Ross Taylor and Scott M. McLennan and modified.

The direct radiative effects of aerosol particles produce a surface warming, whereas their indirect radiative effects lead to a surface cooling. In the high Arctic regions there is no simple relationship between the concentration of aerosol particles and their radiative effects. The interactions between clouds, aerosol particles, and the climate appear to be more complex in such high-latitude regions as the Arctic than in other parts of the earth.

The interactions between the air and the ocean are shown in figure 4. The paths of particulate matter from the ocean to the atmosphere and vice versa are shown by arrows. As indicated in the figure, the major sources of the particles contained in seawater are oceanic biota and the input from river runoff and from eolian dust.

River runoff (such as in the Siberian area) brings crustal material into the Arctic Ocean, where it is frozen into the ice and is transported across the Pole by the transpolar current. During the Arctic summer, this ice melts and drops the crustal material into the sea water and into the surface microlayer (SML). The crustal material then becomes available in both the sea water and the surface microlayer. If these particles subsequently become airborne, their surface also becomes available to the surrounding gases to condensate on them.

The extent to which the trace elements are processed then by the Arctic oceanic biota is unclear. This is certainly the case for Si, which dissolves in seawater as silicic acid and is taken up by diatoms and other organisms. The extent to which crustal material provides a source of nutrients and of primary particles, this possibly constituting a feedback mechanism for climatic changes that occur over various land areas, needs to be better understood.

A NASA ice physicist, Josefino Comiso, predicts that the Arctic Ocean will be completely emptied of summer ice before the end of the present century. A study of hers (Comiso, 2002) shows for the perennial ice cover of the ocean over the North Pole that the amount of ice surviving through the warm summer months is diminishing far more rapidly than earlier. Between 1978 and 2000, 1.2 million square kilometers of permanent ice melted away. This is a loss of nine percent per decade. Research on the composition and the sources of aerosols in the high Arctic region is thus highly important for gaining a better understanding of the environment and for possibly being able to manage it better.

## **1.6 Aims and outline of this work**

The thesis concerns the effects of aerosol particles both on global climate and on human health. More specifically, three particular types of aerosol particles, important to either climate or human health or to both, are studied.

These are

1. Aerosol particles in the High Arctic during the summers;
2. Traffic-generated aerosol particles, more specifically wear particles from the road-tire interface in the sub-micrometer size range;
3. Aerosol particles emitted during the combustion of biomass.

The key scientific questions to which answers were sought in the projects for which I shared responsibility were the following:

- What are the sources of aerosol particles for the high-Arctic boundary layer (ABL) during the summers, with regards both to particles numbers and to particle mass?
- What processes affect the elemental mass concentrations of the ABL?
- What processes are responsible for the generation of particles in the sub-micrometer size range through wear at the road-tire interface?
- How are the properties of the aerosol particles that are emitted during the combustion of biomass affected by the combustion conditions and the fuel that is burnt?

These scientific questions were not resolved solely on the basis of studies of the elemental composition and particle morphology, but the results obtained through implementing these analytical techniques do provide important information which, when complemented by other aerosol and auxiliary data, contributed to a considerable degree to the conclusions that were drawn.

The aim of the atmospheric program of the Arctic Ocean Expedition 2001 was to study sources of airborne particles over the highly remote Arctic Ocean and the climatic relevance of these particles. The results of this project are presented in papers I and II,

which cast light on the sources of aerosol particles in the Arctic during the summers and provide information of a unique character enabling one to better understand the role aerosol particles play in influencing both global climate and human health. The data obtained in the Arctic Project is extremely important since very little data of this nature from latitudes as high as this is available. Until now, there have been only three expeditions to this area that have dealt with questions of this sort.

The Swedish National Road and Transport Research Institute (VTI) was the coordinator of the WearTox project (Gustafsson, 2005). The aims of that project were to study particles from the studded and non-studded tire wear of pavements.

In paper III a characterization of the wear particles originating from the road-tire interface is aimed at. The properties of wear particles in the size range of 15-50 nm are also studied. The toxicological effects these particles have on human health are also taken up.

Measurements presented in papers IV and V were part of the Swedish research program BHM (Swedish: Biobränsle – Hälsa – Miljö; or Biofuels – Health – Environment), especially the project within that program dealing with emissions and air quality (Noone, 2005). The BHM program aims at studying the effects that the increased utilization of biofuel combustion for energy production has on the environment and on human health. Papers IV and V aim at contributing to an understanding of aerosol formation mechanisms and aerosol emissions.



## Chapter 2

### Applied analysis methods (Electron Microscopy)

It was not until well into the 20th century that a better resolution for electron microscopes than the light microscopes could be achieved. This involved employing a source of illumination with a much shorter wavelength than attainable by conventional light microscopes. Electrons, discovered by the British physicist J.J. Thompson, in 1898, were shown by L. deBroglie in 1924 to possess a wavelength nearly a thousand times shorter than that of visible light. The work of such physicists as H. Busch and E. Ruska during the period of 1925 to 1934 led to the development of strong electromagnetic lenses that enabled electron beams to be focused in much the same way as glass lenses direct the pathway of visible light. In fact, the basic design of early transmission-electron microscopes involved use of optical pathways similar to those of light microscopes, which is true of today's instruments as well (M.J. Dykstra 1992).

#### 2.1 Scanning Electron Microscopy (SEM)

A specimen can be scanned effectively by an electron beam (Scanning Electron Microscopy, SEM) through use of strong electromagnetic lenses. An electronic signal is obtained which reveals either the quantity of electrons reflected from the surface or the amount of excited electrons generated from deeper within the specimen. When an incident electron beam hits the atoms of a sample, the sample generally emits the following signals:

- Characteristic X-rays
- Auger electrons
- Bremsstrahlung
- Secondary electrons
- Visible light
- Back-scattered electrons
- Inelastic transmitted electrons

The X-rays emitted from the atoms of the sample are characteristic for the level of energy they possess, which corresponds to that of the element to which the parent atoms belong. The method utilizing this principle is usually referred to as Energy-Dispersive X-ray Spectroscopy **EDX**, the term **EDS** sometimes being used as well. X-rays are formed there by interaction of the electron beam with the sample surface, the sample that is thus imaged being analyzed. This enables SEM to perform elemental analysis in very small areas, such as  $< 1 \mu\text{m}^2$ .

## **2.2 Transmission Electron Microscopy (TEM)**

Before details of how a transmission electron microscope (TEM) works are considered, the matter of why it works at all needs to be clarified. It is not entirely obvious that by passing a beam of electrons through a thin sample an image of the particles within it can be obtained (Chescoe and Goodhew, 1990).

Figure 6 shows what basically happens to electrons when striking four different regions of a model specimen, 100 electrons being involved in each case. Region (A) consists of 10 nm thick amorphous carbon. This target produces a weak scattering of the electrons due to carbon being a light atom. Approximately 10% of the electrons are deflected  $0.5^\circ$  or more, almost none of them being likely to be deflected more than a few degrees. Since region (B) is twice as thick as region (A), it scatters the electrons to a somewhat greater extent. Region (C) is of the same thickness as (B) but consists of amorphous lead, which is a very heavy atom.

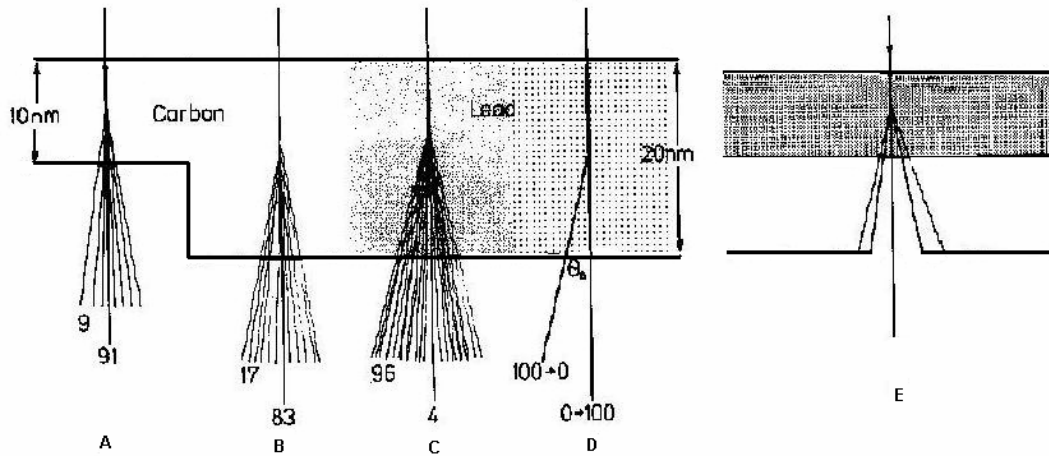


**Figure 6.** The fate of electrons, 100 in each case, falling on four different regions of a hypothetical specimen. The number at the left in each case shows how many are scattered more than  $0.5^\circ$  and the number at the right how many are unscattered or are scattered less than this. The regions are as follows: (A) 10 nm of amorphous carbon; (B) 20 nm of amorphous carbon; (C) 20 nm of amorphous lead and (D) 20 nm of crystalline lead. (E), in turn, shows the effects of inserting an objective aperture to stop all electrons scattered more than about  $0.5^\circ$  (Reproduced from Chescoe and Goodhew, 1990.)

Thus, the majority of electrons are deflected, although the scattering angle is still small. Since region (D) consists of crystalline rather than amorphous lead, diffraction takes place there, the scattered electrons traveling in various directions at twice the Bragg angle  $\theta_B$ , the numbers of electrons emerging from the specimen in the unscattered and in the diffracted beams, respectively, being strongly dependent upon the orientation and the thickness of the specimen, their ranging in the individual case anywhere from very close to zero to 100.

If all these (100) electrons were allowed to contribute to a TEM image, there would be no contrast between areas of differing thickness or composition. No contrast means there being no image of the specimen. In order to achieve an image contrast, all the electrons scattered more than  $\sim 0.5^\circ$  are blocked by an objective aperture, as shown in figure 6E (Chescoe and Goodhew, 1990).

## **2.3 PIXE**

The elemental composition of aerosol particles can be analyzed by use of PIXE (Particle Induced X-ray Emission). When samples are bombarded with protons, the protons can eject inner-shell electrons from the atoms of the sample to create vacancies (Johansson and Campbell, 1988). These vacancies become filled by outer-shell electrons, giving rise to X-rays characteristic of the elements from which they originate. PIXE, which was first introduced in 1970, at the Lund Institute of Technology (Johansson et al., 1970), has the following properties and capabilities:

- Non-destructive analysis of solid samples.
- Simultaneous determination of most of the elements involved ( $Z > 12$ ) and its possessing very low detection limits for these.
- Its being suitable, because of its high sensitivity, for the elemental analysis of aerosol samples, biological samples and thin-film samples.

## **2.4 The Lund Nuclear Microprobe Laboratory (NMP)**

The PIXE analyses were conducted in the Lund NMP (Nuclear Microprobe) facilities, equipped with an electrostatic single-ended accelerator of the NEC 3UDH type. The accelerator provides proton beams of three different sizes - a MACRO, a MICRO and a NANO beam - the MACRO line being largest and the NANO line smallest. The MACRO beam is designed to be used for the analysis of aerosol samples. It is represented by the line at the left in figure 7.

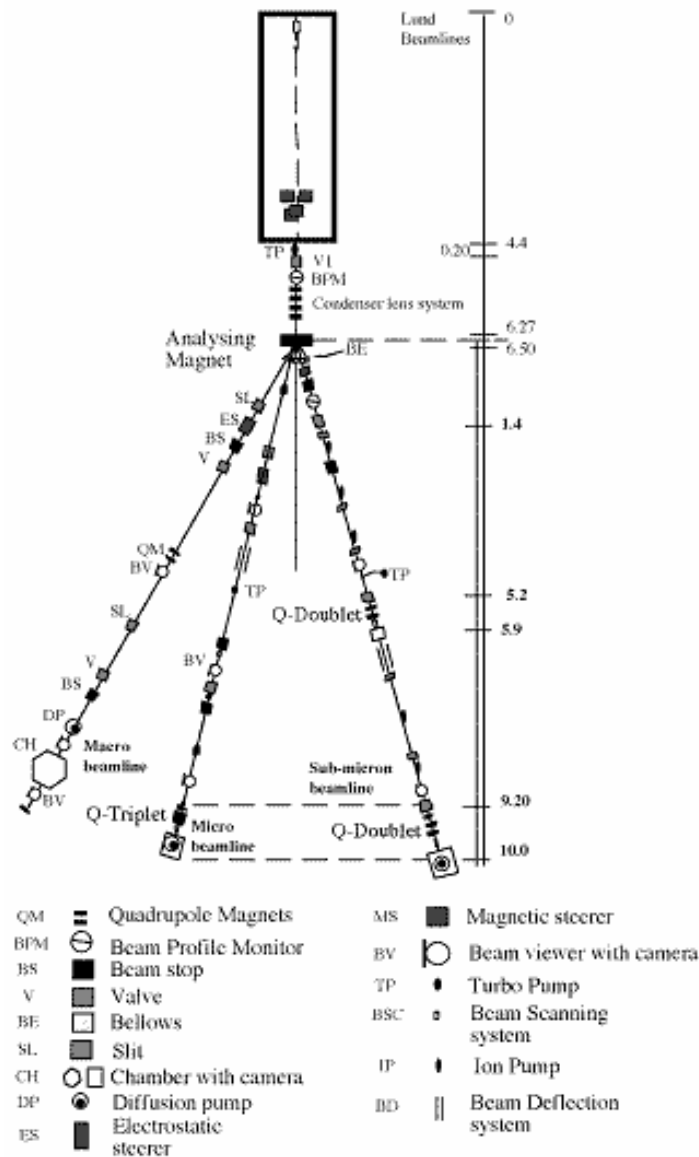


**Figure 7.** Schematic layout of all the beam lines at the Lund NMP laboratory, from left to right the MACRO, MICRO, and NANO beam lines being shown (adopted from Elfman, 2001).

Prior to each experiment, adjustment of the linearity, offset and drift of the beam line chosen is necessary. In addition, the accuracy and precision of the data acquisition system need to be checked. For analyzing aerosol samples, use of a homogenous proton beam is desirable. This can normally be produced by means of quadrupole magnets and collimation of the proton beam in several steps. Having a

well-defined proton beam spot (e.g. one with sharp edges) on the target requires that the collimators be arranged in such a way as to minimize the slit scattering and avoid a beam-spot halo. Two collimators that differed slightly in the diameter of their conical opening were used to achieve this. In figure 8 this arrangement is designated as “collimator pairs”.

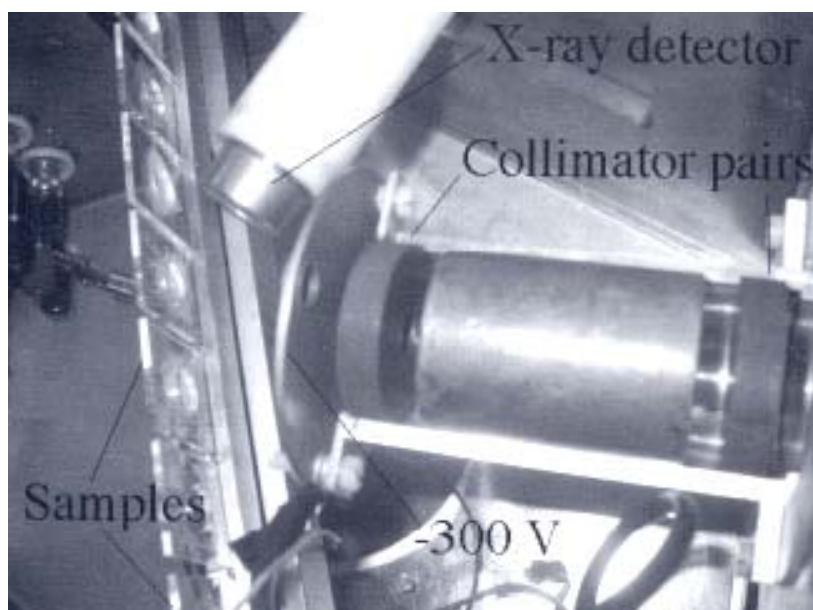


**Figure 8.** View from above of the experimental chamber located on the MACRO beam line. The beam enters from the right through the collimator system (adopted from Shariff, 2004).

It is extremely important that the generation of unwanted X-rays and  $\gamma$ -ray background in the chamber through the interaction of the protons with the material around be minimized, especially in the vicinity of the X-ray detector.

The yield of the characteristic X-ray line created by the passage of protons through a thin target is given by

$$Y_0 = k(Z)N_p M_a(Z) \quad (1)$$

where  $k(Z)$  is the degree of so-called thin-target sensitivity,  $M_a(Z)$  is the mass of the target per beam area ( $S$ ),  $Z$  is the atomic number, and  $N_p$  is the number of incoming protons. The units of  $k(Z)$  are X-ray counts per proton (or per unit of the charge) per  $\mu\text{g}/\text{cm}^2$ . The units for  $M_a(Z)$  are mass per unit area. Equation (1) is independent of whether the beam area,  $S$ , covers the specimen or vice versa (Johansson, S.A.E and J. L. Campbell 1988). See also figure 9 below.

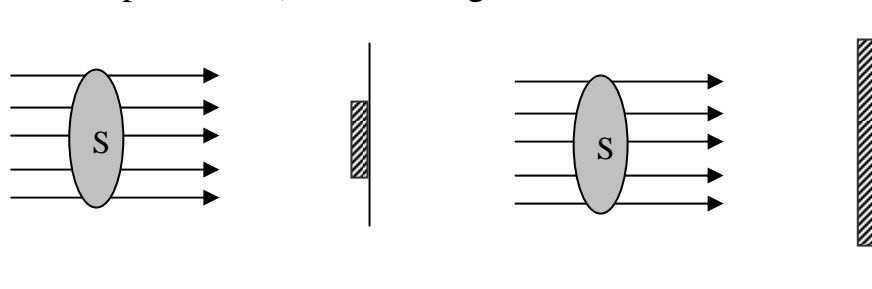


**Figure 9.** Different relationships between the beam area,  $S$ , and the specimen: that of the sample area being smaller than the cross section of the beam (left) and that of the target area being larger than the cross section of the beam (right) (Johansson and Campbell, 1988).

Measurement of the beam current in the macro-chamber is done by dumping the beam in a Faraday cup placed at the far end of the beam line, collecting the charge and using the result obtained to calculate  $N_p$ .

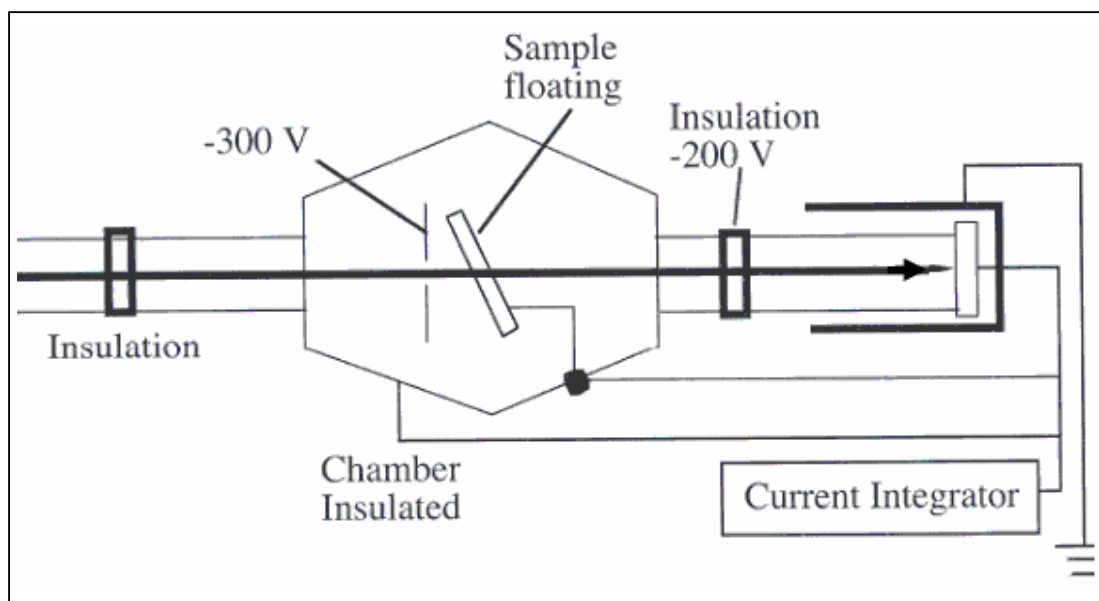


**Figure 10.** Schematic illustration of the arrangement for measuring the charge on the macro beam line (adopted from Shariff, 2004)

Before starting the experiment, one needs to verify that the electronics in its entirety works properly. This is done by use of a reference test to analyse the ratio of the peak area of Al to that of Fe in a standard sample. The linearity can be investigated by calculating the ratio of the peak area to the total charge (Q) on both elements (Al and Fe) for different beam currents.

The X-rays create high-energy electrons in the detector material by means of a photoelectric effect, these in turn, after several steps, creating electron-hole pairs. The Ge-crystal as a whole is part of a closed electric circuit in which the high voltage ( $\sim 1$  kV) provided makes the crystal behave as a reversed biased-pn-junction. The electric field of about 2kV/cm in the crystal causes electrons and holes to quickly move out and a charge to be released. The charge released is proportional to the number of incoming X-rays. The pre-amplifier is integrated with the detector and is connected to a spectroscopy amplifier.



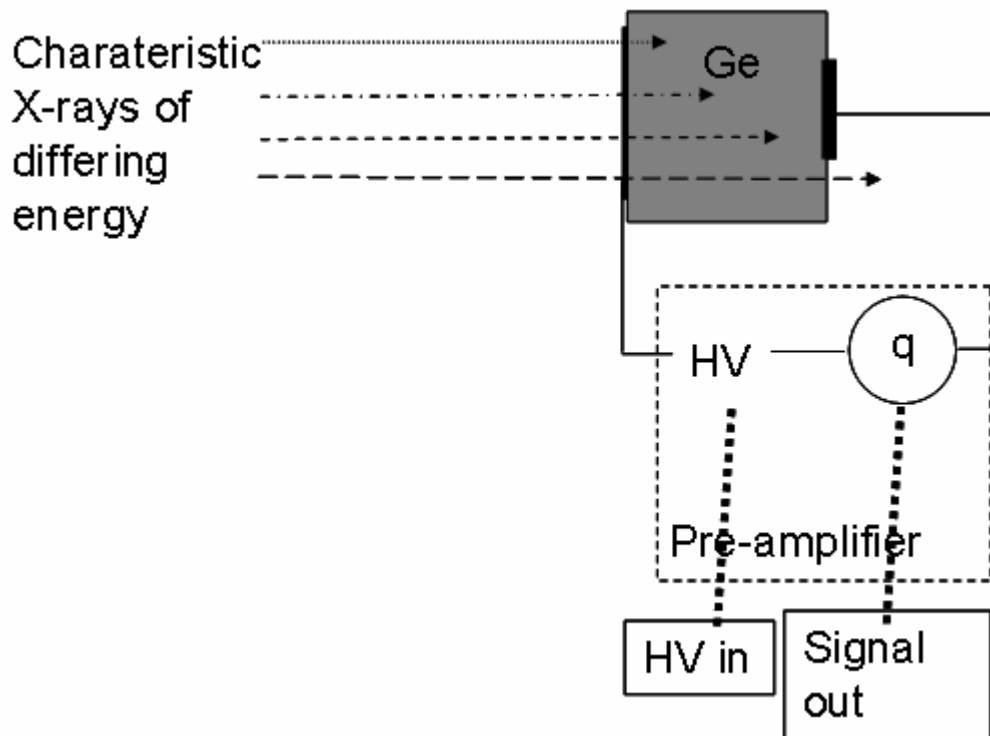


**Figure 11.** A simple schematic view showing the principles of operation of a semiconductor detector (Ge) (Pallon, 2005).

The degree of absorption of X-rays by the detector materials (e.g. Ge) is dependent upon the energy, low-energy photons being absorbed near the entrance and high-energy photons being partly transmitted (see figure 11). The X-ray spectra can be converted to elemental concentrations by use of a software package such as GUPIX.

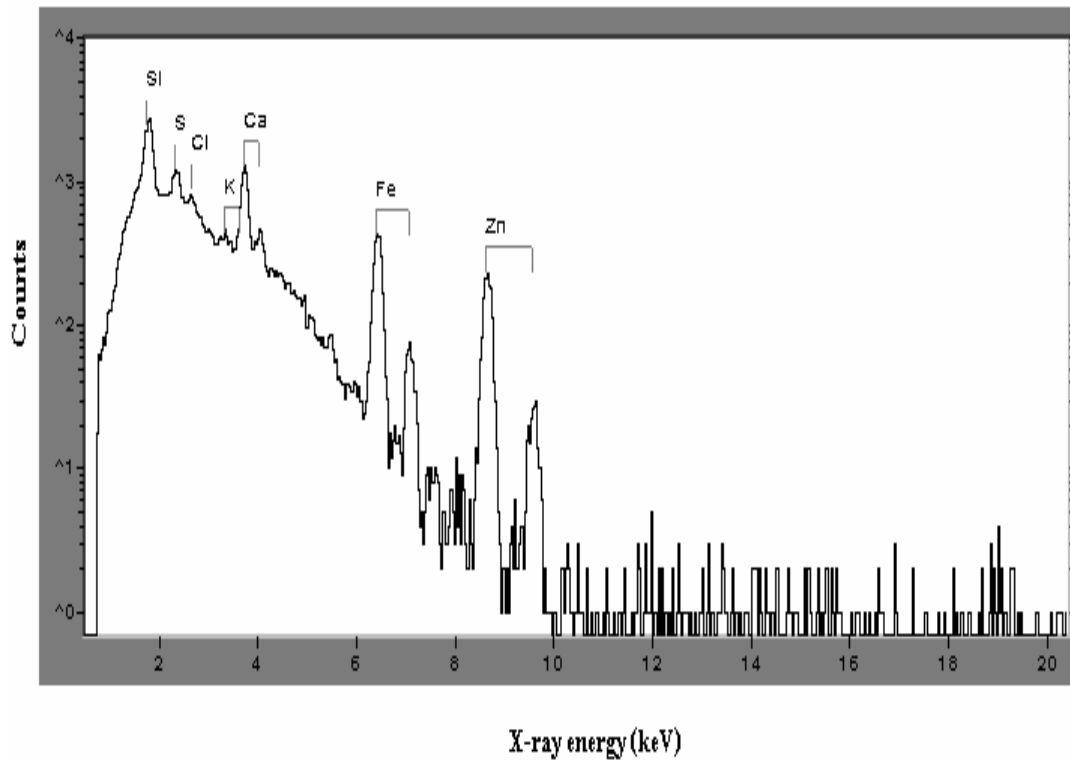


**Figure 12.** The PIXE spectrum of an Arctic aerosol sample.

## Chapter 3

### Sampling techniques for the aerosol particles studied

Size and chemical composition are important properties for the identification of aerosol particles. A variety of techniques for measuring these properties have been designed. Impactors, for example, are used for this purpose worldwide because of their being relatively cheap and being easy to operate and to manufacture. Such instruments separate aerosol particles according to their inertia by means of selective collection or impaction. Impactors can be of a single-stage or a serial, multi-stage type. Those of the latter type are usually called cascade impactors.

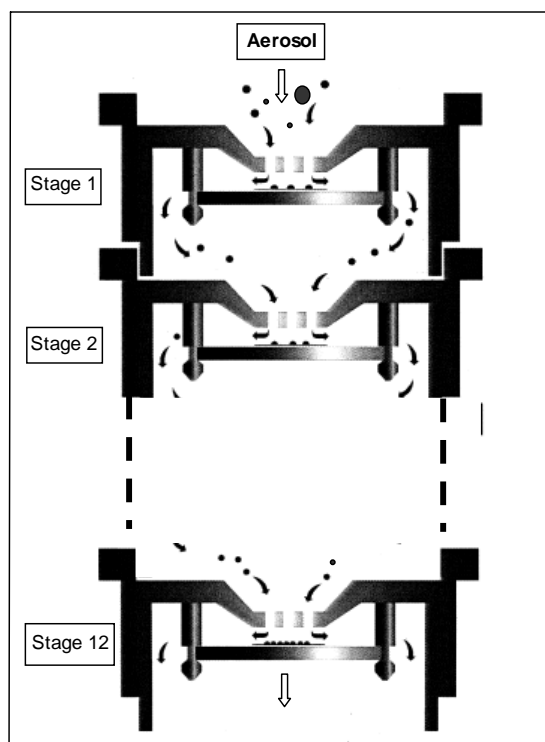


**Figure 13.** The Small Deposition area cascade Impactor, SDI, used in the measurements in connection with the AOE-01 expedition.

During the AOE-01 expedition, the aerosol samples intended for PIXE analysis were collected by use of a Dekati Low Pressure Impactor (LPI) and a Small Deposit area low-pressure Impactor (SDI). The LPI has 13 stages, enabling aerosol particles into to be separated into 12 size fractions by use of cutoff points at aerodynamic diameters of 10.00  $\mu\text{m}$  ( $\text{PM}_{10}$  inlet) to 0.03  $\mu\text{m}$ . The SDI provides 12 different size fractions too, the aerosol particles of differing size being deposited at different stages, the finest aerosol particles being collected at the last stage. A schematic view of a cascade impactor is shown in figure 13.

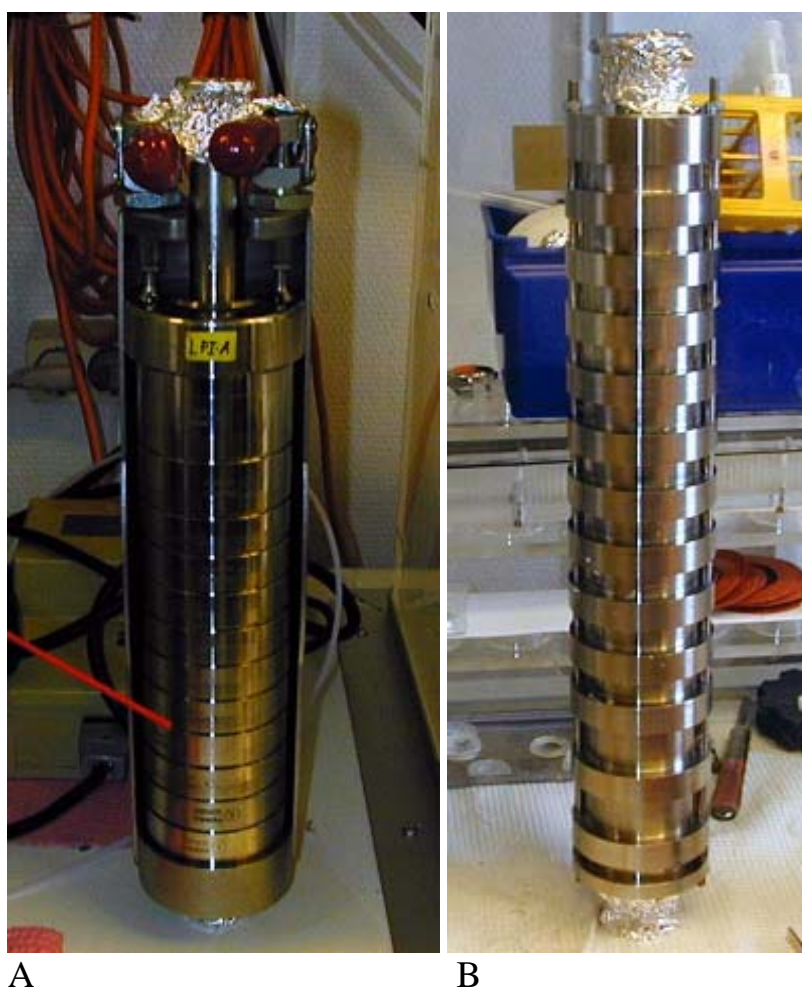


**Figure 14.** An LPI (picture A) and a SDI (picture B) cascade impactor.



**Figure 15.** Unloading an SDI cascade impactor during AOE-01. The procedure needs to be carried out inside a glove box so as to prevent contamination.

The aerosol samples for electron microscopy analysis were collected directly on transmission electron microscope grids by electrostatic precipitation as well as by impaction. Artificial "shadows" were imposed on the collected specimens prior to their being examined in the electron microscope so as improve the contrast between the small and nearly electron-transparent particles and the substrate. This was achieved in a vacuum by firing a beam of metal atoms (Pt/Pd) at the specimen at a  $30^\circ$  angle, making the metal-free shadows twice as long as the diameter of the particles. This allowed the volume of the dry particles, and thus the diameter of a sphere of equivalent volume, to be deduced. The outline of the particles remained, despite the particles being volatile upon examination during the heating of the electron beam. Also, when a partly soluble specimen was floated on water, the original outlines of the particles and its shadow were preserved, allowing the proportion of insoluble material to be estimated. The technique is described in detail in the section that follows.

## Chapter 4

### **Chemical tests conducted on the collected aerosol particles**

The preparation methods described here are for aerosol particles. Information on the various aspects of biological specimen preparation can be found elsewhere (Dykstra, 1992). The following is a brief description of how to prepare and conduct different chemical tests on the aerosol particles collected on the TEM grids.

- Collect particles on a TEM grid by impaction or electrostatic precipitation. The grids need to be carbon-coated for electrostatic precipitation. The particles should be collected only on the dull side. On the shiny side the copper grid bars stick up above the plastic and prevent a shadow from reaching the surface.
- Produce a shadow by use of silicon monoxide (SiO) when very small particles are to be examined, so as to achieve better contrast with the background than the particle itself can yield. The other aim in shadowing is to confine the chemicals a particle contains to a very small volume when the chemical tests described below are to be carried out. Even if all the contents of particles are dissolved away when a wet test is employed, the position and shape of each particle is retained, making it possible to conclude, if such is the case, that it contains none of the ion. Metals give better contrast than SiO but usually produce a spotty background and may react with the particles. Metal alloys such as Pt/Pd give optimal results. In general, the higher the boiling point of the substance which evaporated is, the finer the grain is which it produces.

## 4.1 Wet tests

Note that wet tests may fail to work unless the grid is flat. If the grid has been bent in handling, one should try to flatten it.

*Procedure:*

- Place an absorbent paper pad (Millipore "nutrient pad") in the Petri dish. Wet it thoroughly with a weak reagent (1 mg/20 ml or less). There should be only a very small surplus of free liquid.
- Place a Millipore filter on the wet pad and put the TEM grid on it with the particles facing upwards. Do not cover the dish, which should be kept in a clean, dry environment. (If one covers the dish, liquid may flood the specimens, and at the very least all the hygroscopic particles will merge). Leave the sample in the Petri dish for about an hour (exact time not critical).
- Take a new nutrient pad, place it in a Petri dish and wet it with distilled water. Put a new Millipore filter on it and transfer the TEM grid to it, again with the particles facing upwards. This step is to remove the reagent, which otherwise would crystallize over the entire surface. Leave the sample in the dish for an hour or longer (exact time not critical).
- Put the TEM grid on a dry Millipore filter until the sample has dried and then examine it in the microscope.
- Electron-opaque material appears black on the EM's fluorescent screen or on photographic prints, and shadows appear white. To make the particles resemble an optical picture with a black shadow the densities need to be inverted.

## 4.2 Sulfate test:

A ring of electron-opaque material around the particle (barium sulfate) shows the presence of sulfate. It is possible to make a semi-quantitative determination of the proportion of sulfate on the basis of the ratio of the size of the sulfate area to the particle size (revealed by its shadow) after calibration of it with test aerosol, using the same procedure. Since sulfate is the most common constituent of aerosols, this test is a very useful one.

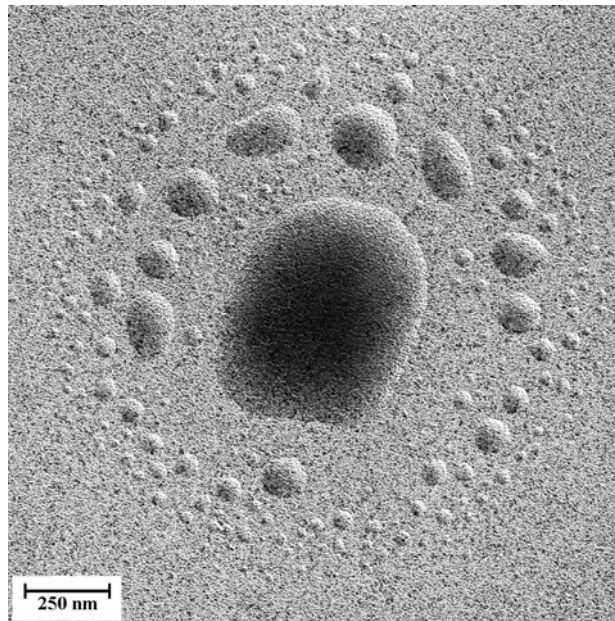


**Figure 16.** A particle containing sulphuric acid, collected by impaction.

Hydrophobic organic compounds contained in the particles can stop the reaction from proceeding. If the organics are spread out by a solvent vapour, the reaction will then proceed. The best solvent vapour that has been found for this purpose is cyclohexane ( $C_6H_{12}$ ). Ether is also good but is unpleasant to use and evaporates unless it is kept cold. Place the TEM grid on a small piece of nutrient pad laid in a Petri dish. Wet another small piece of nutrient pad with the solvent and put it in another part of the Petri dish. Put the lid on for 5 to 10 min and then proceed.

### **4.3 Vapour tests:**

Place the TEM grid on a small piece of nutrient pad in a Petri dish, place a little bit of the solvent on another piece of the pad material and put the lid on for several minutes. Vapour which dissolves constituents of the particles will form liquids that flow out through the shadow hole and crystallize or leave stains that can be seen when viewed by TEM.



#### **4.4 Biological material:**

Bacteria, viruses, spores and decaying vegetable matter all react strongly with osmium tetroxide ( $\text{OsO}_4$ ) vapour, yielding extremely electron-opaque osmium. Osmium is highly toxic and should at all times only be used under a fume hood (Dykstra, 1992).

#### **4.5 Simple hydrocarbons:**

Decane dissolves most lipids (long-chained alcohols, acids and esters), all of which have been identified in bulk samples of particles, and is also safe to use. It does not dissolve inorganic material. No deterioration of the plastic substrate is observed, even at long exposure. The dissolved material spreads out through the shadow hole, sometimes explosively.

#### **4.6 Aromatic compounds:**

Marine and continental aerosols contain a proportion of aromatic compounds. Xylene is better to use for detection purposes than benzene or toluene are since it is less toxic and does not attack the plastic substrate as vigorously. Optimal results are obtained if exposure of it to the TEM grid does not exceed five minutes. After treatment, the components that dissolve will crystallize and the crystal shape may help in identification.

#### **4.7 Heat sensitivity:**

In principle, the electron beam current can be used together with the magnification to determine the heat sensitivity of the particles by a comparison with ammonium sulfate. Ammonium sulfate can be evaporated with use of a reasonable beam current and moderately high magnification. Extending of the heating much further is not recommended, however (high magnification increases the energy density of the beam).

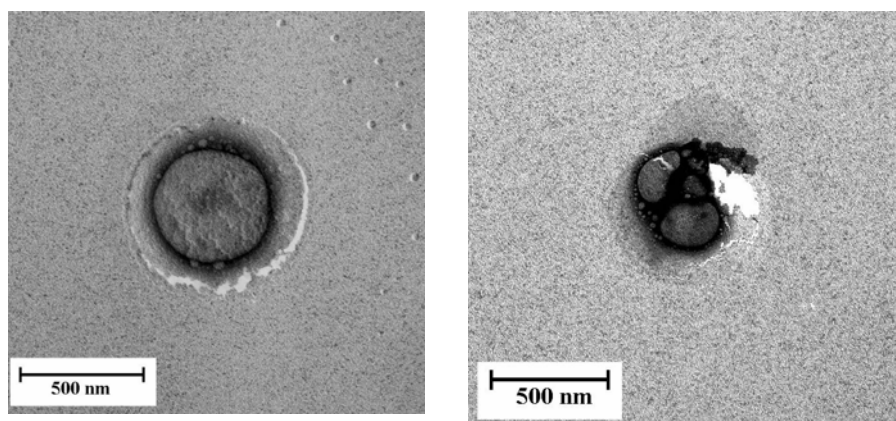


**Figure 17.** Two examples of the xylene-soluble components having dissolved to form an electron-dense dark ring (black).

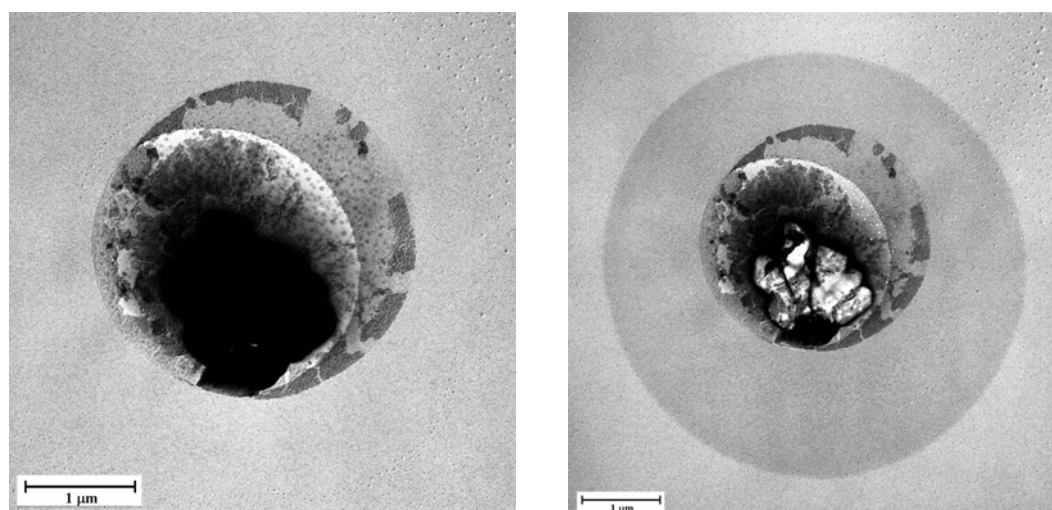


**Figure 18.** A particle like that shown in Figure 16 after its exposure to decane vapour (left), and after heating of it by the electron beam (right).

#### **4.8 Limitations of the wet chemical tests:**

The minimum amount of sulfate, for example, that can be detected is determined by the diffusion of sulfate ions out of the particle through the plastic membrane before reacting with the barium ions and the spreading of the reaction products out through the shadow hole. It is only possible to detect such tiny masses of sulfate because of the reaction being confined to a very small volume. For reaction products that are more soluble than barium sulfate, such as silver chloride, the minimum amount is larger.

## Chapter 5

### Supporting films for TEM analysis

Electron microscope specimens need not only to be thin but also to be mechanically and thermally stable and to not accumulate electrostatic charges. The grids required are available commercially, their sometimes being called "naked grids". These grids are cleaned by use of a glow-discharge method before being covered with a backing. A support film is stretched over an area of the supporting TEM-grid having a diameter of approximately 3 mm. A good support film should have the following properties:

- Being as transparent to electron beam as possible, and thus being thin, and consisting of a substance with a low scattering power.
- Remaining stable, i.e. resisting breakage and deformation during investigation by the electron microscope.

The most commonly used supporting films are plastic, carbon and combination films.

#### 5.1 Making Formvar-supported grids

The plastic films used to support grids are usually made of Nitrocellulose or Formvar (polyvinyl formaldehyde). To make Formvar-supporting grids, use is made of a 0.25-0.5% Formvar solution in either chloroform or ethylene dichloride. A glass slide is washed carefully with soap and is rubbed with a paper pad (Millipore). It is then dipped into the solution for a moment. Removal of it has to involve a steady movement in order for an even layer of the Formvar film on the slide glass to be obtained. The excess liquid is allowed to drip off and the slide is then dried in air (Dykstra, 1992).

To remove the Formvar film from the slide, the film needs to be cut by a razor blade near to the edges of the slide. The slide is then immersed obliquely in distilled water, allowing the Formvar film to float to the surface. Finally the grids are placed on the film and are fished up afterwards by means of a piece of a Parafilm (Gharibi, 2004).

## **5.2 Making Carbon-supported grids**

To make a Carbon-supported grid, a stainless-steel grid having the form of a strainer (containing holes) is placed approximately one to two centimeters below the water surface and cleaned grids are inserted on top of it. In a separate step, carbon is heated in a vacuum chamber together with a sheet of mica with a freshly broken surface. The carbon evaporates and becomes attached to the mica surface. The mica sheet is then immersed into the water vessel obliquely, leading to the carbon film being detached from the mica sheet (in the same manner as with the Formvar film), the mica falling to the bottom of the water vessel. The water level in the vessel is then lowered slowly until the floating carbon film reaches the grids. These grids with carbon backing are allowed to dry finally in particle-free air. Most laboratories have an apparatus for picking up carbon films (Gharibi, 2004).

## **5.3 Making Combination-supported grids**

Preparing combination films combines the advantages of both Formvar and carbon films. Combination films are produced by the vapour deposition of a layer of carbon on a plastic film.

## Chapter 6

### 6. Results and Conclusions

In the following, a summary of the results reported in the papers included in the thesis is provided. Three methods for analysing the aerosol particles that were sampled in the different environments were employed: SEM, TEM and PIXE.

Paper I concerns the elemental size distributions of aerosol particles in atmospheric samples from an Arctic Ocean expedition undertaken in 2001 (AOE.01), in response to the increasing interest that has been shown recently in aerosol particles in the Arctic. Measurements of the distribution of aerosol mass concentrations made during the expedition were used to study the physical and chemical properties, as well as the possible sources, of aerosol particles in the Pack Ice (PI) region of the Arctic Ocean. The total, fine and coarse mass concentrations of aerosol particles within this region were measured. The equivalent aerodynamic diameter ( $EAD < 10\mu\text{m}$ ) was used for determining the total mass concentration. The coarse fraction diameters were defined as  $2\mu\text{m} < EAD < 10\mu\text{m}$  and the fine fraction diameters as  $< 2\mu\text{m}$ . The aerosol particles were collected using stacked filter units (SFU) and two types of cascade impactors: a Low Pressure Impactor (LPI) and a Small Deposit Area Impactor (SDI). The results obtained with use of the PIXE technique for parallel samples differing in the devices employed to collect them were compared. The total mass concentrations of Cl and S were presented as a function of the transport time from the ice edge (Mtr). Trace elements of Si, Fe, Zn and Ti that were found appeared to be of biogenic origin (e.g. processed crustal material). Most of the particles belonging to the coarse mode were found to be comprised mainly of sea salt and substances of biogenic origin (e.g. bacteria). Most of the samples contained considerable amounts of Si in the fine mode, this appearing to be a potential source of the dissolved silicic acid present in the sea water. Log-normal fitting of the size distributions was applied to the

PIXE results for the aerosol samples obtained in the Pack Ice region. Modal parameters calculated for a variety of trace elements are reported.

Paper II concerns the fraction of primary aerosol particles (PAP) and secondary aerosol particles (SAP) over the Arctic in the Pack Ice region. The aerosols collected there were found to be comprised of the following: sea salt, ammonium sulphate, ammonium bisulphate, sulphuric acid mixtures, mixtures of sulphuric acid and methanesulfonic acid (MSA), compact aggregates, bacteria, microorganisms, solids, and unknowns. A total of 320 individual aerosol particles were examined by means of TEM and SEM analysis, the frequency of each of the aerosol types present being determined. The particles were also classified as being either primary (PAP) or secondary (SAP) aerosols, the fraction of each being plotted as a function of the transport time from ice edge (Mtr). It was concluded that minerals can act as nuclei for the deposition of sulphate or other condensable vapours to produce aerosol particles that can act as cloud condensation nuclei, CCN, and that SAP are more hygroscopic than PAP but contain inclusions. These inclusions showed the same basic characteristics as the PAP aerosol particles but were more hydrophobic, making it more difficult for them to grow and become CCN particles. This was seen as directly affecting the cloud properties of the atmosphere and as indirectly affecting the climate of the globe.

Paper III concerns traffic-generated emissions of ultra-fine particles from the road surface-tire interface. In a road simulator study, the road-tire interface was found to be a significant source of fine sub-micrometer particles. These particles were identified as originating to a large extent from the tires and as consisting of fragments of the carbon-reinforcing filler material (soot agglomerates) and of mineral oils from the softening filler. Identification of them was based on off-line-transmission electron-microscopy studies of ultra-fine wear particles that were collected, and on-line thermal treatment by use of a thermodesorber. The particles had a mean diameter of 15-50 nm, similar to what was found in the LDV tailpipe exhaust. A simple box-model approach was used to estimate the emission factors in the 15-700 nm size interval. The emission factors increased with increasing vehicle speed, and at speeds of 50 and 70 km·h<sup>-1</sup> they varied between  $3.7 \cdot 10^{11}$  and  $3.2 \cdot 10^{12}$  particles·vehicle<sup>-1</sup>·km<sup>-1</sup>, corresponding to 0.1-1

% of those observed for tailpipe emissions in real-world emission studies conducted at similar speeds. The emission factors originating from the road-tire interface were similar in magnitude to the particle-number emission factors derived in many studies in which the formation of new particles has been quenched in the dilution system. They were also similar to the low tailpipe particle emission levels that have been achieved by use of new engine technologies.

*Paper IV deals with particle emissions from district heating units operating on three commonly used biofuels.* The study aimed at characterising particle emissions from district heating units operating on three commonly used biofuels: forest residues, pellets and sawdust. Boilers of the moving-grate type employed in three district heating units were found to have a maximum thermal output of 1-1.5 MW. Since these output measurements were obtained using multicyclones, which were the only particle removal devices installed, it was direct emissions to ambient air that were characterised, their number and mass-size distributions being determined. The elemental composition of the particles was obtained by Particle Induced X-ray Emission analysis (PIXE) and thermal-optical analysis. The morphology of the particles was assessed by use of transmission electron microscopy (TEM). The total number concentration of particles with an aerodynamic diameter of less than 5  $\mu\text{m}$  (PM<sub>5</sub>) that were emitted at a medium-level operating load ranged from 6.3 to 7.7  $\times 10^7$  particles $\cdot\text{cm}^{-3}$ , the values for the combustion of forest residues being slightly higher. The PM<sub>5</sub> mass concentrations at a medium operating load obtained from low-pressure impactor measurements ranged from 51 to 120  $\text{mg}\cdot\text{m}^{-3}$ , the highest values being obtained for the unit operating on forest residues. Fine-mode contributions, involving particles with an aerodynamic diameter of less than 1  $\mu\text{m}$  (PM<sub>1</sub>) were dominant in both the PM<sub>5</sub>-mass and the total-number concentrations. The elements determined by PIXE ( $Z > 12$ ) were found to represent 21–34 % of the PM<sub>1</sub> mass, whereby K, S, Cl and Ca represented 18–33% of the latter and Zn, Mn, Fe, Cr, Pb and Cd 1–3 % of it. The concentrations of heavy metals emitted depended on the type of fuel and the operating load. Forest residues showed relatively high emissions of Zn, Cr, Cd and Pb, whereas pellets showed high emissions of Zn and Cd. The lowest emissions of heavy metals were from the combustion of sawdust. The particulate organic (OC) and the elemental (EC) carbon



contributions to PM1 ranged from 1 to 19% and from 0 to 56%, respectively. The particulate OC concentrations were strongly dependent upon the operating load, regardless of the type of fuel, whereas the EC concentrations were found to depend upon both the load and the type of fuel employed.

Paper V concerns a laboratory and a field test of a method for the high-temperature characterization of fly ash and fly ash precursors. The objective of the study was to design and experimentally examine a method for sampling high-temperature aerosols obtained from biomass combustion in which nucleation and condensation from vapours forming fly ash was controlled. The sampling method included a high-temperature probe in which the hot gas was diluted and then cooled. Laboratory results for sampling a model aerosol with known concentrations of SiO<sub>2</sub> particles and KCl vapour showed that with use of a high dilution ratio the KCl vapour was effectively separated from the aerosol by deposition onto the walls of the probe. When a lower dilution ratio was employed, the KCl vapour generated a distinct nucleation mode when it was cooled in the probe. The sampling method was also used for sampling flue gas from a circulating fluidized-bed boiler fired with forest residues. The results suggested that at 780°C the major fractions of Ca, K, S, and Zn were present as particles whereas most of the Cl and the Pb were present as gases. The field results here were consistent with previously reported findings indicating that the method can be used for the efficient and precise characterization of high-temperature combustion aerosols containing inorganic vapours.

## Papers

### *Paper I:*

#### **Aerosol particle elemental size distributions during the Arctic Ocean expedition in the summer of 2001**

*Arash Gharibi\**, *Erik Swietlicki*

#### **Manuscript in preparation.**

The author was responsible for the planning and preparation of the measurements and the carrying out of the sample collection conducted on board.

The author was also responsible for the PIXE analysis and was in charge of evaluating all of the PIXE results, employing the GUPIX fitting program to determine the elemental concentrations in the samples, as well as calculating the size distributions and applying the log-normal distribution function to each of elements in the samples. In the single-particle analyses, the author was responsible for producing the grids with backing for TEM and SEM and EDX, respectively, that were needed. The author wrote the article as well.

---

\* Corresponding author: arash.gharibi@nuclear.lu.se

***Paper II:***

**Summer high Arctic aerosol particles classified using  
Transmission Electron Microscopy**

***Arash Gharibi\* , Keith Bigg, Erik Swietlicki, Caroline Leck***

***Manuscript in preparation.***

The author was responsible for the planning and preparation of the measurements for the single particle analysis (TEM and SEM) and for carrying out measurements on board (ODEN) during the AOE-01 expedition. The planning and preparation work were the same as in paper I. The author carried out the single-particle imaging of TEM and SEM, conducted the chemical tests on the aerosols that were collected and chose appropriate TEM images for the different chemical tests. Finally, the author wrote the paper.

***Paper III:***

**Traffic-generated emissions of ultra fine particles from  
the road surface – tire interface.**

***A. Dahl, A. Gharibi, E. Swietlicki, A. Gudmundsson, M.  
Bohgard, M. Gustafsson and G. Blomqvist.***

**Article in press (Atmospheric Environment).**

The author was responsible for the planning and preparation of the measurements for the single-particle analyses (TEM, SEM and EDX) and for performing measurements that were conducted at the VTI facilities in Linköping, Sweden. The author and A. Dahl collaborated in writing the article.

---

\* Corresponding author: arash.gharibi@nuclear.lu.se

***Paper IV:***

**Particle emissions from district heating units operation on three commonly used biofuels.**

***A. Wierzbicka, L. Lillieblad, J. Pagels, M. Strand, A. Gudmundsson, M. Bohgard, A. Gharibi, E. Swietlicki and M. Sanati.***

***Atmospheric Environment, 2005, Volume/Issue 39/1 pp.139-150.***

The author was responsible for the planning and preparation of the measurements for the single-particle analyses (TEM, SEM and EDX) and for carrying out the measurements made in the Växjö district heating plant (Sweden). The author was responsible as well for performing the PIXE analysis and contributed to evaluation of the data. The author was likewise responsible for writing the parts of the article concerned single-particle and PIXE analysis.

***Paper V:***

**Laboratory and field test of a method for high-temperature characterization of fly ash and fly ash precursors.**

***M. Strand, M. Bohgard, E. Swietlicki, A. Gharibi, and M. Sanati.***

***Aerosol Science and Technology, 38:765, 2004.***

The author was responsible for the planning and preparation of the PIXE analysis and for the GUPIX evaluation of the data.

## Acknowledgements

Come on, be honest and admit that the first page you look at is this page and that it perhaps will be the only one. Hoping very much, however, that this is not the case, I would like to express my deepest gratitude to my supervisor, Professor Erik Swietlicki, for giving me the opportunity of participating in the AOE-01 experiment. His excellent guidance, high degree of patience and many useful suggestions have been indispensable in my study of aerosol particles. I have learned very much from him regarding the mysteries of aerosol particles. It was no easy task to get a neutrino-physicist to change his mind and become an aerosol scientist. I am not saying that I am now an aerosol scientist, but Erik opened my eyes to this field of science and I am very grateful to him for this.

I am particularly grateful as well to Dr. Keith Bigg for the fruitful discussions we have had, and for his invaluable help and advice regarding the chemical testing parts of the thesis. It is he who taught me how to handle small EM-grid creatures.

I am very thankful too for the encouragement that Professor Claes Fahlander and Bo Jacobson provided me for continuing when I had almost lost hope of finishing the work.

I would like to thank Professor Peter Ekström, the head of the Nuclear Physics Division, for allowing me to keep my office there until I had completed this work.

Thanks also for the invaluable support I have received from the staff of the Aerosol group. Especially, I want to thank Professor Bengt Martinsson for the support he provided me over the years.

I am very grateful to my co-supervisors Professor Per Kristiansson and Jan Pallon for their help during the times I needed them most.

I wish to express my thanks to Dr. Eric Carlemalm, Dr. Rolf Odselius and Lina Gefors at the Electron Microscopy Unit at Lund University for all of our pleasant discussions and social events (including coffee at 10:00) over the years. Eric Carlemalm has taught me a great deal regarding use not only of the TEM microscope but also of other apparatus routinely employed in this area. Dr. Rolf Odselius' knowledge of SEM and EDX (ISIS) has been extremely useful to my understanding of how to interpret and use SEM images and EDX spectra.

Thanks are due to A. Szpila and A. Dahl who collaborated with me on various projects.

My appreciation also goes to Adam and Hung for being so generous with their time and always being supportive.

I thank Björn and Ulf from the High-energy Physics Department for always being helpful in connection with my software and hardware problems.

I thank the various graduate students whom I have shared offices with for fostering a pleasant and productive work environment. I thank Vaida, Cintia, and Natalia.

I am sincerely thankful to all my friends, especially Monika, Eva, Johan and Peter for their help in keeping my Swedish at a good level over the years.

Regarding the details and the clarity of expression of my thesis in English I am grateful to Robert Goldsmith for his linguistic editing help.

Finally I want to express my gratitude to my family. They provided me moral support at the times I needed it most. My family in Sweden are Sara and my daughter Setare, and in Iran my father and mother and my brothers, Hatef, Ali, Parviz, and Behrooz and my sisters, Parvin, Mojgan (Homan and Hengameh) and Leila.

Again, I thank you all.

## References

O. Boucher and J. Haywood (2001) "On summing the components of radiative forcing of climate change", *Climate Dynamics*, 18, 297-302.

M. Camatini et al., *Materials characterizations* 46 (2001) 271-28.

D. Chescoe, and P.J. Goodhew, "The Operation of Transmission and Scanning Electron Microscopes", ISBN 0-19-856420-1 (1990).

J. Comiso, *Geo. Phys. letters* Vol. 29, No. 20, 1956, 2002.

M. J. Dykstra, "Biological Electron Microscopy", ISBN 0-306-44277-9 (1992).

M. Elfman, "Development of a Data Acquisition System at a Nuclear Microprobe with Applications in the Geo- and Biosciences", Ph-D thesis (2001).

B.J. Finlayson-Pitts, and J.N. Pitts, *Atmospheric chemistry: fundamentals and experimental techniques* Wiley (1986).

A. Gharibi, "Studies of aerosol particle formation from various sources using ion and electron beam analytical techniques", Licentiate Thesis (2004).

J. F. Griffith and J. A. Barnard, *Flame and Combustion*, 3<sup>rd</sup> edition, Chapman & Hall, Glasgow (1995).

W. C. Hinds, "Aerosol Technology Properties", ISBN 0-471-19410-7 (1998).

<http://www.ipcc.ch/> Intergovernmental Panel on Climate Change (IPCC) (2001).

T.B. Johansson, R. Akselsson and S.A.E Johansson, Nucl. Instr. and Meth. 84 (1970) 141.

S. A. E. Johansson and J. L. Campbell, "PIXE A Novel Technique for Elemental Analysis", Wiley Chichester UK (1988).

D.J. Kohls G. Beaucage, Current Opinion in Solid State and Materials Science 6 (2002) 183-194.

C. A. Pope and D. W. Dockery, "Air Pollution and Health", Epidemiology of Particle Effects, First edition, pp. 673-705 (1999).

J. Pallon, "Special PhD project in the course: Accelerators based Measurements Techniques", April (2005).

J. H. Seinfeld and S. N. Pandis, "Atmospheric Chemistry and Physics, From Air Pollution to Climate Change", John Wiley and Sons, (1998).

A. Shariff "Development of New Experimental Facilities at the Lund Nuclear Microprobe Laboratory", Ph-D thesis (2004).

M. Strand, "Particle Formation and Emission in Moving Grate Boilers Operating on Woody Biofuels", Ph-D thesis (2004).

S. R. Taylor, Scott M. McLennan, "The Continental Crust: its Composition and Evolution, Blackwell Scientific Publications", (1985)

WHO 2003, Health Aspects of Air Pollution with Particulate Matter, Ozone and Nitrogen Dioxide, Report from WHO Working Group Meeting, Bonn 13-15 Jan. 2003.



I

# Aerosol particle elemental size distributions during the Arctic Ocean expedition in the summer of 2001

Arash Gharibi<sup>\*</sup>, Erik Swietlicki

Division of Nuclear Physics, Physics, Department, Lund University, P.O. Box 118, SE-221 00 Lund, Sweden

## Abstract

The central Arctic Ocean is a region that is particularly sensitive to changes in climate due to various feedback mechanisms that exist there. During the Arctic summer, aerosol particles influence the radiative balance primarily by acting as cloud condensation nuclei, knowledge of the sources and properties of these particles being essential for an adequate assessment of future climate changes in the Arctic region. As part of an atmospheric research programme, aerosol samples were collected on filters (SFU: Stacked Filter Unit) and cascade impactors (an LPI: a Dekati Low-Pressure Impactor; and an SDI: a Small Deposit Impactor) during an expedition to the Arctic Ocean in the summer of 2001 on the Swedish icebreaker *Oden*. The aerosol samples were analyzed by PIXE (Particle Induced X-ray Emission) to obtain information concerning their size-resolved elemental composition.

The elements Si, S, Cl, K, Ca, Ti, Fe, Zn and Br were usually found in concentrations above their detection limits, also within the pack ice between 88°-89° N. The sources of these elements at these high latitudes could be attributed to sea spray production (Cl, K, Ca, S, Br), secondary DMS-derived sulphur compounds (S), and a source of primary aerosol particles that contributed to the concentrations of the elements Si, K, Ca, Ti, Fe and Zn. This latter source has a composition which resembles that of average crustal rock. A likely transport route of minerals to the high Arctic is by way of ice-rafting by means of the Transpolar Current. These minerals originate from Siberian river runoff into the Laptev and Kara Seas. On the basis of the data available, the possibility cannot be ruled out that the minerals were first processed by the Arctic Ocean biota before becoming airborne.

It appears that bubble bursting that ejects solid particles from the sea surface microlayer or the sea water below into the atmosphere, a process

---

<sup>\*</sup> Corresponding author: arash.gharibi@nuclear.lu.se

that only take place in the open leads between ice floes, is a major source of primary aerosol particles, which are composed of sea salt and of crustal or biogenic matter. The ice-rafting of crustal material by way of the Transpolar Current and the bubble bursting that occurs in open leads are both potentially sensitive to changes in climate.

## **1. Introduction**

The climate is changing more rapidly in the Arctic than in any other region on earth (ACIA, 2004). Yet the models predicting what the climate in this region will be in the future are the highly uncertain. This is due to our inadequate understanding of several strong feedback mechanisms specific to the Arctic region.

Aerosol-cloud-climate interactions and feedbacks during the summer months in the high Arctic are particularly important because of the major impact they have on the regional radiative balance there. Key factors in obtaining a better understanding of the climate system in the Arctic are the sources of primary and secondary aerosols and their ability to form cloud droplets. Like the warmer oceans, the Arctic Ocean has a persistent low-altitude cloud cover, especially in the summers. Yet in contrast to the warm marine stratocumulus clouds that typically cool the surface of the oceans the Arctic summer clouds are a warming factor most of the year for the climate there (Intrieri et al. 2002, Tjernström 2005). The reasons behind this net warming effect are that the Arctic summer clouds are optically thin and overlying a high-albedo surface (the pack ice), and that the surface temperature is severely restricted to fall between the melting points of fresh water ice (0 °C) and that of salty sea water (-1.5 °C). Also, due to the relatively low aerosol concentrations in the central Arctic region with the resulting low concentrations of cloud condensation nuclei (CCN), the clouds tend to have relatively low number concentrations of larger sized droplets and thus a low reflectivity.

The fact that the Arctic clouds warm the surface below them does not mean that the cloud cover there necessarily enhances either the warming of the Arctic or the melting of the pack ice that the human impact on the global climate system (a positive feedback mechanism) brings about. Instead, the radiative forcing induced by humans may still be negative, for instance if melting of the pack ice also results in an increased number of CCN, thus increasing the cloud reflectivity. Such a scenario would constitute a negative feedback mechanism, one that may delay and mitigate – or even prevent – the accelerated pack ice melting observed

during the Arctic summer (Comiso, 2002; <http://arctic.atmos.uiuc.edu/cryosphere/>; ACIA 2004).

The Arctic boundary layer (ABL) is typically shallow (~200 m), well mixed and capped by a thin cloud deck (Tjernström, 2005). The lifetime of aerosol particles in the ABL is severely limited by the fact that ABL air is humid (near the saturation point, with frequent fogs) and is always mixed with the lowest cloud deck. Particles are removed by frequent precipitation in the form of drizzle, which often is frozen. Observations made during earlier icebreaker expeditions (*Oden* 1991, 1996 and 2001) have clearly shown there to be additional sources of aerosol particles and CCN at air-transport times from the ice edge in excess of 48 hours. In the summers, the likely sources of aerosol particles (and thus also of CCN) to the ABL are sea salt, DMS-derived secondary sulphates, primary biogenic particles, ice-rafted crustal material, and the homogeneous nucleation of gas-phase precursors. The downward mixing of aerosol particles transported long-range from the air above the ABL is also a plausible source.

The balance of the climate system in the Arctic is thus very intricate, current climate models in fact being unable to agree even on the current cloud cover and structure, let alone their being able to adequately incorporate knowledge of the biological and chemical feedbacks involved that may arise as a result of atmosphere-ice-ocean interaction when changes in climate take place. The mixing from the surface to the free troposphere above the clouds is far weaker than it is at lower latitudes and the mixed layer is much thinner, adding to the difficulties that climate models have in specifying the processes that take place in the Arctic.

As part of an Atmospheric Research Programme (Leck et al., 2004), aerosol samples were collected on filters (SFU: Stacked Filter Unit) and cascade impactors (LPI: Dekati Low-Pressure Impactor; SDI: Small Deposit Impactor) during the expedition to the Arctic Ocean in the summer of 2001 (AOE-2001) on the Swedish icebreaker *Oden*. The aerosol samples were analyzed with PIXE (Particle Induced X-ray Emission) to obtain information regarding the size-resolved elemental composition.

The main objective of the measurements presented here is to use the elemental composition and size distributions of the aerosol particles collected over the Arctic Ocean pack ice to deduce information regarding the sources of the Arctic summer aerosols and the processes that contribute to level determining their.

## 2 Experimental

The AOE01 aerosol study program concerned conditions during the summer in the following regions of the Arctic Ocean or locations there: the marginal ice zone (MIZ), open water (OW), pack ice station 3 (PI<sub>3</sub>), Ice Drift and pack ice station 4 (PI<sub>4</sub>). Tables 1a and 1b present the effective aerosol sampling time, the overlap in sampling time between the different collectors, the wind speed, and the transport time over the ice since the last contact with open water (Mtr). During the Ice Drift, the ship was moored to an ice floe. The ice drift started on August 1 near latitude 89.0° N, longitude 1.8° E and ended on August 22 at 88.2° N, 9.4° W.

Sample Station	Sample no.				Mtr Median (h)				Eff. sam. time (min)				Sampling period			
	LPIA	SDIA	SDIB	SFUA	LPIA	SDIA	SDIB	SFUA	LPIA	SDIA	SDIB	SFUA	(Julian day)	(Julian day)	(Julian day)	(Julian day)
MIZ	1				0				676				186,53	187		
"	2				0				455				187,56	187,9		
"	3		1		>120				>120	747		766	190,25	190,8		190,25 190,78
"	4		2		>120				>120	724		1477	192,38	192,9		192,38 193,4
"	5		"		>120				>120	675		"	192,93	193,4		" "
OW	6		3		62,8				13,8	1440		725	196,58	197,6		196,58 197,09
PI 3	"		4		"				72	"		673	"	"		197,12 197,58
DRIFT	7		5		72				72	1436		1436	207,96	209		207,96 208,96
"	8	2	6		84		84		84	1994		1994	1378	214,42	215,8	214,42 215,42
"	"	"	7		"		"		96,2	"		"	588	"	"	215,44 215,85
"	9	3	8		44		44		113	2860		2755	1420	216,72	218,7	216,8 218,7 216,72 217,71
"	"	"	9		"		"		44	"		"	1366	"	"	" 217,76 218,71
"	10	4	10		72		48		48	2788		2715	1359	218,82	220,8	218,84 220,7 218,82 219,76
"	"	"	11		"		"		84	"		"	1367	"	"	" 219,8 220,75
"	11	5	12		55,5		55,5		49,7	2456		2456	1013	221,54	223,6	221,54 223,6 221,54 222,58
"	"	"	13		"		"		70,5	"		"	1365	"	"	" 222,64 223,59
"	12	6	14		>120		>120		>120	3610		3610	2264	224,48	227,5	224,48 227,5 224,48 226,5
"	"	"	15		"		"		>120	"		"	1265	"	"	" 226,56 227,5
"	13	7	7		16	47,6	47,6	47,6	>120	2780	2703	2703	1338	227,58	229,5	227,63 229,5 227,63 229,5 227,58 228,51
"	"	"	17		"		"		47,6	"	"	"	1370	"	"	" 228,56 229,51
"	14	8	8		18	36	36	36	28,6	4512	2262	2262	1030	229,57	233,4	229,63 231,5 229,63 231,5 229,57 230,29
"	"	"	19		"		"		40	"		"	1325	"	"	" 230,59 231,51
"	"	9	9		20	45,3	45,3	94,8	"	2091	2091	1124	"	"	231,63	233,4 231,63 233,4 231,57 232,5
"	"	"	21		"		"	34,5	"	"	"	1018	"	"	"	" 232,69 233,43
PI 4	"	"	22		"		"	25,8	"	"	"	1200	"	"	"	236,76 237,59

Table 1.a

% time average of SFUA by			Wind Speed (m/s)											
*=LPIA	*=SDIA	*=SDIB	LPIA			SDIA			SDIB			SFUA		
%=SFU / *	%=SFU / *	%=SFU / *	min	median	max	min	median	max	min	median	max	min	median	max
			3	7,2	10,9									
			3,1	4,9	6,1									
(3-1) <b>98</b>			1,8	4,6	7,3							1,8	4,6	7,3
(4-2) <b>49</b>			2,6	5,1	6,9							2,6	5,9	9,1
(5-2) <b>46</b>			4,4	7,8	9,1							"	"	"
(6-3) <b>50</b>			8,7	11,3	13,5							8,7	11	13,3
(6-4) <b>47</b>			"	"	"							9,5	11,6	13,5
(7-5) <b>100</b>			3,1	6,3	9,6							3,1	6,3	9,6
(8-6) <b>69</b>		(2-6) <b>69</b>	0,7	9,9	15,2				0,7	9,9	15,2	7,6	12,8	15,2
(8-7) <b>29</b>		(2-7) <b>29</b>	"	"	"				"	"	"	0,7	3,1	7,9
(9-8) <b>51</b>		(3-8) <b>52</b>	2,7	7,1	10,5				2,7	7,1	10,5	5,1	8,1	10,5
(9-9) <b>48</b>		(3-9) <b>50</b>	"	"	"				"	"	"	2,7	5,8	9
(10-10) <b>49</b>		(4-10) <b>50</b>	1,2	7,3	13				1,7	7,5	13	5	8,7	13
(10-11) <b>49</b>		(4-11) <b>50</b>	"	"	"				"	"	"	1,2	4,4	10,8
(11-12) <b>41</b>		(5-12) <b>41</b>	0,3	5,2	9,6				0,3	5,2	9,6	0,3	4	8,5
(11-13) <b>56</b>		(5-13) <b>55</b>	"	"	"				"	"	"	2,3	6,5	9,6
(12-14) <b>63</b>		(6-14) <b>63</b>	1,1	3,3	9,1				1,1	3,3	9,1	1,1	3,4	9,1
(12-15) <b>35</b>		(6-15) <b>35</b>	"	"	"				"	"	"	1,4	3,1	5,6
(13-16) <b>48</b>	(7-16) <b>50</b>	(7-16) <b>50</b>	4,7	6,6	11,9	5	6,7	11,9	5	6,7	11,9	4,7	8,05	11,9
(13-17) <b>49</b>	(7-17) <b>51</b>	(7-17) <b>51</b>	"	"	"	"	"	"	"	"	"	4,1	5,9	10,1
(14-18) <b>23</b>	(8-18) <b>45</b>	(8-18) <b>45</b>	0,2	5	10,2	0,2	5,2	9,4	0,2	5,2	9,4	0,4	4,8	6,1
(14-19) <b>30</b>	(8-19) <b>58</b>	(8-19) <b>58</b>	"	"	"	"	"	"	"	"	"	1,7	6,4	9,4
(14-20) <b>25</b>	(9-20) <b>54</b>	(9-20) <b>54</b>	"	"	"	0,9	4,8	10,2	0,9	4,8	10,2	0,9	3,3	5,8
(14-21) <b>23</b>	(9-21) <b>49</b>	(9-21) <b>49</b>	"	"	"	"	"	"	"	"	"	5,4	7,5	10,2
												0,5	3	6,3

Table 1.b. The number inside brackets is a sum of % time average of two or more impactor. For example (8-6) **69** and (8-7) **29** in the first column means the running time of SFUA6 and SFUA7 together cover **98** % of the running time of the LPIA8.

## 2.1 Aerosol sampling system

Four cascade low-pressure impactors were used during the expedition to collect highly size-resolved aerosol particle samples. These were LPIA and LPIB (Dekati Low Pressure Impactors A and B), SDIA and SDIB (Small Deposit Impactors A and B). The LPI impactor consists of 13 impaction stages of equivalent aerodynamic diameter with experimental  $d_{50}$ -values of 0.03-10.33  $\mu\text{m}$ , and EAD (Hillamo, 1994). SDI is another type of multi-jet low pressure cascade impactor (Maenhaut et al., 1996a), one which can classify aerosol particles into 12 size fractions ( $d_{50}$ -values 0.045-8.39  $\mu\text{m}$  EAD). As the name implies, the SDI impactor samples the aerosol particles on a small area of the collection substrate (8 mm in diameter as compared with 10 mm for the LPI). It was developed with the specific intention of facilitating subsequent PIXE analysis.

The elemental concentration data presented here were all obtained from the analysis of aerosol samples collected from a sampling manifold equipped with a PM10 inlet (cut-off 10  $\mu\text{m}$  EAD). The SFU (Stacked Filter Unit) sampler collected particles on two sequential 47-mm diameter Nuclepore polycarbonate filters: a coarse-mode filter (pore size 8  $\mu\text{m}$ ) and

a fine-mode filter (pore size 0.4  $\mu\text{m}$ ). The coarse filter had a 50% collection efficiency at  $\sim 2$   $\mu\text{m}$  EAD and collected particles in the size range of 2 to 10  $\mu\text{m}$  EAD, whereas the fine filter collected particles of less than 2  $\mu\text{m}$  EAD. The SFU operated at a flow rate of 16.7  $\text{L min}^{-1}$ . Twenty-two samples were collected with this device. The SDI and LPI were operated at a flow rate of 10  $\text{L min}^{-1}$ . The collection foils in the SDI consisted of a very thin AP1 polyimide film, whereas LPIA7 to LPIA14 (used for collection during the ice drift period) consisted of a 1.5  $\mu\text{m}$  thick KIMFOL polycarbonate film. A 10  $\mu\text{m}$  thick Nuclepore polycarbonate film was used as a backing substrate for LPIA1 to LPIA6 (MIZ and OW stations). The blank concentrations increased in the order AP1 < KIMFOL < Nuclepore. The collection time per SDI sample was 20-60 hours, its being 10-75 hours for the LPI. A total of 9 and 14 samples, respectively, were collected using the SDI and the LPI.

Sampler	Inlet	Stages	Flow (l/min)	Backing
LPIA(1-6)	10 $\mu\text{m}$	13	10	Nuclepore
LPIA(7-14)	"	"	"	Kimfol
SDI	"	12	"	AP1
SFUA	"	2	16.7	Nuclepore

Table 2. Summary of properties of the aerosol samplers used.

## 2.2 The PIXE analyses

A proton beam of 2.55 MeV was used in the PIXE (Particle Induced X-ray Emission) analysis of the aerosol samples that were collected. The analyses were performed at the so-called Macro beam-line of the ion beam accelerator facility at the Division of Nuclear Physics in Lund. The collimated beam size was 0.63  $\text{mm}^2$ , 0.92  $\text{mm}^2$  and 0.92  $\text{mm}^2$  for the SDI, LPI and SFU samples, respectively. The PIXE spectra were acquired by an HPGe X-ray detector having a 340  $\mu\text{m}$  thick Mylar absorber and a 1 mm hole. The spectra were collected until a preset proton beam charge of 25-50  $\mu\text{C}$  was reached. The larger preset charge was used for the lightly loaded samples. Finally, the resulting X-ray spectra were evaluated by the GUPIX fitting program, which converts peak areas to elemental concentrations. Blank correction was performed by subtraction of the average blank concentration from the elemental concentrations obtained from GUPIX. The minimum detection limit (MDL) was set to 2.32 times the standard deviation of the blank. This corresponds to a 99% confidence level (Papasiropoulos, 2002). Elemental concentrations that fell below the MDL of a sample were removed from the data set. Details of the Macro

beam-line setup and the PIXE spectrum analysis and quantification procedures can be found in (Shariff, 2004).

### 3 Results

The aerosol filter and impactor sampling schedule was devised so that there would be a maximum overlap in time between the various samplers. Despite these efforts, there are some cases in which there were short periods of time that were not completely overlapping (Table 1b). Figure 1 shows an example of the chlorine (Cl) concentrations obtained using different samplers, and for time periods that were overlapping to the extent this could be achieved in practice. It is obvious that there is considerable scatter in the elemental concentrations as measured using the different samplers. The differences were normally within a factor of two, but were in some cases as large as a factor of ten. Similar discrepancies were noted for the other elements. Sudden changes in ABL aerosol and trace gas concentrations can frequently be observed (Leck and Bigg, 1999). The observed scatter may partly be due to the incomplete correspondence of sampling times. However, most of the scatter seems to be attributable to the type of aerosol sampler used. Maenhaut et al. (1996b) present elemental concentrations determined by PIXE analysis of parallel aerosol samples collected using different impactor and filter samplers during the Arctic Ocean expedition in the summer of 1991. They report discrepancies of the same order of magnitude as those observed in 2001 and attribute these to sampling artifacts rather than to analytical (PIXE) errors. Plausible sampling artifacts include bounce-off, losses to the walls inside the sampler, and evaporation of semi-volatile compounds such as hydrochloric acid (HCl) from acidified sea salt aerosols.

During three of the ice drift impactor sampling periods, samples from both of the SDI impactors were analyzed by PIXE (SDIA 7-9 and SDIB 7-9, with complete overlap in time). These can be used to further elucidate the cause of the inter-sampler concentrations discrepancies. The deviations between the two SDI impactors are quite small with respect both to the total elemental concentrations (as can be seen in Figure 1 for Cl) and the elemental size distributions. The latter is shown in Figure 2 for the mass size distributions of the sulphur obtained from the two SDI impactors (SDIA 7 and SDIB 7) operating completely in parallel for the entire sampling period. This agreement is particularly gratifying in view of these impactor samples (SDI 7-9) having been collected at the very end of the ice drift period – well into the pack ice region at around 88° N – when



the lowest elemental concentrations during the entire expedition were encountered. AP1 backing substrates were used for all the SDI impactors.

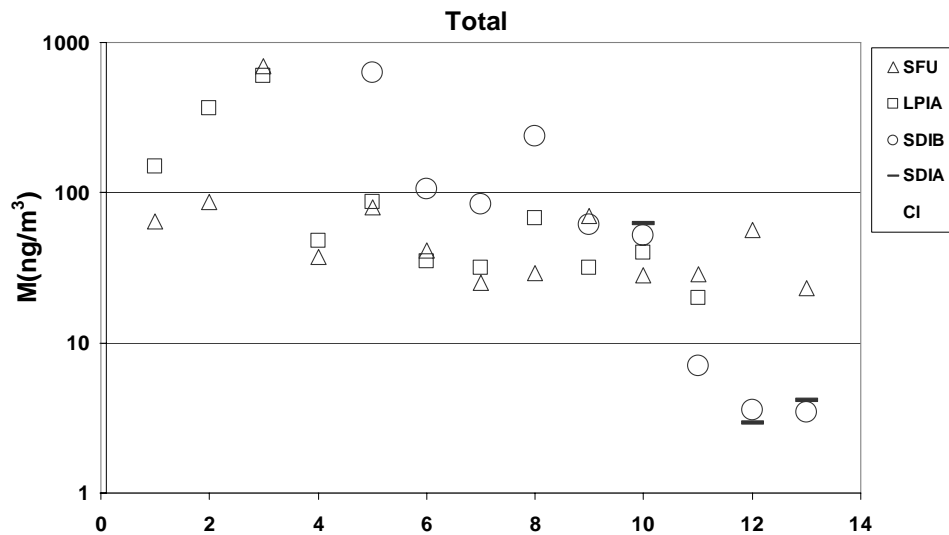


Figure 1. Measured Cl concentrations for overlapping samples obtained using various aerosol collection devices.

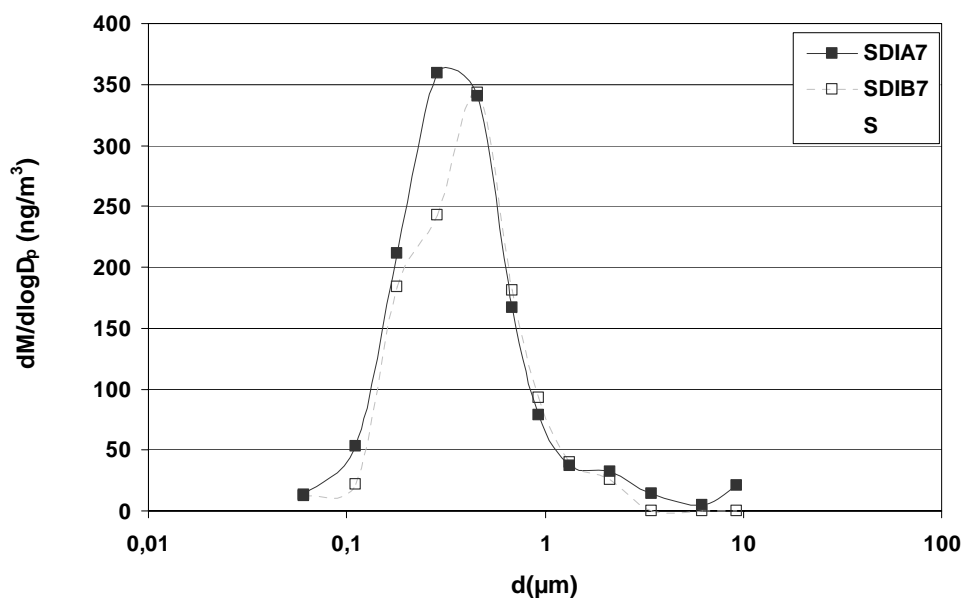


Figure 2. Elemental size distribution for sulphur obtained with two parallel SDI impactors. The aerosol was collected during the ice drift well into the pack ice region around 88° N.

### 3.1 Log-normal modal fitting of elemental size distribution data

Log-normal modal fitting of the measured elemental size distributions was performed in order to be able to present the elemental size distribution data in succinct form and to facilitate comparison with other data of similar character (Maenhaut et al., 1996b; Hillamo et al., 2001). The fitting results – obtained by minimising  $\chi^2$  – are presented in Table 3 for the elements Si, S, Cl, K, Ca, Ti, Fe, Zn, and Br, and for impactor samples SDIB 2-9 and SDIA 7-9 collected during the ice drift. For each mode, the table contains estimates of the elemental mass concentration ( $m$  in  $\text{ng}\cdot\text{m}^{-3}$ ), the geometric mean diameter ( $D_g$  in  $\mu\text{m}$ ) and the geometric standard deviation ( $\sigma_g$ ) of each mode and element (logarithmic base = 10). The table also presents the sum of all the modal mass concentrations ( $M_{\text{tot}}$  in  $\text{ng}\cdot\text{m}^{-3}$ ) and the sum of the mass concentrations over all impactor stages from the original data ( $M_{\text{sum}}$  in  $\text{ng}\cdot\text{m}^{-3}$ ). This fitting was only carried out for the SDI impactor samples, since the LPI samples showed less consistent modal structures, making fitting problematical. A condensed graphical representation of the fits for impactor sample SDIB02 is shown in Figure 3 for the elements Si, S, Cl, K, Ca, and Fe. Two modes are evident, centred around geometric mean diameters  $D_g$  of 0.1-0.3  $\mu\text{m}$  and 0.5-2  $\mu\text{m}$ , respectively.

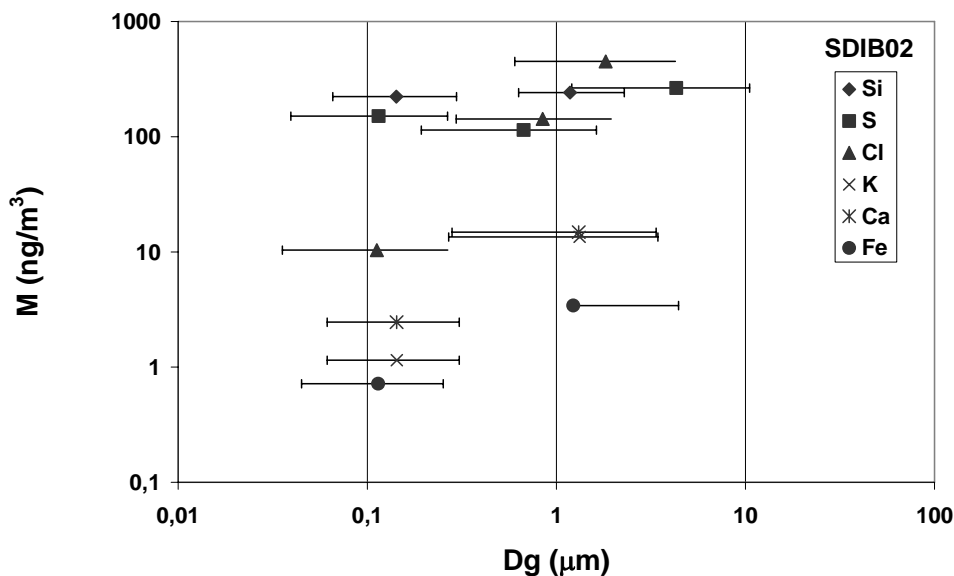


Figure 3. The best-fitting, log-normal distribution on SDIB02 data for elements Si, S, Cl, K, Ca, and Fe. Two modes  $D_g$  corresponding to 0.1-0.3  $\mu\text{m}$  and 0.5-2  $\mu\text{m}$  particles is evident.

SDIB02	Si	S	Cl	K	Ca	Ti	Fe	Zn	Br
m( $\text{ng}/\text{m}^3$ )	223.09	151.06	10.39	1.15	2.45	0.65	0.72		0.03
$D_g$ ( $\mu\text{m}$ )	0.14	0.11	0.11	0.14	0.14	0.11	0.11		0.13
$\sigma_g$ ( $\mu\text{m}$ )	1.12	1.31	1.37	1.14	1.14	1.32	1.21		1.20
m( $\text{ng}/\text{m}^3$ )	241.02	114.21	142.78	13.48	14.84	1.69	3.43	4.71	0.00
$D_g$ ( $\mu\text{m}$ )	1.18	0.67	0.85	1.33	1.31	0.86	1.23	0.81	0.47
$\sigma_g$ ( $\mu\text{m}$ )	1.71	1.43	1.30	1.59	1.57	1.17	2.60	1.10	1.02
m( $\text{ng}/\text{m}^3$ )		264.40	450.16			0.43	0.00	0.56	0.12
$D_g$ ( $\mu\text{m}$ )		4.31	1.82			3.46	0.00	3.19	1.42
$\sigma_g$ ( $\mu\text{m}$ )		1.44	1.34			5.00	0.00	1.75	1.75
$M_{\text{tot}}$ ( $\text{ng}/\text{m}^3$ )	464.12	529.67	603.33	14.62	17.30	2.77	4.15	5.27	0.15
$M_{\text{sum}}$ ( $\text{ng}/\text{m}^3$ )	416.41	540.04	625.12	17.95	21.75	2.80	4.83	4.02	0.15
SDIB03	Si	S	Cl	K	Ca	Ti	Fe	Zn	Br
m( $\text{ng}/\text{m}^3$ )	118.63	1200.00	19.18	4.34	4.00	0.25	0.68	0.10	0.01
$D_g$ ( $\mu\text{m}$ )	0.27	0.29	0.25	2.02	0.46	0.32	0.15	0.15	0.14
$\sigma_g$ ( $\mu\text{m}$ )	2.34	1.27	1.14	2.57	1.35	1.14	2.64	1.75	1.24
m( $\text{ng}/\text{m}^3$ )	28.50	300.00	98.50		2.00	0.79	0.47	0.11	0.07
$D_g$ ( $\mu\text{m}$ )	0.95	1.40	1.90		2.12	0.63	0.77	0.70	1.33
$\sigma_g$ ( $\mu\text{m}$ )	1.31	1.29	1.81		1.80	1.10	1.41	1.20	1.33
m( $\text{ng}/\text{m}^3$ )	86.45	160.00				0.29	2.02	0.41	0.06
$D_g$ ( $\mu\text{m}$ )	2.57	3.46				1.52	5.11	1.58	4.49
$\sigma_g$ ( $\mu\text{m}$ )	2.25	2.60				1.15	1.62	5.00	1.14
$M_{\text{tot}}$ ( $\text{ng}/\text{m}^3$ )	233.57	1660.00	117.67	4.34	6.00	1.33	3.17	0.62	0.14
$M_{\text{sum}}$ ( $\text{ng}/\text{m}^3$ )	233.11	1321.19	130.38	5.40	5.58	1.34	3.04	0.53	0.11
SDIB04	Si	S	Cl	K	Ca	Ti	Fe	Zn	Br
m( $\text{ng}/\text{m}^3$ )	88.66	40.55	6.91	2.47	1.60	1.52	0.40	0.16	0.00
$D_g$ ( $\mu\text{m}$ )	0.14	0.10	0.18	0.14	0.13	0.13	0.17	0.14	0.18
$\sigma_g$ ( $\mu\text{m}$ )	1.13	1.53	1.70	1.70	1.52	1.32	1.42	1.71	1.01
m( $\text{ng}/\text{m}^3$ )	65.09	39.03	60.28	2.13	3.50	0.30	1.00	0.25	0.01
$D_g$ ( $\mu\text{m}$ )	0.76	1.07	1.58	1.58	1.54	1.54	1.38	1.18	2.79
$\sigma_g$ ( $\mu\text{m}$ )	1.55	2.46	1.50	1.50	1.83	1.83	2.11	1.73	1.23
m( $\text{ng}/\text{m}^3$ )	77.05								
$D_g$ ( $\mu\text{m}$ )	3.24								
$\sigma_g$ ( $\mu\text{m}$ )	2.18								
$M_{\text{tot}}$ ( $\text{ng}/\text{m}^3$ )	230.81	79.58	67.19	4.60	5.10	1.82	1.40	0.41	0.01
$M_{\text{sum}}$ ( $\text{ng}/\text{m}^3$ )	187.12	80.05	74.13	4.03	4.52	2.04	1.41	0.51	0.02
SDIB05	Si	S	Cl	K	Ca	Ti	Fe	Zn	Br
m( $\text{ng}/\text{m}^3$ )		657.36	7.47	12.07	1.43	3.82	0.34	0.27	0.04
$D_g$ ( $\mu\text{m}$ )		0.28	0.14	1.28	0.10	0.37	0.16	0.15	0.31
$\sigma_g$ ( $\mu\text{m}$ )		1.92	2.22	2.20	1.64	1.52	1.23	2.92	1.56
m( $\text{ng}/\text{m}^3$ )	29.86	27.54	236.05		10.60		1.71	0.40	
$D_g$ ( $\mu\text{m}$ )	0.80	1.91	1.64		1.22		1.22	1.35	
$\sigma_g$ ( $\mu\text{m}$ )	1.44	1.85	1.65		2.41		5.00	1.52	
m( $\text{ng}/\text{m}^3$ )	47.71								
$D_g$ ( $\mu\text{m}$ )	3.68								
$\sigma_g$ ( $\mu\text{m}$ )	1.77								
$M_{\text{tot}}$ ( $\text{ng}/\text{m}^3$ )	77.56	684.91	243.52	12.07	12.03	3.82	2.05	0.67	0.04
$M_{\text{sum}}$ ( $\text{ng}/\text{m}^3$ )	293.94	726.40	237.69	14.87	11.96	3.95	1.63	0.73	0.04

Table 3.

<b>SDIB06</b>	<b>Si</b>	<b>S</b>	<b>Cl</b>	<b>K</b>	<b>Ca</b>	<b>Ti</b>	<b>Fe</b>	<b>Zn</b>	<b>Br</b>
m( $\text{ng}/\text{m}^3$ )	24.82	117.45				1.64			UDL
$D_g$ ( $\mu\text{m}$ )	0.11	0.30				0.25			
$\sigma_g$ ( $\mu\text{m}$ )	1.55	1.81				1.76			
m( $\text{ng}/\text{m}^3$ )	157.53	41.89	51.55	1.59	4.80	0.25	0.95		
$D_g$ ( $\mu\text{m}$ )	0.90	2.15	2.08	2.70	2.23	1.17	1.08		
$\sigma_g$ ( $\mu\text{m}$ )	5.00	1.80	1.72	1.48	1.58	1.11	5.00		
$M_{\text{tot}}$ ( $\text{ng}/\text{m}^3$ )	182.35	159.34	51.55	1.59	4.80	1.89	0.95	0.00	UDL
$M_{\text{sum}}$ ( $\text{ng}/\text{m}^3$ )	167.47	181.12	60.85	4.26	7.88	1.98	1.17	0.39	
<b>SDIB07</b>	<b>Si</b>	<b>S</b>	<b>Cl</b>	<b>K</b>	<b>Ca</b>	<b>Ti</b>	<b>Fe</b>	<b>Zn</b>	<b>Br</b>
m( $\text{ng}/\text{m}^3$ )		191.05		4.21	2.09	UDL			0.34
$D_g$ ( $\mu\text{m}$ )		0.40		1.27	2.15				1.31
$\sigma_g$ ( $\mu\text{m}$ )		1.86		2.22	1.76				1.92
m( $\text{ng}/\text{m}^3$ )		11.83	50.81						
$D_g$ ( $\mu\text{m}$ )		1.86	1.86						
$\sigma_g$ ( $\mu\text{m}$ )		1.49	1.60						
$M_{\text{tot}}$ ( $\text{ng}/\text{m}^3$ )	0.00	202.88	50.81	4.21	2.09	UDL	0.00	0.00	0.34
$M_{\text{sum}}$ ( $\text{ng}/\text{m}^3$ )	72.14	217.41	52.37	3.98	2.08	0.23	23.21	9.31	0.32
<b>SDIB08</b>	<b>Si</b>	<b>S</b>	<b>Cl</b>	<b>K</b>	<b>Ca</b>	<b>Ti</b>	<b>Fe</b>	<b>Zn</b>	<b>Br</b>
m( $\text{ng}/\text{m}^3$ )		9.62			0.42	UDL		0.42	0.02
$D_g$ ( $\mu\text{m}$ )		0.40			2.15			0.17	0.93
$\sigma_g$ ( $\mu\text{m}$ )		1.52			2.76			1.23	4.92
m( $\text{ng}/\text{m}^3$ )		0.56	3.22					0.74	
$D_g$ ( $\mu\text{m}$ )		1.01	1.86					2.52	
$\sigma_g$ ( $\mu\text{m}$ )		1.88	1.63					5.00	
$M_{\text{tot}}$ ( $\text{ng}/\text{m}^3$ )	0.00	10.17	3.22	0.00	0.42	UDL	0.00	1.15	0.02
$M_{\text{sum}}$ ( $\text{ng}/\text{m}^3$ )	5.76	10.87	3.69	0.29	0.39		1.69	0.93	0.01
<b>SDIB09</b>	<b>Si</b>	<b>S</b>	<b>Cl</b>	<b>K</b>	<b>Ca</b>	<b>Ti</b>	<b>Fe</b>	<b>Zn</b>	<b>Br</b>
m( $\text{ng}/\text{m}^3$ )		5.25			0.11	UDL			0.02
$D_g$ ( $\mu\text{m}$ )		0.45			0.28				1.31
$\sigma_g$ ( $\mu\text{m}$ )		1.50			1.41				1.92
m( $\text{ng}/\text{m}^3$ )		0.28	3.32		0.08				
$D_g$ ( $\mu\text{m}$ )		2.31	3.46		1.56				
$\sigma_g$ ( $\mu\text{m}$ )		1.61	1.60		2.83				
$M_{\text{tot}}$ ( $\text{ng}/\text{m}^3$ )	0.00	5.53	3.32	0.00	0.19	UDL	0.00	0.00	0.02
$M_{\text{sum}}$ ( $\text{ng}/\text{m}^3$ )	5.70	5.68	3.63	0.19	0.19	0.01	1.83	0.67	

Table 3.

<b>SDIA07</b>	<b>Si</b>	<b>S</b>	<b>Cl</b>	<b>K</b>	<b>Ca</b>	<b>Ti</b>	<b>Fe</b>	<b>Zn</b>	<b>Br</b>
<b>m(ng/m<sup>3</sup>)</b>	72.47	224.45	8.88		2.97	0.26			0.04
<b>D<sub>g</sub> (μm)</b>	0.11	0.32	0.16		0.13	0.13			0.21
<b>σ<sub>g</sub>(μm)</b>	1.49	1.79	1.49		1.32	1.32			1.72
<b>m(ng/m<sup>3</sup>)</b>	80.22	16.81	51.42		2.10	0.20			
<b>D<sub>g</sub> (μm)</b>	0.60	1.95	1.80		1.59	1.59			
<b>σ<sub>g</sub>(μm)</b>	1.87	1.89	1.66		2.36	4.86			
<b>m(ng/m<sup>3</sup>)</b>	32.94								
<b>D<sub>g</sub> (μm)</b>	3.45								
<b>σ<sub>g</sub>(μm)</b>	1.57								
<b>M<sub>tot</sub>(ng/m<sup>3</sup>)</b>	185.62	241.26	60.30	0.00	5.07	0.46	0.00	0.00	0.04
<b>M<sub>sum</sub>(ng/m<sup>3</sup>)</b>	184.95	252.68	61.25	6.66	5.25	0.39	1.84	0.83	0.04
<b>SDIA08</b>	<b>Si</b>	<b>S</b>	<b>Cl</b>	<b>K</b>	<b>Ca</b>	<b>Ti</b>	<b>Fe</b>	<b>Zn</b>	<b>Br</b>
<b>m(ng/m<sup>3</sup>)</b>	2.25	9.44	0.10	0.17	0.25	UDL			
<b>D<sub>g</sub> (μm)</b>	0.14	0.39	0.13	0.59	0.96				
<b>σ<sub>g</sub>(μm)</b>	2.74	1.47	2.00	5.00	2.34				
<b>m(ng/m<sup>3</sup>)</b>	0.58	1.15	2.97				1.26		
<b>D<sub>g</sub> (μm)</b>	0.86	1.24	1.95				4.10		
<b>σ<sub>g</sub>(μm)</b>	1.32	1.27	1.70				1.16		
<b>m(ng/m<sup>3</sup>)</b>	3.40								
<b>D<sub>g</sub> (μm)</b>	2.79								
<b>σ<sub>g</sub>(μm)</b>	4.67								
<b>M<sub>tot</sub>(ng/m<sup>3</sup>)</b>	6.23	10.60	3.07	0.17	0.25		3.14	0.65	0.02
<b>M<sub>sum</sub>(ng/m<sup>3</sup>)</b>	5.27	10.85	3.07	0.22	0.25	0.02	3.45	0.68	0.02
<b>SDIA09</b>	<b>Si</b>	<b>S</b>	<b>Cl</b>	<b>K</b>	<b>Ca</b>	<b>Ti</b>	<b>Fe</b>	<b>Zn</b>	<b>Br</b>
<b>m(ng/m<sup>3</sup>)</b>		4.94		0.44	0.41	0.08	1.98	0.76	0.04
<b>D<sub>g</sub> (μm)</b>		0.29		1.72	3.48	1.49	0.75	0.88	0.50
<b>σ<sub>g</sub>(μm)</b>		1.47		2.65	3.41	5.00	5.00	5.00	5.00
<b>m(ng/m<sup>3</sup>)</b>	1.81	1.51	4.06		0.57		3.63		
<b>D<sub>g</sub> (μm)</b>	2.99	0.48	1.84		2.81		2.74		
<b>σ<sub>g</sub>(μm)</b>	1.06	2.77	1.78		1.11		1.15		
<b>M<sub>tot</sub>(ng/m<sup>3</sup>)</b>	11.37	6.44	4.43	0.44	0.98	0.08	5.61	0.76	0.04
<b>M<sub>sum</sub>(ng/m<sup>3</sup>)</b>	9.14	6.42	4.23	0.51	1.19	0.09	4.14	1.34	0.04

Table 3. Log-normal elemental size distribution parameters for Si, S, Cl, K, Ca, Ti, Fe, Zn, and Br, and impactor samples SDIB 2-9 and SDIA 7-9. The mass concentration  $M_{tot}$  (ng/m<sup>3</sup>) and  $M_{sum}$  (ng/m<sup>3</sup>) obtained from the fitting and experiments are shown in last two rows. The  $D_g$  (geometric mean diameter, in μm) and  $\sigma_g$  (geometric standard deviation) of each mode are presented in rows two and three.

### 3.2 Primary sea salt particle sources

For all but one of the SDI samples (3.5  $\mu\text{m}$  for SDIB 9), Cl has a peak in mass size distribution in the narrow size interval (for  $D_g$ ) of 1.58-2.08  $\mu\text{m}$ . This mode most likely originates from the drying of film and jet droplets generated by bubble bursting in the sea water. For particle sizes  $>0.5 \mu\text{m}$ , the enrichment factors for sulphur (compared with the Cl in the sea water as a reference) are comparatively small, and were found in the interval of 1-20, the smallest values being around 1-2  $\mu\text{m}$ , coinciding with the peak in the coarse mode of Cl. An example is shown in Figure 4, which displays the size-dependent enrichment factors for sulphur compared with the Cl in sea water (Riley and Skirrow, 1975) for impactor samples SDIB 4-6, the local wind speed varying between 1.1 and 13  $\text{m}\cdot\text{s}^{-1}$  during the sampling period. At sizes greater than 1  $\mu\text{m}$ , coarse mode, the particles are almost composed of primary sea salt aerosol. The reference value for Cl in sea salt is taken from Riley and Skirrow (1975).

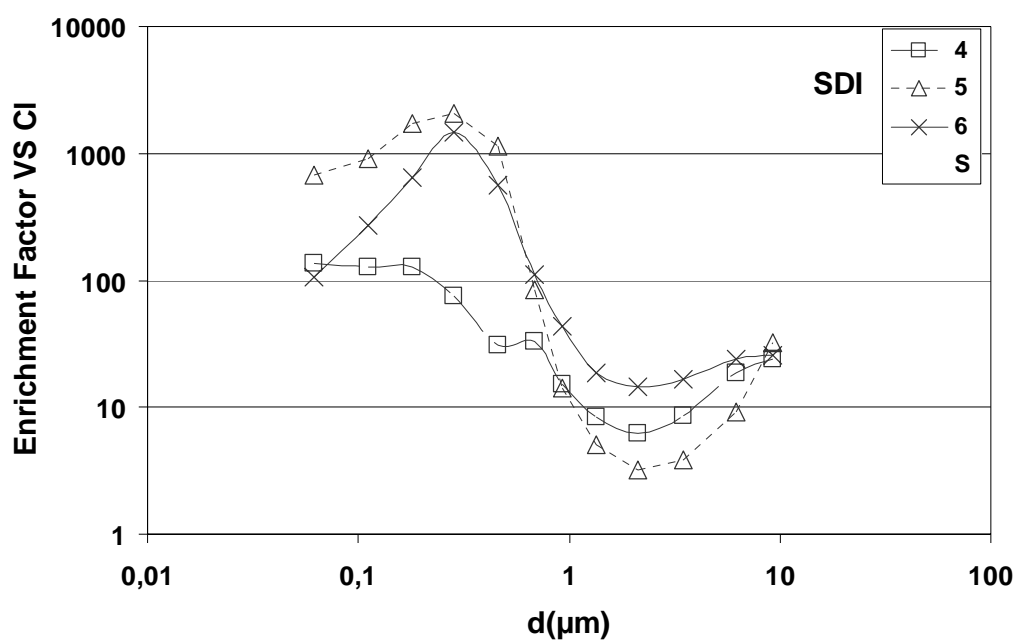


Figure 4. Size-dependent enrichment factors for S versus Cl in sea water in three SDI impactor samples collected around  $\sim 88^\circ$  in the pack ice.

Since sulphur was present in all the SDI impactor samples, the volatilization of HCl from the acidified aerosol samples cannot be ruled out. The enrichment factors for sulphur as well as for the other elements as compared to the Cl in sea water are expected to be  $>1$ , especially in the sub-micrometer particle-size ranges in which the condensation of acidic secondary sulphur compounds contributes a significant mass fraction in comparison to the mass of the primary particles on which condensation takes place. As can be seen in Figure 7, the enrichment factors for sulphur as compared with the Cl in the sea water are large indeed (typically  $>10^2$ ) in the sub-micrometer particle-size range, indicating there to be a source of secondary sulphur. The same holds too for the other SDI impactor samples. Since Na was not detected in the PIXE analysis, calculation of the concentrations of non-sea salt sulphates was not possible for this data set.

Size-dependent enrichment factors for K and Ca as compared with the Cl in the sea water were also close to unity for particle sizes  $>0.5 \mu\text{m}$ , falling between 1 and 2 for K, and 1 and 10 for Ca. For sulphur (S), the smallest K and Ca enrichment factors were found at around 1-2  $\mu\text{m}$ , located in the coarse-mode Cl peak. Since both K and Ca are major components of sea salt, this shows that particles in the super-micrometer size fraction have a composition similar to that of sea salt. This further corroborates the mass mode centred around 1-2  $\mu\text{m}$  in EAD as being caused to a large extent by bubble bursting in the sea water. Figure 5 shows that the Cl concentrations increase generally with increasing local wind speed, also over the pack ice where the open leads were often too narrow to permit extensive wave formation and whitecapping. These findings are in agreement with those made during the two earlier summer icebreaker expeditions to the Arctic Ocean in 1991 and 1996 (Maenhaut et al., 1996b; Hillamo et al., 2001).

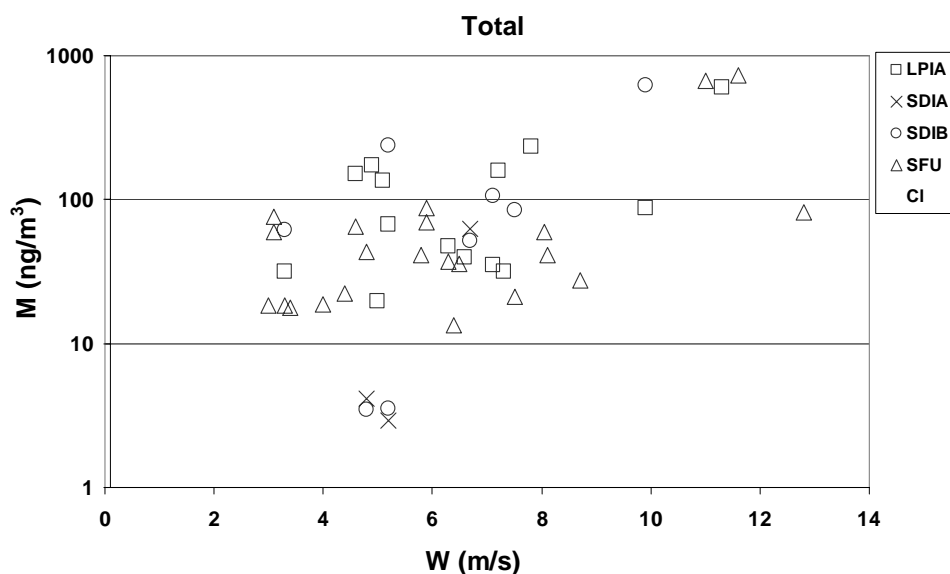


Figure 5. Measured Cl concentrations as function of median wind speed during the sampling period.

### 3.3 Secondary sulphate particle sources

Most of the sulphur in the SDI ice drift impactor samples was confined to a mode with geometric mean diameters  $D_g$  of 0.10-0.45  $\mu\text{m}$ , all but two of these  $D_g$  falling in the narrow size range of 0.28-0.45  $\mu\text{m}$ . The latter range corresponds to the so-called accumulation mode, which is a consistent feature of the summer Arctic Ocean aerosol particle number-size distribution (Heintzenberg et al, 2005). This mode is at least partly a result of the processing of Aitken mode particles (typically <80 nm in dry diameter) in clouds and fogs. Since most of the aerosol particle surface area is typically found in the Aitken and accumulation mode size ranges, a substantial mass fraction of the sulphur in this mass mode also comes from the condensation of such secondary sulphur-containing compounds as sulphuric acid and methane sulphonate (MSA) directly onto the aerosol particles in a water vapour sub-saturated condition external to clouds and fogs. These sulphur compounds are produced by the gas-phase oxidation of  $\text{SO}_2$  and other DMS-derived gaseous compounds.

Hillamo et al. (2001) refer to the mode centered around 0.3  $\mu\text{m}$  containing sulphate, MSA and ammonium ions as being the major accumulation mode, a mode for the same ions around 0.1  $\mu\text{m}$  being classified as representing an Aitken mode. These impactor samples were collected during the summer 1996 expedition to the same region.



As already noted, the enrichment factors for sulphur as compared with the Cl in the sea water were large (typically  $10^2$ - $10^3$ ) for all the SDI impactor samples in the sub-micrometer particle size range. It can be concluded that for particle diameters  $< 1 \mu\text{m}$  the source of secondary sulphur is the oxidation of DMS released by phytoplankton. The major source regions for DMS are found in the open water and in the marginal ice zone surrounding the Arctic pack ice. Again, these observations are in agreement with the findings obtained in the two earlier expeditions (Maenhaut et al., 1996b; Hillamo et al., 2001).

### 3.4 Primary crustal particle sources

In contrast to the low enrichment factors found for S, K and Ca in the super-micrometer region, the element Si was typically enriched by a factor of  $10^4$ - $10^7$ , for Ti  $10^3$ - $10^6$ , Fe  $10^3$ - $10^6$ , Ni  $10^3$ - $10^6$  and Zn  $10^3$ - $10^5$  when all the SDI impactor samples and all the particle sizes are taken into account. This clearly indicates that during the summers in the high Arctic pack ice region there are sources of these elements other than sea spray. These elements are not known to be involved in atmospheric gas-to-particle conversion processes similar to the production of sulphate from DMS. Instead, the additional source is likely to generate primary particles containing these elements.

In examining plots such as in Figure 3 for all the individual SDI impactor samples (not shown here), the elements of sub-micrometer size appear to be present in fairly constant relative concentrations, even though the absolute concentrations vary substantially. To examine this further, ratios of the various elements to Si were calculated for the fine fraction aerosol particles, using all SDI impactor samples for the stages  $< 2.69 \mu\text{m}$  (EAD). Such elemental ratios to Si were also calculated for the global average crustal composition as a reference (Taylor and McLennan, 1985) for the elements K, Ca, Ti, Fe and Zn. The results are displayed in Figure 6a.

It can be concluded that the elemental ratios to Si show a similar pattern for all the impactor samples and that in most cases these ratios lie within a factor of ten with respect to the crustal reference. This also means that most enrichment factors in comparison to Si in the crustal reference are within the range of 0.1-10.

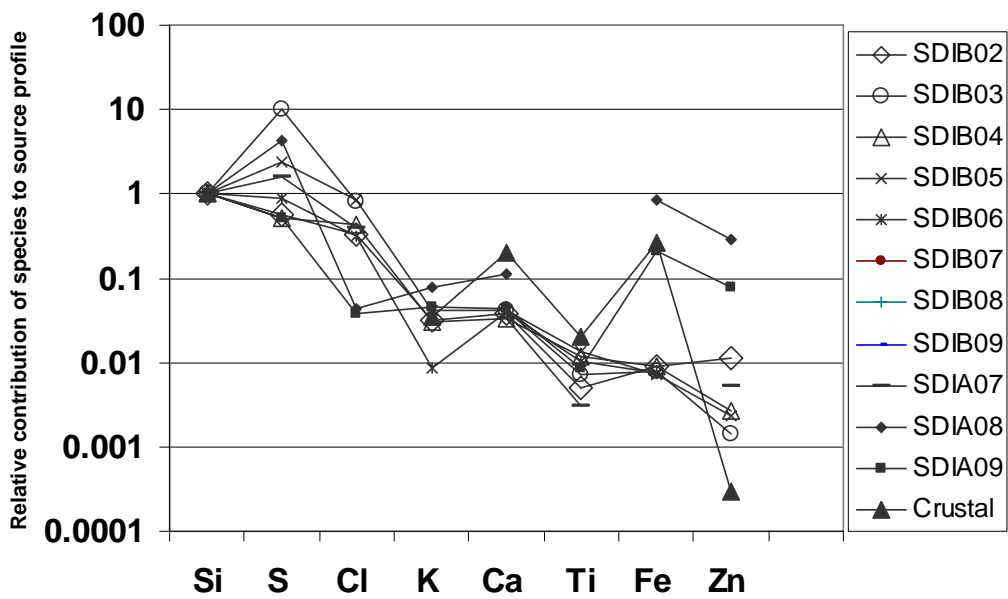


Figure 6a. Source profile for aerosol particles  $<2.69\ \mu\text{m}$  (EAD) compared to the global average crustal composition.

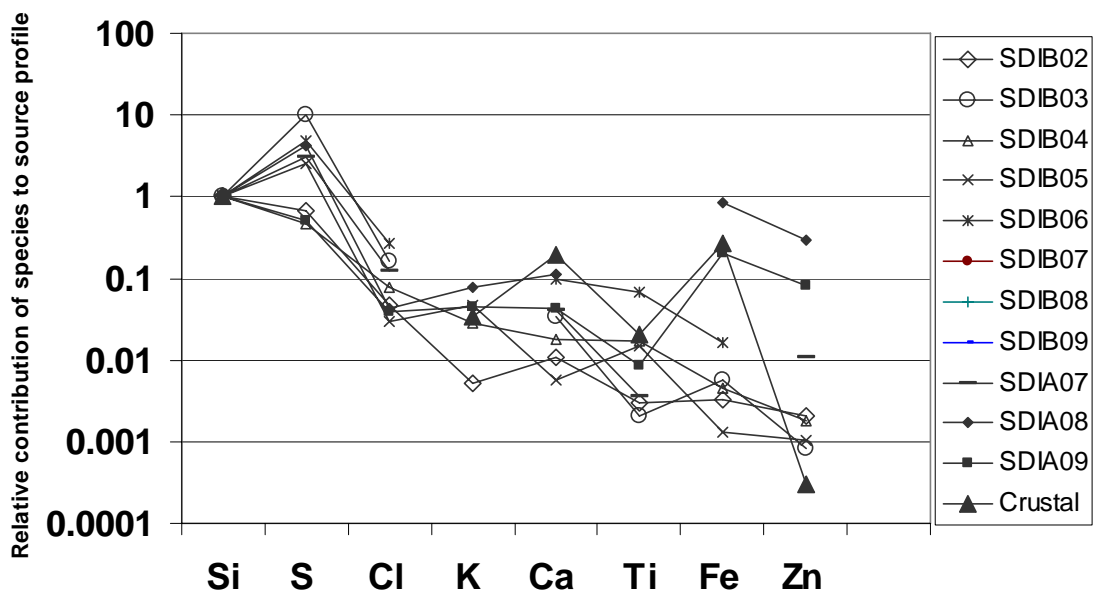


Figure 6b. Source profile for aerosol particles  $<0.577\ \mu\text{m}$  (EAD) compared to the global average crustal composition.

The characteristic crustal elements in addition to Si that were quantified were K, Ca, Ti and Fe. The general pattern for these elements was that the K/Si ratio resembled that of the reference crustal Si composition, whereas Ca, Ti and Fe were found at somewhat lower concentrations than their crustal average. Zn was found to be enriched. The same pattern (Figure 6b), but with larger scatter, was observed for the impactor stages below 0.577  $\mu\text{m}$  (EAD) alone. The similarity between the elemental ratios to Si of K, Ca, Ti, Fe and Zn and the reference crustal composition appears to imply that the fine fraction aerosol (<2.69  $\mu\text{m}$  EAD), also that below 0.577  $\mu\text{m}$  (EAD), has a crustal-like component.

It has been well documented that the Siberian rivers carry large quantities of crustal material into the Laptev and Kara Seas, from which it tends to be transported further into the high-Arctic by the Transpolar Current. Patches of crustal material discoloring the surface of multi-year ice have often been reported in the high-Arctic. These were also observed during AOE-2001. Samples of such ice-rafted sediments (IRS) were collected during AOE-2001 and were analyzed for POC (Particulate Organic Carbon) and PCBs (Gustafsson et al., 2005), and for isotopic content (Andersson, personal communication, 2005).

On the basis of the low salinity (31.4) of the surface waters (at 8 m depth), the high QSE (quinine sulphate equivalent) values, and the observed values for POC and  $\delta^{13}\text{C}$ -POC, Gustafsson et al. (2005) concluded that the water and ice system sampled at 88°-89° N during the ice drift had originated from the Lena River estuary in the Laptev Sea and been transported across the Pole by the Transpolar Current. In addition, the Nd and Sr isotopic analysis of IRS collected further to the south (81.5°-82.5° N) during the same expedition indicates this crustal material to originate from the Kara Sea (Andersson, personal communication, 2005). The freshwater river runoff from the Siberian Yenisey and Ob rivers that flow into the Kara Sea first has to move eastward into the Laptev Sea before reaching the Transpolar Current that crosses over the North Pole.

Whatever the exact geographical origin may have been, these studies show that crustal material from the western Siberian rivers was present on the surface of multi-year ice in the high-latitude pack ice region during the icebreaker expedition in the summer of 2001. It is thus not unlikely that these IRS can also be found in an airborne state as aerosol particles. This raises the question of the mechanism by which they become airborne.

Maenhaut et al. (1996b) likewise found crustal material in the aerosol collected in the high-Arctic during the icebreaker expeditions in the summer of 1991, their suggesting that these were at least to some extent the result of the local mechanical wind-blown generation of aerosols from IRS.

Another alternative generation route is via the surface water of the open leads between ice floes. During the summer ice-melting period, the solid particulate matter deposited on the surface of the ice, or within the melting ice, is released either into the surface sea water or onto the surface microlayer covering the open leads. The larger mineral particles sediment to larger depths and, if reaching the ocean floor before dissolving in the water column, add to the thick sediment layers at the bottom of the Arctic Ocean.

The sea-surface microlayer (SML) is a thin structured interface separating the atmosphere and the ocean (Wurl and Obbard, 2004, Grammatika and Zimmerman, 2001). The thickness of the SML depends on both the amount of organic matter present and the wind speed (Liu and Dickhut, 1998) but is normally <1000  $\mu\text{m}$ . It can serve both as a sink and as a source of anthropogenic compounds, including chlorinated hydrocarbons, organic compounds, polycyclic aromatic hydrocarbons (PAH) and heavy metals, due to its unique chemical composition (Wurl and Obbard, 2004). These compounds, as well as organic matter and organisms, can be highly enriched in the SML as compared with their underlying bulk sea water concentrations.

Mineral particles deposited onto the SML probably have a smaller probability of being removed from the sea surface by sedimentation, since they are engulfed in the microlayer. Bubbles bursting at the surface inevitably need to penetrate this SML in order to eject the bubble gases to the atmosphere. In doing so, they may also eject material from the SML as film droplets that subsequently form aerosol particles. The somewhat larger jet droplets bring solid material and sea water caught in the wake of the rising bubble into the air. Bubble bursting may transfer solid particles – such as crustal ice-rafted sediments – from the SML or the sea water immediately below the surface of the open leads and into the air above. This constitutes a source then of primary aerosol particles of an elemental composition resembling that of the mineral particles ejected by way of the bubble bursting process.

Another alternative is that crustal material is first dissolved in the sea water and is then taken up by the Arctic Ocean biota. Silicon, for example, is an important component of marine biogenic matter. Planktonic organisms such as diatoms, radiolarians, and silicoflagellates use silicon to build up their skeletal shell. These organisms take up Si in dissolved form

as silicic acid,  $\text{Si}(\text{OH})_4$ . The uptake of silicic acid by the biota can be very efficient and can deplete the surface layer of dissolved Si. The major input of Si and other crustal elements to the world's oceans is through chemical weathering of the sediments and minerals of continental origin that are brought into the oceans by river runoff (Treguer et al., 1995; Barrie and Hoff, 1985). Other comparatively minor pathways are Aeolian transport from the continents, and seafloor weathering. The transfer of minerals from the hydrosphere to the biosphere initiates the biological cycling of minerals. To our knowledge, there is no study available describing the elemental composition of Arctic Ocean biota, at least with regard to the trace elements involved. It is not unlikely, however, that the elemental ratios of the oceanic biota resemble those of the minerals taken up by the organisms there. It cannot be ascertained, therefore, on the basis of existing elemental data, to what extent the crustal material has first been processed by the organisms inhabiting the surface layer of the Arctic Ocean during the summers, prior to its penetrating the SML by way of bubble bursting and contributing to the Arctic aerosol.

### **3.5 Transport since the last contact with open water**

The open waters of the Arctic Ocean south of the ice edge are biologically very productive during the summers, releasing DMS into the surface water. The DMS that leaks into the marine atmospheric boundary layer is oxidized to sulphate compounds and MSA that add to the secondary sulphur mass found in the marine aerosol. In the open sea, sea salt particles are also produced by wave action followed by bubble bursting. Over the pack ice, both DMS and sea salt production are markedly reduced (Leck and Persson, 1996). Frequent fogs and low clouds over the marginal ice zone and the pack ice also rapidly reduce the concentrations of all soluble particles. The aerosol particles produced in the open sea or the marginal ice zone and advected northward towards the Pole are thus efficiently scavenged during transport. Nilsson and Leck (2002) estimate the turnover time for sulphate and MSA in the Arctic marine boundary layer to be ~18 h and the turnover time for DMS(g) to be considerably longer (~59 h).

In the absence of sources of new aerosol particles over the pack ice, the particle number and mass concentrations of aerosols can thus be expected to decrease with the increase in transport time since the last contact with open water (denoted here as  $M_{tr}$ ). This transport time was estimated for the 2001 expedition on the basis of ice maps and of back trajectories of the air mass.

Figures 7a and 7b show the way in which the mass concentrations of chlorine and sulphur – summed over all the SDI and LPI impactor stages and both the SFU filters – change with transport time since the last contact with open water. A steep decline initially is seen during the first 40 h of transport over the ice, consistent with a turnover time of ~18 h for these hygroscopic aerosols containing NaCl or sulphates and MSA. Following the minima at  $Mtr \approx 40$  h, the concentrations of both sulphur and chlorine increase again. For sulphur, there is a tendency towards a maximum concentration of around  $Mtr \approx 60$  h, followed by another decrease for a very long  $Mtr$ . The sulphur concentrations at  $Mtr \approx 60$  h are similar to those observed over the open water close to the ice edge, whereas the concentrations for chlorine at  $Mtr > 50$  h are considerably lower than over open water.

A similar analysis was performed by Heintzenberg et al. (2006) for the number concentrations in the various modes of the sub-micrometer aerosol number-size distribution. For the 2001 expedition, the particles belonging to the large accumulation mode (geometric mean diameters of 470 nm) display a behavior very similar to that shown in Figures 6a and 6b. This mode in the number-size distribution corresponds to the mass mode of around 1.5-2  $\mu m$  observed for the Cl mass-size distributions. The accumulation mode particles (geometric mean diameters at 133 nm for 2001) show a less distinct minimum of  $Mtr = 24-48$  h and more constant concentrations as a function of  $Mtr$ .

Similar trends were found by Bigg and Leck (2001) for the concentration of cloud condensation nuclei. The trace elements Si, Fe, Zn and Ti do not show any such trend in the sense that there is no decline in concentration during the first 40 hours of transport.

The observed increase in elemental mass concentrations for sulphur and chlorine to an apparent steady state concentration at a very long  $Mtr$  is a strong indication of there being sources of both secondary sulphate and chlorine well within the pack ice region of the high Arctic during the summers. Since advection from lower latitudes is ruled out, there are basically two alternatives:

1. Local production of aerosol particle mass within the Arctic Boundary Layer (ABL);
2. Down-mixing of air from above the ABL.

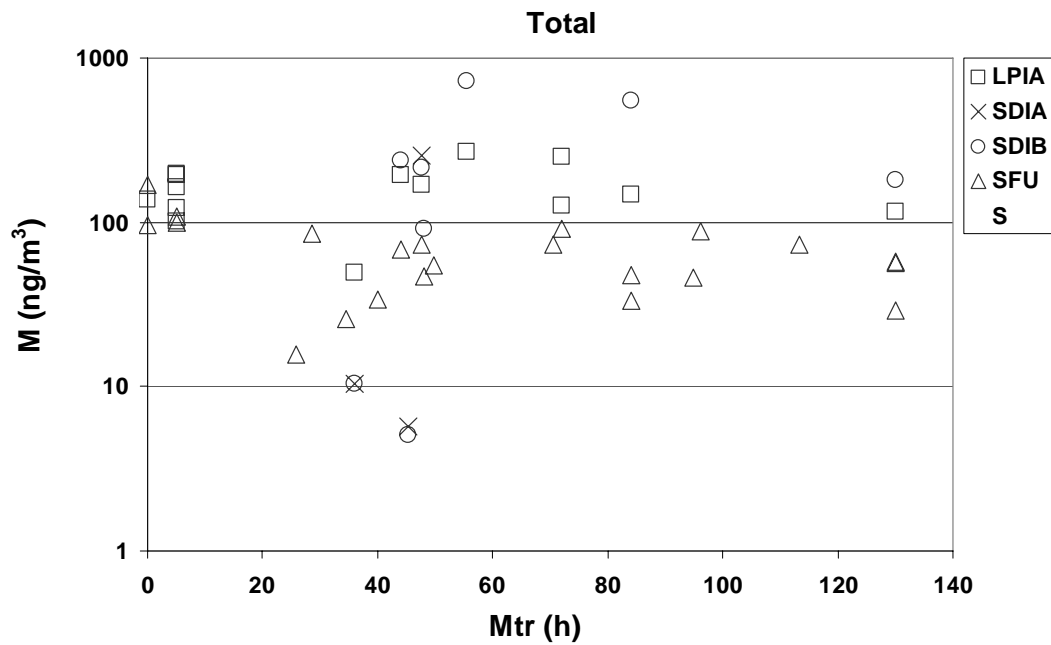


Figure 7a. Total mass concentration (ng/m<sup>3</sup>) of S for the SFU, LPI and SDI samples as a function of as a function of Mtr.

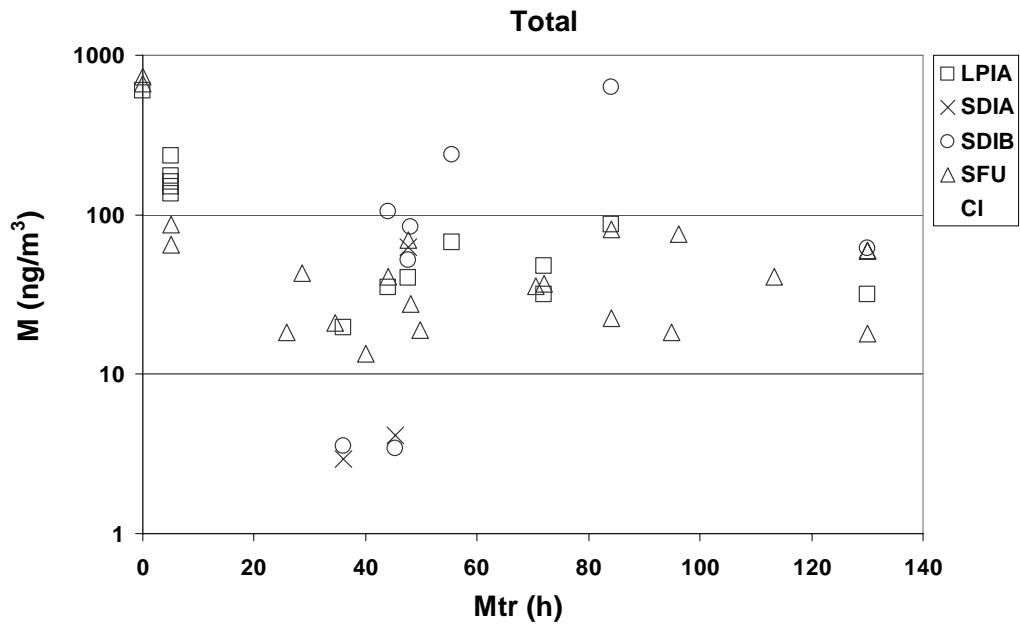


Figure 7b. Total mass concentration (ng/m<sup>3</sup>) of Cl for all samplers, SDI, LPI and SFU, as a function of Mtr.

An extensive meteorological program was carried out during AOE-2001 (Tjernström, 2005). One distinct meteorological feature found was a shallow (~200 m) boundary layer capped by very strong inversion that suppressed mixing from above. Such down-mixing is thus both intermittent and infrequent. Nilsson and C. Leck (2002), however, conclude that at Mtr = 96 h the entrainment of air from the free troposphere (FT) corresponds to a steady-state sulphur source to the ABL of  $3 \cdot 10^{-7} \text{ nmol} \cdot \text{m}^{-3} \cdot \text{s}^{-1}$ , to be compared with a production rate of sulphate from  $\text{SO}_2$  of  $2 \cdot 10^{-7} \text{ nmol} \cdot \text{m}^{-3} \cdot \text{s}^{-1}$ . These sources are balanced by a loss to the sea surface of  $5 \cdot 10^{-7} \text{ nmol} \cdot \text{m}^{-3} \cdot \text{s}^{-1}$ .

No corresponding analysis has been carried out for chlorine, but it is unlikely that there is transport of sea salt particles within the FT sufficient to sustain the observed chlorine mass concentrations far into the pack ice.

Vertical aerosol profiling was conducted in the vicinity of the icebreaker during AOE-2001. During some of these flights, well-confined layers of particles  $>300 \text{ nm}$  were observed above the ABL. At least one of these could be traced backwards in time to forest fires that had occurred in northeastern Siberia. Otherwise, during the summers there is rather infrequent atmospheric transport of air within ABL and FT to the central Arctic Ocean, so that the concentrations of anthropogenic pollutants are usually low.



## 4. Discussion and conclusions

The elements Si, S, Cl, K, Ca, Ti, Fe, Ni, Zn and Br were normally found at concentrations above the detection limit, also within the pack ice at 88° - 89° N. The finding that the elemental concentrations did not decay exponentially with transport time since the last contact with open water is a strong indication that there are sources of aerosol particles within the pack ice region of the high Arctic during the summers.

Two sources of primary aerosol particles were identified: sea salt and crustal or biogenic sources. Primary aerosol particles from both sources were released by bubble bursting in the open leads between ice floes. The strength of the sea salt source increased with an increase in local wind speed, also over the pack ice, where the open leads were often too narrow to allow extensive wave formation or whitecapping to occur. The sea salt source contributed mainly to the presence of coarse aerosols, which had a mode for the mass size distribution of Cl, K, Ca and S of around 1-2  $\mu\text{m}$ . Secondary DMS-derived sulphur compounds (S) were found mainly in the fine-mode aerosols.

The source of those primary aerosol particles that contributed to the concentration of the elements Si, K, Ca, Ti, Fe and Zn had a composition similar to the average concentrations of these elements in crustal rocks. Minerals originating from the Siberian river runoff into the Laptev and Kara Seas are transported to the high Arctic continually through ice-rafting by way of the Transpolar Current. The crustal-like sources of primary aerosol particles may also be the result of the processing of minerals by the Arctic Ocean biota prior to their being ejected into the atmosphere through bubble bursting.

The processes and conditions that are important for the production of aerosol particles of crustal-like composition in the high-Arctic during the summers would appear to be the following:

- i) The inflow of crustal material of continental origin originating from Siberian river outflow and ice-rafted to the high Arctic by way of the Transpolar current;
- ii) Bubble bursting, which ejects solid particles into the atmosphere from the SML or from the sea water below.
- iii) The open water found in the leads between the ice floes.

All three of these are potentially sensitive to changes in climate. Thawing of the permafrost in Siberia can increase the river runoff and thus increase the influx of crustal material to the Arctic Ocean. The pattern of ice flow responds to the Arctic Oscillation index, which in turn has been linked to changes in climate. The areal coverage of the pack ice in the Arctic Ocean

during the summers is decreasing quite rapidly (Comiso, 2003). This leads to a continual increase in the fraction of open water, which in turn contributes to bubble bursting. It also reduces the transport efficiency of ice-rafting, which is partly dependent upon the amounts of multi-year ice that are found. The input of Aeolian dust is also likely to increase as the snow cover decreases in both its extent and its persistence.

## **Acknowledgements**

This work was supported by the Swedish Polar Research Secretariat, the Swedish Research Council and the Nordic Council of Ministers through the Nordic Arctic Research Programme. The authors wish to thank the crew that operated the Swedish icebreaker *Oden* during the Arctic Ocean expedition 2001, as well as our colleagues at Lund University that helped us with the PIXE analysis.

## References

- ACIA, 2004: Impacts of a Warming Arctic, Arctic Climate Impact Assessment, Cambridge Univ. Press.
- Andersson, Per, Personal communication (2005) Swedish Museum of Natural History, Laboratory for Isotope Geology (LIG), P.O. Box 50007, SE-104 05 Stockholm, Sweden
- Barrie, L.A., Hoff, R.M., Fine years of air chemistry observations in the Canadian Arctic, *Atmospheric Environment* 19(1985)1995-2010.
- Bigg, E.K. and Leck, C., Cloud-active particles over the central Arctic Ocean, *J. Geophys. Res.* Vol. 106, No. D23(2001)32155-32166.
- Comiso, J. C., 2003: Sea ice concentration, ice temperature, and snow depth, using AMSR-E data, *IEEE TGRS*, 41(2), 243-252.
- Comiso, J.C., 2002: A rapidly declining perennial sea ice cover in the Arctic. *Geophys Res. Lett.*, 29, 10.1029/2002GL015659.
- Gustafsson, Ö., Andersson, P., Axelman, J., Bucheli, T.D., Kömp, P., McLachlan, M.S., Sobek, A. and Thörngren, J.-O. Observations of the PCB distribution within and in-between ice, snow, ice-rafted debris, ice-interstitial water, and seawater in the Barents Sea marginal ice zone and the North Pole area. *Science of the Total Environment*, 342(2005)261–279.
- Heintzenberg, J., Leck, C., Birmili, W., Wehner, B., Thernström, M. and Wiedensohler, A. Aerosol number-size distributions during clear and fog periods in the summer high Arctic: 1991, 1996 and 2001. *Tellus* (2006), In press.
- Hillamo, R. Development of inertial impactor size spectroscopy for atmospheric aerosols, PhD thesis (1994). University of Helsinki, Finnish Meteorological Institute Contributions No. 14, Helsinki 1994.
- Hillamo, R., Kerminen, V.-M., Aurela, M., Mäkelä, T., Maenhaut, W., Leck, C., Modal structure of chemical mass size distribution in the high Arctic aerosol, *J. Geophys. Res.* Vol. 106, No. D21(2001)27555-27571.
- Intrieri, J. M., C. W. Fairall, M. D. Shupe, P. O. G. Persson, E. L. Andreas, P. S. Guest, and R. E. Moritz (2002), An annual cycle of Arctic surface cloud forcing at SHEBA, *J. Geophys. Res.*, 107(C10), 8039, doi:10.1029/2000JC000439.
- Leck, C., and E.K. Bigg, Aerosol production over remote marine areas - A new route, *Geophys. Res. Lett.*, 23(1999)3577-3581.
- Leck, C., Tjernström, M., Matrai, P. Swietlicki, E. and Bigg., K., Can Marine Micro-organisms Influence Melting of the Arctic Pack Ice? *EOS*, 85(2004)25-32.

- Liu, k.& Dickhut, R., Effects of wind speed and particulate matter sources on surface microlayer characteristics and enrichment of organic matter in southern Chesapeake Bay, *Journal of Geophysical Research*, 103(1998)10571-10577.
- Maenhaut, W., Hillamo, R., Mäkelä, T., Jaffrezo, J.-L., Bergin, M.H., Davidson, C.I. A new cascade impactor for aerosol sampling with subsequent PIXE analysis. *Nucl. Instr and Meth. B*109/110(1996a)482-487.
- Maenhaut, W., Ducastel, G., Leck, C., Nilsson, E.D., Heintzenberg, J., Multi-elemental composition an sources of the high Arctic atmospheric aerosol during summer and autumn. *Tellus* 48B(1996b)300-321.
- Grammatika, M. and Zimmerman W.B., Micohydrodynamics of flotation processes in the sea surface layer, *Dynamics of Atmospheres and Oceans*, 34(2001)327-348.
- Nilsson, E.D., and C. Leck, A pseudo-Lagrangian study of the arctic remote marine sulphur cycle. *Tellus* 54B(2002)213-230.
- Papapiropoulos G., B.G. Martinsson, A. Zahn, C.A.M. Brenninkmeijer, M. Hermann, J. Heintzenberg, H. Fischer and P.F.J. van Velthoven. Aerosol elemental concentrations in the tropopause region from intercontinental flights with the CARIBIC platform, *J. Geophys. Res.* 107(D23), 4671, doi: 10.1029/2002JD002344, 2002.
- Riley J.P. and Skirrow G., *Chemical Oceanography*; Academic Press. 1975.
- Shariff, A. “Development of New Experimental Facilities at the Lund Nuclear Microprobe Laboratory”, Lund University, Ph-D thesis (2004).
- Taylor, S.R. and McLennan, S.M., *The Continental Crust: its Composition and Evolution*, Blackwell Scientific Publications (1985).
- Tjernström, M., The summer Arctic boundary layer during the Arctic Ocean Experiment 2001 (AOE-2001). *Boundary-Layer Meteorology*, 117(2005)5-36.
- Tréguer, P., Nelson, D.M., Van Bennekom, A.J., DeMaster, D.J., Leynaert, A., Quéguiner, B., The silica balance in the world ocean; A reestimate, *Science* 268(1995)375-379.
- Wurl O. and Obbard, J.P., A review of pollutants in the sea-surface microlayer (SML): a unique habitat for marine organisms, *Marine Pollution Bulletin* 48(2004)1016-1030.

**II**

# Summer aerosol particles in the high Arctic classified using Transmission Electron Microscopy

Arash Gharibi <sup>a,\*</sup>, Keith Bigg <sup>b</sup>, Erik Swietlicki <sup>a</sup>, Caroline Leck <sup>b</sup>

<sup>a</sup> Division of Nuclear Physics, Lund University, P.O. Box 118, SE-221 00 Lund, Sweden

<sup>b</sup> Meteorological Institute of Stockholm University (S-106 91 Stockholm)

## Abstract

As part of an atmospheric research programme involving a trip to the Arctic Ocean on the Swedish icebreaker *Oden* in the summer of 2001, aerosol particles were collected for subsequent analysis by transmission electron microscopy. The aerosol particles collected within the pack ice between 88°-89° N were classified according to their morphology into the following types: sea salt, ammonium sulphate, ammonium bisulphate, sulphuric acid mixtures, mixtures of sulphuric acid and methanesulphonic acid (MSA), compact aggregates, bacteria, microorganisms, solids, and unknowns. These particle types were further categorized as being either of primary or secondary origin. A total of 322 aerosol particles were examined and the frequency of each particle type was determined.

Most particles consisted of sulphuric acid in various mixtures with methane sulphonic acid (MSA), and they often contained solid inclusions. The primary aerosol particles other than sea salt (compact aggregates bacteria, microorganisms, and solids) showed a temporal variability that closely resembled that of the nearly-hydrophobic particles as determined by an H-TDMA (Hygroscopic Tandem Differential Mobility Analyser) operating at dry particle sizes of 110-165 nm. This indicates that primary aerosol particles that were originally solid and nearly-hydrophobic were formed in the pack ice region and were eventually transformed by the condensation of DMS-derived sulphur-containing compounds to become more hygroscopic. The climatic significance of these findings is that it shows that these primary particles can act as a site of condensation for vapours such as sulphuric acid or MSA, facilitating the formation of clouds and fogs that have a large impact on the radiative balance.

---

\* Corresponding author: arash.gharibi@nuclear.lu.se

## 1. Introduction

The Arctic is a region that is particularly sensitive to changes in climate, the temperature rising faster here than in any other regions on earth (ACIA, 2004). Clouds play a key role in the radiative balance within the Arctic pack ice region, and can either mitigate or aggravate climatic changes, depending upon the response of the Arctic boundary layer clouds to global warming and the melting of the pack ice (Comiso, 2002).

The production of aerosol particles that can readily serve as cloud condensation nuclei (CCN) at the water vapour supersaturations found in the Arctic stratocumulus clouds is one of the most uncertain elements in the prediction of changes in Arctic climate. It is well known that dimethyl sulphide (DMS) is released to sea water through the grazing by marine zooplankton on phytoplankton and algae and through bacterial attack. Secondary sulphur-containing compounds such as sulphuric acid and methane sulphonate (MSA) are produced by the gas-phase oxidation of  $\text{SO}_2$  and other DMS-derived gaseous compounds. Oceanic emissions of dimethyl sulphide (DMS) to the atmosphere constitute a major source of secondary aerosols in the Arctic (e.g. Leck and Persson, 1996). The open water and marginal ice zone regions surrounding the Arctic pack ice are the major source of DMS. The production of primary particles is important since these can act as condensation sites for various vapours and thus increase the rate at which CCN are produced.

As part of an atmospheric research programme involving a trip to the Arctic Ocean on the Swedish ice breaker *Oden* in the summer of 2001 (Leck et al., 2004), aerosol particles were collected for subsequent analysis by means of transmission electron microscopy. The aerosol particles collected within the pack ice at  $88^\circ$ - $89^\circ$  N were classified according to their morphology into several types. The primary aerosol particles other than sea salt were of particular interest, due to their importance in maintaining the particle population in the Arctic boundary layer within the pack ice region. These were compared with the nearly-hydrophobic particles determined by an H-TDMA (Hygroscopic Tandem Differential Mobility Analyser) operating at dry particle sizes of 110-165 nm.

The major objective of the measurements presented here was, through use of the single-particle analytical techniques that were available, to obtain information regarding the sources and the processes that contribute to production of the Arctic summer aerosols.

## 2 Sampling and TEM analysis

The aerosol particles were collected on copper TEM grids ( $\varnothing = 3$  mm), using a polyvinylbutyral (“butvar”) collecting surface. Three types of collection devices were employed: impactors of two types and an electrostatic precipitator (ESP). The first type of impactors had a round nozzle ( $\varnothing = 500$  nm), a flow rate of  $30 \text{ ml}\cdot\text{s}^{-1}$ , and a 50% collection efficiency at an equivalent aerodynamic diameter (EAD) of 160 nm. The second type were low-pressure impactors with a flow rate of  $1.3 \text{ ml}\cdot\text{s}^{-1}$ , their having a  $\varnothing = 75 \text{ }\mu\text{m}$  circular electron microscope aperture as a nozzle. In addition, an electrostatic precipitator (ESP) was employed, having a  $^{63}\text{Ni}$  radioactive source as an aerosol bipolar charger, a  $12 \text{ kV}\cdot\text{cm}^{-1}$  electric field between the anode and the cathode plate, and a very low flow rate of  $0.17 \text{ ml}\cdot\text{s}^{-1}$ . This latter device allowed aerosol particles up to 1 mm in diameter to be sampled (Leck and Bigg, 2005).

A total of 322 individual aerosol particles were studied using TEM (Transmission Electron Microscopy). The TEM analysis involved the grid to be examined being scanned first at low magnification to obtain an overall view of the aerosol particle loading and the types of particles being collected. Contaminated or damaged grids were discarded already at this stage. The TEM operator then zoomed in on smaller parts of the grid that were considered typical for the entire grid. Within these selected areas, images of individual particles were made at high magnification. Care was taken to select individual particles randomly, so that the selection would be representative of the entire particle population collected on the grids. Unless particles were explicitly examined for beam damage, they were illuminated as briefly as possible before an image was recorded.



### 3. Common particle types

The 322 individual particles examined by use of TEM displayed a high degree of variability with respect to morphology, size and composition. These particles could nevertheless be classified into several different types on the basis of the earlier experience of with the single-particle electron microscopy analysis of aerosol particles from the high Arctic (Bigg and Leck, 2001a; Bigg and Leck, 2001b). The classification also facilitated both interpretation of the data and comparison of the results with those of other single-particle analytical techniques. The following set of common particle types was used in classification:

- Sea salt (SS)
- Ammonium sulphate (AS)
- Ammonium bisulphate (ABS)
- Sulphuric acid mixtures (SAM)
- Mixtures of Sulphuric acid and MSA (SAMM)
- Compact Aggregates (CA)
- Bacteria (B)
- Microorganisms (MO)
- Solids (S)
- Unknowns (U)

These particle types were categorized further as being of either primary or secondary origin. The AS, ABS, SAM, and SAMM particle types were clearly secondary aerosol particles (SAP), whereas the types CA, B, MO, and S were categorized as being primary aerosol particles (PAP) other than sea salt (SS). This resulted in four categories altogether: SAP, PAP, SS, and U.

Note that in Figure 1 the electron-absorbent material appears white and the shadows black, except in the pictures 2 and 3, where the colours are switched. The size of each particle was calculated from the length of its shadow. The length of the shadow is equal to the diameter of the equivalent sphere (i.e. the diameter of a sphere of the same volume). Further details of treatment of the individual particles and of the classification of the TEM images can be found in Bigg and Leck (2001a).

### **Sea salt (SS)**

Particles containing sea salt usually have a crystal-like structure. Picture 1 in Figure 1 shows a TEM image of a particle collected over the Arctic Ocean in 2001 having this special property. It illustrates the general structure of a NaCl crystal that also contains other material. The great majority of the salt particles are >200 nm in diameter.

### **Ammonium sulphate (AS)**

Ammonium sulphate, which is in liquid form when collected, has a contact angle of nearly 90 degrees with the grid surface and protrudes upwards as a hemisphere (Picture 2). In a combination of ammonium sulphate and organic material, an ammonium sulphate particle appears as a spherical cap (Picture 3), one which in this form is considerably less sensitive to heat from the electron beam.

### **Ammonium bisulphate (ABS)**

The crystallisation of ammonium bisulphate produced by nebulizing a solution and collecting the liquid droplets takes place explosively when the particles are subjected to a vacuum, pieces being thrown out then and the surface becoming rough. Atmospheric bisulphate particles almost always are flatter and less coarse in their crystallisation, probably because of their organic content (Picture 4). When ABS is mixed with methane sulphonic acid, no grainy structure appears, bright cracks being present, as can be seen in Picture 5.

### **Sulphuric acid mixtures (SAM)**

Sulphuric acid mixtures can form droplet halos. Their appearance depends upon the purity of the sulphuric acid. If the droplet particles contain a relatively pure sulphuric acid mixture, the droplet rings produced are quite extensive, each of the droplets being very small. They are nearly hemispherical in shape, as in the example shown in Picture 6. As the content of other compounds increases, the droplets tend to become fewer and larger (Picture 7). In Picture 8, the central particle appears to contain small particles from the surface microlayer, whereas surface-active components result in the droplet rings being very flat (Bigg et al., 2004).

## **Mixtures of Sulphuric acid and MSA (SAMM)**

Since pure methane sulphonic acid is unstable when an electron beam is directed at it, obtaining a TEM image of it is difficult. Nevertheless, some of the particles found in the Arctic very similar in appearance to SAMM were sufficiently stable to be analysed by TEM (Picture 9). When ammonium bisulphate is mixed with ammonium sulphate, the resulting particles are quite stable, see Picture 10. Mixing ammonium sulphate with MSA results in flat discs like the one shown in Picture 11.

## **Compact Aggregates (CA)**

When two groups of particles come in contact with each other, they can combine to form either larger particles or a compact aggregate. Aggregated aerosol particles are easily recognised in a TEM image, being very distinct in their appearance. Since most of the compact aggregates studied contained only traces of inorganic elements, mainly Si and P, we concluded that both the aggregates and their smaller components were almost entirely organic. A compact aggregate containing particles 20-50 nm in size is shown in Picture 12.

## **Bacteria (B) and Microorganisms (MO)**

Bacteria, together with small unknown organisms and parts of larger creatures, were found to varying degrees in the Arctic samples. In addition, the air contained numerous bacteria ranging from 100 nm to about 1  $\mu$ m in length, together with many other distinctive microorganisms. An example of a bacterium is presented in Picture 13 and an example of a virus-like particle in Picture 14.

## **Solids (S)**

When the magnification is held constant, increasing the intensity of the electron beam leads to an increase in the heat applied to the sample. Solid particles are usually very heat-resistant and yield a clear TEM image. Almost no electrons pass through them, which makes their image very dark. In most of the pictures the colours have been switched to make the shadows black. A particle of the solid type is shown in Picture 15.

## **Unknowns (U)**

Particles that could not be included in any of the types just mentioned were classified as unknown. An example is shown in Picture 16.

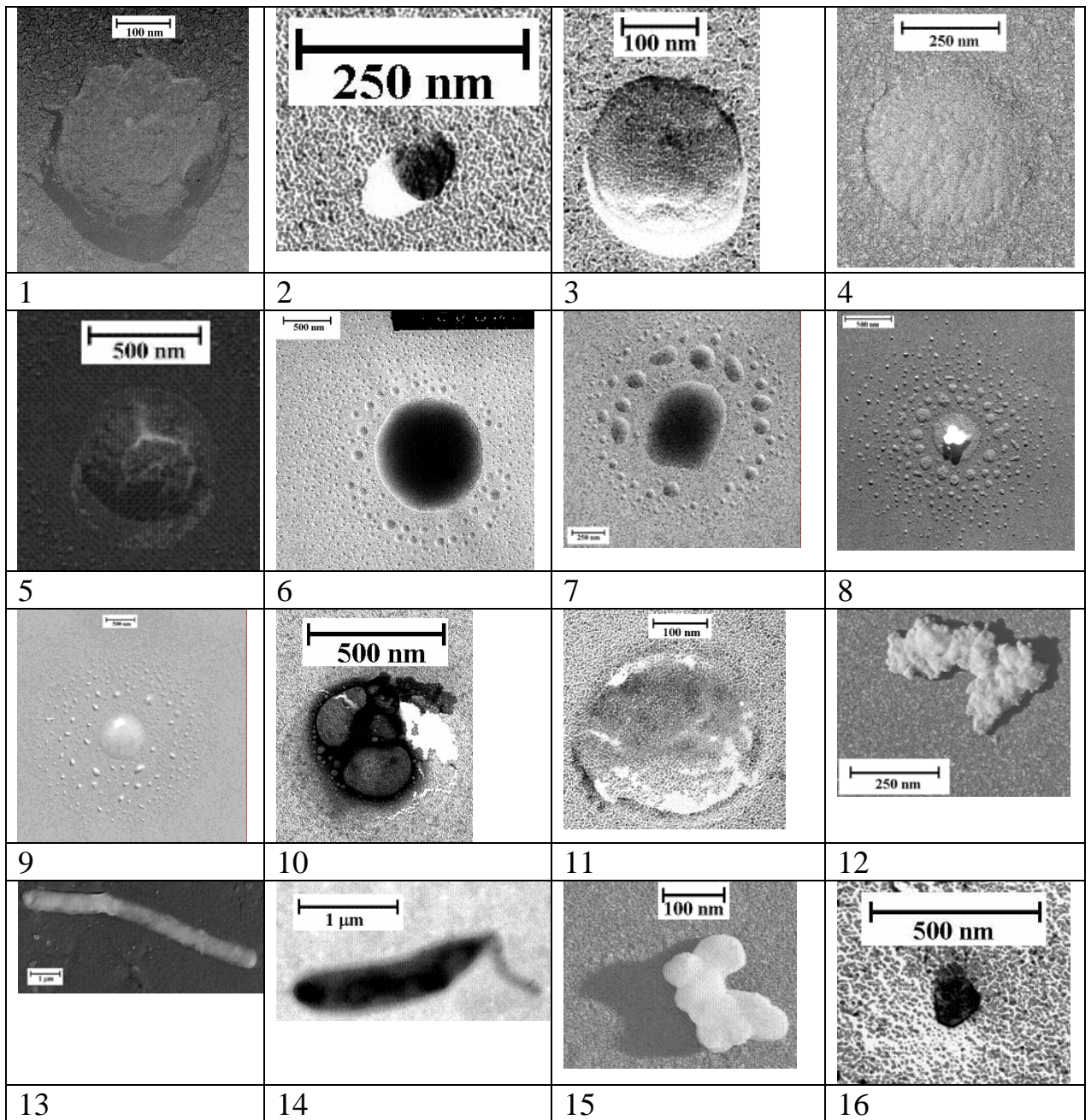


Figure 1. TEM images of the common particle types (CPT), the shadows being black in all the images except for 2 and 3, in which the colour is switched so that the shadow appears white.

#### 4. Particle-type statistics

All 322 particles that were examined by TEM could be classified. The frequency of each particle type is shown in Figure 3. Most of the particles studied were classified as SAM or SAMM. The third largest type is U, involving the unknown particles.

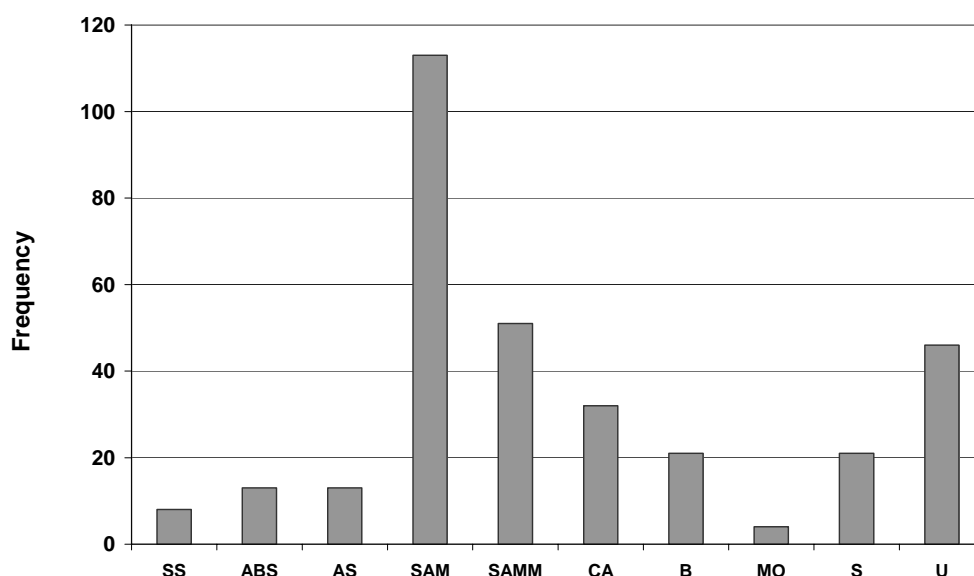


Figure 3. Frequency of the various particle types (n = 322).

In Figure 4, the relative frequencies of the four particle categories (PAP, SAP, SS and U) are plotted as a function of transport time over ice since the last contact with open water (Mtr). The samples that were collected over open water are plotted at 0 h, and those collected in the marginal ice zone at 5 h. Mtr was estimated on the basis of ice maps and air mass back trajectories.

Of particular interest in Figure 4 is the region in which Mtr > 35 h, since aerosol particles produced over the open sea or in the marginal ice zone are rapidly scavenged by frequent fogs and low clouds when transported over the pack ice within the Arctic boundary layer. Nilsson and Leck (2002) estimate the turnover time for sulphate and MSA in the Arctic boundary layer over pack ice to be ~18 h.

As shown in Figure 4, the aerosol fraction of SAP is 90-100% at eight out of thirteen Mtr. These secondary particles, containing various DMS-derived sulphur compounds, appear to completely dominate the number concentration except during certain distinct periods of time, in which PAP are more frequent. Production of sulphate and MSA also takes place over the pack ice, since the turnover time for DMS(g) over the pack ice was estimated to be significantly longer (~59 h) than that of sulphate and MSA (Nilsson and Leck, 2002).

PAP dominated the aerosol number fraction on two occasions (Mtr = 43 h on August 19, 2001; Mtr = 84 h on August 8, 2001), both of which occurred during the ice drift when the ship was moored to an ice floe. The ice drift period started on August 1, 2001 near latitude 89.0° N, longitude 1.8° E, and ended on August 22 at 88.2° N, 9.4° W. Note that 41% of the PAP fraction consisted of CA. August 8 was the first sunny day with clear skies encountered since the start of the ice drift period, and measurements of the sub-micrometer aerosol particle number size distribution then observed the formation of particles at ~25 nm (Heintzenberg et al., 2006). On August 19, the maximum in the aerosol particle number size distribution was found at ~200 nm.

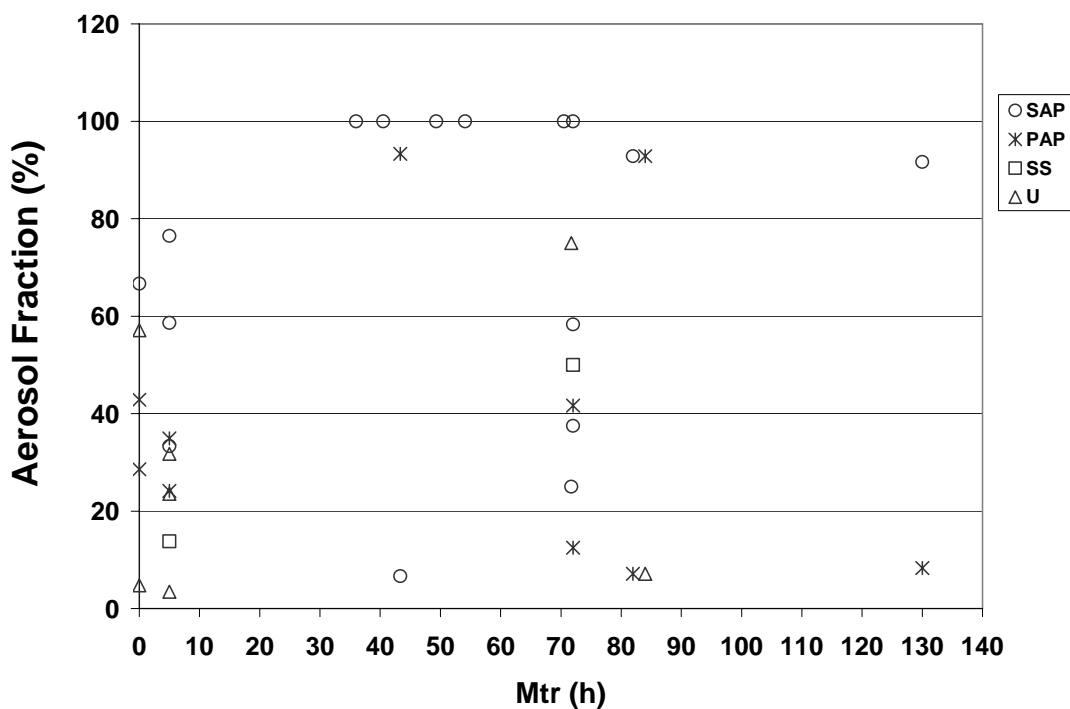


Figure 4. The relative aerosol fractions of the various particle types (%) as a function of transport time over ice since the last contact with open water (Mtr).

## 5. Comparison of hygroscopic properties

During the AOE-2001 expedition, the hygroscopic properties of aerosol particles were measured for dry particles between 20 and 165 nm in size by use of a Hygroscopic Tandem Differential Mobility Analyser (H-TDMA). The instrument measures the diameter growth factor of individual aerosol particles taken from a dry state to a relative humidity of 90%. The H-TDMA is capable of distinguishing between particles of the same dry size but differing in hygroscopic growth (Rissler, et al., 2005). It is thus capable of determining the degree of internal or external mixing of the aerosol in question. During the icebreaker expedition to this same region in the summer of 1996, the particles were classified in three groups on the basis of their hygroscopic growth: more-hygroscopic, less-hygroscopic and sea salt particles (Zhou, et al., 2001). During the 2001 expedition, the more-hygroscopic particles dominated, as they also did in 1996. The occurrence of nearly-hydrophobic particles, however, was much more frequent in 2001 than in 1996, possibly because of the three-week ice drift period when H-TDMA measurements were carried out continuously, which was not the case in 1996, when aerosol measurements were only conducted during brief periods of time while at station along the route.

Figure 5 examines, for the aerosol particles with dry diameters of 110 and 165 nm, relations between the number fractions of the aerosol particles as determined by TEM single-particle analysis and their hygroscopic properties as determined by the H-TDMA instrument. The determination of the various aerosol fractions on the basis of TEM and H-TDMA single-particle analysis were conducted entirely independently of each other up to the point where the fractions were compared, as shown in Figure 5. No re-classification was undertaken following this comparison.

For the H-TDMA data, the more-hygroscopic particles are denoted as AF0, and the nearly-hydrophobic particles as AF1. The more-hygroscopic particles the H-TDMA provides corresponded to the SAP particles as determined by use of TEM. This was expected, since sulphate mixtures have high growth factors that result in more-hygroscopic particles being detected by the H-TDMA.

Also of interest is the observation that the nearly-hydrophobic particles obtained from H-TDMA (AF1) have a temporal variability that closely resembles that of the primary aerosol particles (PAP) identified in the TEM analysis. Furthermore, these primary nearly-hydrophobic particles also appear at long Mtr times. This indicates that the particles that are being formed in the pack ice region were originally solid and nearly-hydrophobic, and that the particles were transformed then by condensation of the DMS-derived sulphur-containing compounds to eventually become more hygroscopic. The nearly-hydrophobic primary aerosol particles are either compact aggregates, microorganisms or unidentified solids. The latter are very heat-resistant and electron-dense. They generate clear TEM images with sharp contours.



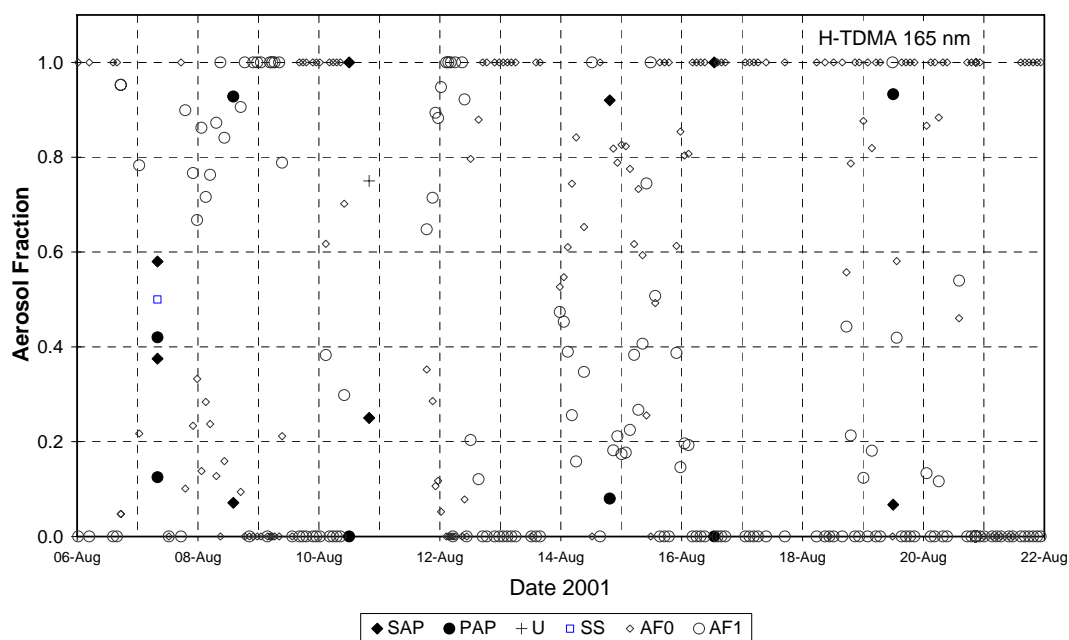
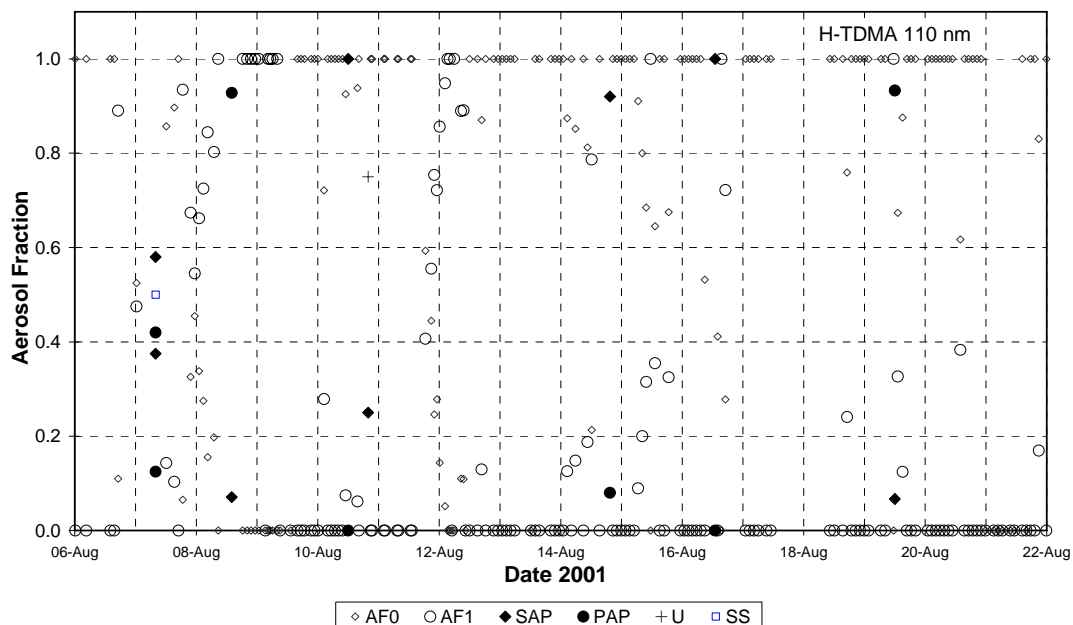


Figure 5. Relations at 110 and 165 nm between the aerosol number fractions determined by TEM single-particle analysis and the hygroscopic properties of the particles. H-TDMA: AF0 more-hygroscopic particles; AF1; nearly-hydrophobic particles; TEM: SAP/PAP or secondary/primary aerosol particles.

## 5. Discussion and conclusions

During AOE-2001, aerosol particles in the size range of 20-165 nm classified by the H-TDMA as belonging to the more-hygroscopic group showed a frequency of occurrence of 83-92%, depending on their dry size. The average growth factors (dry to RH=90%) varied between 1.49 and 1.62. For comparison, a 100 nm particle of pure ammonium sulphate has a growth factor of 1.74, that of ammonium bisulphate being slightly higher. This indicates that the particles are not entirely soluble and have an insoluble core. The frequency of occurrence of the nearly-hydrophobic particles was considerably lower (observed in 23-42% of all the H-TDMA scans), the highest frequencies being in the size range of 50-165 nm. The corresponding average growth factors were 1.01-1.11.

Gharibi and Swietlicki (2006) used size-resolved elemental analysis of impactor samples to obtain information regarding the sources of aerosol particles within the pack ice between 88° and 89° N during AOE-2001. Two sources of primary aerosol particles were identified: sea salt and a crustal and/or biogenic source. Secondary DMS-derived sulphur compounds were found mainly in the fine mode aerosols. According to Gharibi and Swietlicki (2006), the source of primary aerosol particles contributing to the concentrations of the elements Si, K, Ca, Ti, Fe and Zn has a composition similar to that of average crustal rock. The minerals originate from Siberian river runoff into the Laptev and Kara Seas. They and are ice-rafted to the high Arctic by the Transpolar Current.

This primary crustal and/or biogenic source may well be identical to that of the nearly-hydrophobic particles observed by the H-TDMA and the primary aerosol particles (PAP) identified by means of TEM single-particle analysis. As discussed in Gharibi and Swietlicki (2006), the source strength of these primary aerosol particles is dependent upon bubble bursting that ejects solid particles into the atmosphere from the surface microlayer of the sea or from the sea water below. In the pack ice region, this process can obviously only take place in the open leads between ice floes.

The climatic significance of these findings is that these primary particles can act as a site of condensation for condensable vapours such as sulphuric acid and MSA. If these primary particles are 100 nm in size or larger, only a small mass fraction of soluble material is needed for them to be active as CCN (Cloud Condensation Nuclei) at the low supersaturations found in stratocumulus clouds. The important thing here is that primary particles are actually formed in the Arctic boundary layer, whatever the composition of the primary particles may be. The alternative route for secondary particle production would otherwise be the homogeneous nucleation of gas-phase precursors, most likely through the ternary nucleation of sulphuric acid, water vapour and ammonia. Since the vapour concentration of sulphuric acid is likely to be very low, such nucleation is probably of less importance for sustaining the particle number concentrations within the Arctic pack ice than any other source of primary particles are.

### **Acknowledgements**

This work was supported by the Swedish Polar Research Secretariat, the Swedish Research Council and the Nordic Council of Ministers within the framework of the Nordic Arctic Research Programme. The authors wish to thank the crew that operated the Swedish icebreaker *Oden* during the Arctic Ocean expedition 2001, as well as the members of the Electron Microscopy Unit of the Faculty of Medicine at Lund University, in particular Dr. Eric Carlemalm, Rolf Odselius and Lina Gefors.

## References

- ACIA, 2004: Impacts of a Warming Arctic, Arctic Climate Impact Assessment, Cambridge Univ. Press.
- Bigg E. K. and C. Leck, Properties of the aerosol over the central Arctic Ocean. *J. Geophys. Res.* 106 D23(2001a)32101-32110.
- Bigg E. K. and C. Leck, Cloud-active particles over the central Arctic Ocean,. *J. Geophys. Res.* 106 D23(2001b)32155-32166.
- Bigg, E.K., C. Leck and L. Tranvik, Particulates of the surface microlayer of open water in the central Arctic Ocean in summer, *Marine Chemistry* 91(2004)131-141.
- Comiso, J.C., 2002: A rapidly declining perennial sea ice cover in the Arctic. *Geophys Res. Lett.* 29, 10.1029/2002GL015659.
- Gharibi and Swietlicki (2006). Aerosol particle elemental size distributions during the Arctic Ocean expedition summer 2001, Manuscript in preparation.
- Heintzenberg, J., Leck, C., Birmili, W., Wehner, B., Thernström, M. and Wiedensholer, A. Aerosol number-size distributions during clear and fog periods in the summer high Arctic: 1991, 1996 and 2001. *Tellus* (2006), In press.
- Leck, C. and C. Persson, Seasonal and short-term variability in dimethyl sulfide, sulfur dioxide and biogenic sulfur and sea salt aerosol particles in the arctic marine boundary layer, during summer and autumn. *Tellus* 48B(1996)272-299.
- Leck, C., Tjernström, M., Matrai, P. Swietlicki, E. & Bigg., K.. Can Marine Micro-organisms Influence Melting of the Arctic Pack Ice? *EOS*, 85(2004)25-32.
- Leck C. and Bigg E. K., Biogenic particles in the surface microlayer and overlaying atmosphere in the central Arctic Ocean during summer, *Tellus* 57B(2005 )305-316,
- Nilsson, E.D., and C. Leck, , A pseudo-Lagrangian study of the arctic remote marine sulphur cycle. *Tellus* 54B(2002)213-230.
- Rissler, J., Vestin, A., Swietlicki, E., Fisch, G., Zhou, J., Artaxo, P. and Andreae, M.O., Size distribution and hygroscopic properties of aerosol particles from dry-season biomass burning in Amazonia. *Atmos. Chem. Phys. Discuss.*, 5(2005)8149-8207.
- Zhou, J., Swietlicki, E., Berg, O.H., Aalto, P.P., Hämeri, K., Nilsson, E.D. and Leck C., Hygroscopic properties of aerosol particles over the central Arctic Ocean during summer. *J. Geophys. Res.* 106 D23(2001)32111-32124.

**III**



ELSEVIER

SCIENCE @ DIRECT®

Atmospheric Environment ■ (■■■■) ■■■-■■■

ATMOSPHERIC  
ENVIRONMENT[www.elsevier.com/locate/atmosenv](http://www.elsevier.com/locate/atmosenv)

## Traffic-generated emissions of ultrafine particles from pavement–tire interface

Andreas Dahl<sup>a,\*</sup>, Arash Gharibi<sup>b</sup>, Erik Swietlicki<sup>b</sup>, Anders Gudmundsson<sup>a</sup>,  
Mats Bohgard<sup>a</sup>, Anders Ljungman<sup>c</sup>, Göran Blomqvist<sup>d</sup>, Mats Gustafsson<sup>d</sup>

<sup>a</sup>Division of Ergonomics and Aerosol Technology, Lund University, P.O. Box 118, SE-221 00 Lund, Sweden

<sup>b</sup>Division of Nuclear Physics, Lund University, P.O. Box 118, SE-221 00 Lund, Sweden

<sup>c</sup>Division of Occupational and Environmental Medicine, Department of Molecular and Clinical Medicine, Faculty of Health Sciences, Linköping University, SE-581 85 Linköping, Sweden

<sup>d</sup>Swedish National Road and Transport Research Institute (VTI), SE-582 95 Linköping, Sweden

Received 31 March 2005; received in revised form 4 October 2005; accepted 14 October 2005

### Abstract

In a road simulator study, a significant source of sub-micrometer fine particles produced by the road–tire interface was observed. Since the particle size distribution and source strength is dependent on the type of tire used, it is likely that these particles largely originate from the tires, and not the road pavement. The particles consisted most likely of mineral oils from the softening filler and fragments of the carbon-reinforcing filler material (soot agglomerates). This identification was based on transmission electron microscopy studies of collected ultrafine wear particles and on-line thermal treatment using a thermodesorber.

The mean particle number diameters were between 15–50 nm, similar to those found in light duty vehicle (LDV) tail-pipe exhaust. A simple box model approach was used to estimate emission factors in the size interval 15–700 nm. The emission factors increased with increasing vehicle speed, and varied between  $3.7 \times 10^{11}$  and  $3.2 \times 10^{12}$  particles vehicle<sup>-1</sup> km<sup>-1</sup> at speeds of 50 and 70 km h<sup>-1</sup>. This corresponds to between 0.1–1% of tail-pipe emissions in real-world emission studies at similar speeds from a fleet of LDV with 95% gasoline and 5% diesel-fueled cars. The emission factors for particles originating from the road–tire interface were, however, similar in magnitude to particle number emission factors from liquefied petroleum gas-powered vehicles derived in test bench studies in Australia 2005. Thus the road–tire interface may be a significant contributor to particle emissions from ultraclean vehicles.

© 2005 Elsevier Ltd. All rights reserved.

**Keywords:** Road wear; Size distribution; Light duty vehicle; Nanoparticle; Emission factor

### 1. Introduction

Numerous epidemiological studies have shown that elevated outdoor particle concentrations measured as PM<sub>10</sub> (mass concentration of particles with an equivalent aerodynamic diameter < 10 μm) and PM<sub>2.5</sub>, or number concentrations of ultrafine

\*Corresponding author. Tel.: +46 46 222 95 98;  
fax: +46 46 222 44 31.

E-mail address: [andreas.dahl@design.lth.se](mailto:andreas.dahl@design.lth.se) (A. Dahl).

(<100 nm) particles, are associated with increased prevalence of respiratory and cardiovascular disease and mortality, both acute and chronic (Pope et al., 2002; Hoek et al., 2002; Katsouyanni et al., 2001; Peters et al., 2001; Pekkanen et al., 2002). WHO estimates that exposure to fine particulate matter in outdoor air leads to about 100,000 deaths annually in Europe (WHO, 2002; Ezzati et al., 2002). The toxicological mechanisms of ambient particle-related adverse effects on human health are only partly understood, although it has been suggested that ultrafine particles have stronger adverse health effects (Donaldson et al., 2001; Oberdorster et al., 1995). It is therefore of considerable interest to thoroughly characterize different particle types and sizes in order to relate their differing properties to observed effects.

Research conducted in recent years has shown that particles originating from the wear of the road, strongly contribute to the PM<sub>10</sub> concentrations near streets and roads in the Nordic countries during winter and early spring (Kupiainen et al., 2002). Because of this it is important to determine the particle emissions caused by traffic in order to provide the basis for efficient air-quality management. Toxicological studies on traffic-generated particles have mainly focused on exhaust particles. There is a need for more knowledge about the toxicological effects of wear particles. Since early 2003 the Swedish National Road and Transport Research Institute (VTI) has coordinated the project WearTox (Gustafsson et al., 2005) and its aims were to generate particles from studded tire wear of pavements, to characterize these particles and to study their toxicological effects on human airway cells. Different pavements have been used in the project and as comparison to the studded tires, non-studded tires were also used in the project.

Wear particles are usually larger than combustion particles (> 1 μm), and as expected, the study found that supermicrometer-sized mechanically generated particles totally dominated the particle mass. The properties of these coarse mode particles will be the subject of a separate paper. More surprisingly, a considerable amount of submicrometer particles were also generated, both from the studded and the non-studded set of tires, during the WearTox road simulator experiments, with a broad maximum in the size distribution, typically around 15–50 nm. This paper focuses on describing the observed properties of these particles. The main objective is

to identify the nature of this source of submicrometer particles and determine emission factors that can be used to compare their source strength with other traffic-generated emissions, mainly tail-pipe exhaust particles.

## 2. Experimental set-up

### 2.1. The VTI road simulator

Wear particles originating from the road–tire interface were generated in the VTI road simulator. Sampling in the simulator hall makes it possible to sample pure wear particles, with very low contamination from ambient particles and no influence from tail-pipe emissions. In all experiments presented here, the road simulator runs four wheels around a circular track. Each wheel axle is equipped with an electrical motor, which drives the rotation of the simulator. The speed can be varied between 0 and 70 km h<sup>-1</sup>. A linear track simulation is accomplished even though the tires are running in a circle, because no radial force is acting on the tires as the wheels are bolted to the axles of the road simulator. To make the wheels move radially across the entire track, an eccentric movement can be activated above 50 km h<sup>-1</sup>.

The simulator track can be equipped with any type of pavement and any type of light duty vehicle (LDV) tire can be mounted on the axles. No ventilation of the simulator hall was used, but pressure gradients might have caused minor self ventilation. The temperature in the hall ranged from 20 to 35 °C, but it was not governed with any air conditioner.

In the WearTox experiments, four combinations of tires and pavements were used:

1. Studded winter tires and an ABT (asphalt concrete) pavement with stone material from a local granite (Skårlunda granite). This pavement type is normally used on Swedish low- to medium-trafficked roads and has moderate wear resistance.
2. Studded winter tires and an ABS (stone mastic asphalt) pavement with stone material mainly from a quartzite (Kärr quartzite). This pavement type is used on Swedish highly trafficked roads and has high wear resistance.
3. Non-studded winter tires and ABS pavement.
4. Non-studded winter tires and a poroelastic road surface (PERS) developed and supplied by

Rosehill Polymers Ltd. The tiles are composed of rubber granules or fibers from scrap tires as the aggregate and urethane resin as the binder.

During the measurements the simulator was run at speeds corresponding to 30, 50 and 70 km h<sup>-1</sup> at the radius of the tires.

## 2.2. Aerosol characterization

The particle sizing at the VTI facilities was performed with a scanning mobility particle sizer (SMPS) system, consisting of a differential mobility analyzer (DMA) model 3071 (TSI Inc., USA) and a condensation particle counter (CPC) model 3010 (TSI Inc., USA). The aerosol and the sheath air flow rates were set to 0.31 and 31 min<sup>-1</sup>, respectively, giving a detectable size range of 15–700 nm. The SMPS system was placed outside the closed room housing the road simulator and the aerosol was sampled through a 2.0 m  $\frac{1}{4}$ " copper tube. During the testing sessions, the background aerosol was measured before starting the road simulator.

In addition, the aerosol was conditioned at different temperatures in order to observe the evaporation of substances from the aerosol particles. This was done using a thermodesorber (TD), which was derived from the original design of Burtcher et al. (2001) by Dahl and Pagels (2003). The TD consists of a heater and a desorber. The heater is a 550 mm long stainless steel tube with an inner diameter of 18 mm and with a heater coil wound around the tube. The desorber is placed downstream the heater and consists of a perforated 500 mm long tube, which is surrounded with activated carbon, which is used to adsorb the evaporated material. Using a DMA, selected specific particle sizes (40, 80, 160, 320 and 640 nm) of the wear particles were introduced into the TD, which was heated to different temperatures (75, 150 and 300 °C). Downstream the TD, the aerosol particle size distribution was then measured using the SMPS system. This combined DMA–TD–DMA–CPC set-up is referred to here as a Volatility Tandem DMA (VTDMA) (Orsini et al., 1999).

## 2.3. Electron microscopy

Electron microscopic studies were performed using a Philips CM10 transmission electron microscope (TEM). TEM was used to study the

morphology of fine aerosol particles emitted during wear of the road–tire interface, when the road simulator was equipped with the studded tires and the quartzite pavement (combination 2). The particles were collected with an electrostatic precipitator (ESP) directly onto electron microscopy copper grids that were covered with a thin electron-transparent carbon substrate prior to sampling. The precipitator was placed downstream of a DMA and was followed by a particle counter (CPC). This enabled sampling of charged particles of known mobility as well as an estimation of the number of particles collected on the grids. The ESP had a 100% removal efficiency for the particles studied in this session. After collection on the TEM grid substrate, artificial “shadows” were imposed on the collected particles before examination in an electron microscope. This was done in order to improve the contrast between the substrate and the small and almost electron-transparent particles. The shadowing was achieved in a vacuum chamber by firing a beam of metal atoms (Pt) onto the grids at an angle of 30°. The Pt shadow remained even if the particles were volatile during the heating of the electron beam during examination. A thick Pt shadow gives a 3-dimensional appearance, while the particles with a faint shadow provide more information about the sample thickness (electron density of the sample). The Pt metal tends to form small grains the size of a few nanometers on the sample substrate. These grains should not be mistaken for deposited aerosol particles. This grainy texture is more apparent in samples that have a relatively thick Pt cover, while nearly invisible in other TEM images.

## 3. Results

The results of the various analyses presented below were used to identify the nature of the source of submicrometer-sized particles seen in the road simulator experiments and to determine emission factors.

### 3.1. Particle size distribution

The background number concentration was measured before starting the road simulator during the testing sessions and it was between 1000 and 2000 particles cm<sup>-3</sup> at all events. After starting the road simulator, an aerosol is generated and the particle concentration reaches a steady state after approximately 1 h when the generation and the



deposition are balanced. The non-studded tires were run on the quartzite surface at 30, 50 and 70 km h<sup>-1</sup>. A particle number size distribution with a number concentration of 25,000 cm<sup>-3</sup>, a mean diameter of 27 nm and a geometric standard deviation of 1.5 was measured at 70 km h<sup>-1</sup> (Fig. 1). However, the size distribution was truncated, as the SMPS system had a particle size detection limit at 15 nm (i.e. more particles were generated than could be detected). As shown in Fig. 1, this is more pronounced in the measurements at 50 km h<sup>-1</sup>. At 30 km h<sup>-1</sup>, only a small part of the presumed lognormal distribution was detected.

With the studded tires on quartzite pavement at 70 km h<sup>-1</sup>, the particle number size distribution had a mean diameter of 44 nm with a geometric standard deviation of 1.7 and a number concentration of 18,000 cm<sup>-3</sup> (15–700 nm) at steady state (Fig. 1). A similar distribution profile was observed as the road simulator was run at 50 km h<sup>-1</sup>, but with a lower number concentration of 8000 particles cm<sup>-3</sup>. The size distribution from the 30 km h<sup>-1</sup> test is not shown in Fig. 1, but the particle size distribution was in the same range as the background level (~1000 cm<sup>-3</sup>) and no characteristic size distribution was observed. The same set of tires were run on granite pavement at 70 km h<sup>-1</sup> resulting in a total number concentration of 26,000 cm<sup>-3</sup>, a mean diameter of 50 nm and a geometric standard deviation of 1.8 at steady state.

### 3.2. Emission factors

The source strength for the particles in the size interval of interest (15–700 nm) can be estimated by continuously monitoring the particle size distribution and the total number concentration, from the point when the road simulator starts to the point when particle concentration reaches a steady state. The source strength can then be converted to a particle number emission factor for a LDV,  $E$  (particles vehicle<sup>-1</sup> km<sup>-1</sup>), a quantity that is more suitable for air dispersion modeling purposes. The particle concentrations are assumed to obey the following box model mass balance equation:

$$\frac{dN}{dt} = Q - kN(t), \quad (1)$$

where  $N(t)$  is the particle number concentration (particles cm<sup>-3</sup>) in the simulator hall (the box),  $Q$  is the source strength (particles cm<sup>-3</sup> s<sup>-1</sup>), and  $k$  is the loss rate constant (particles s<sup>-1</sup>). The loss rate is assumed to be first-order in particle number concentration and thus proportional to  $N(t)$ . Eq. (1) also assumes that the particles generated at the road–tire interface are efficiently mixed into the box, and that there is no ventilation in and out of the box (simulator hall) providing additional sources and sinks (ventilation was turned off during the experiments). If the particle concentrations obey Eq. (1), then  $N(t)$  has the following

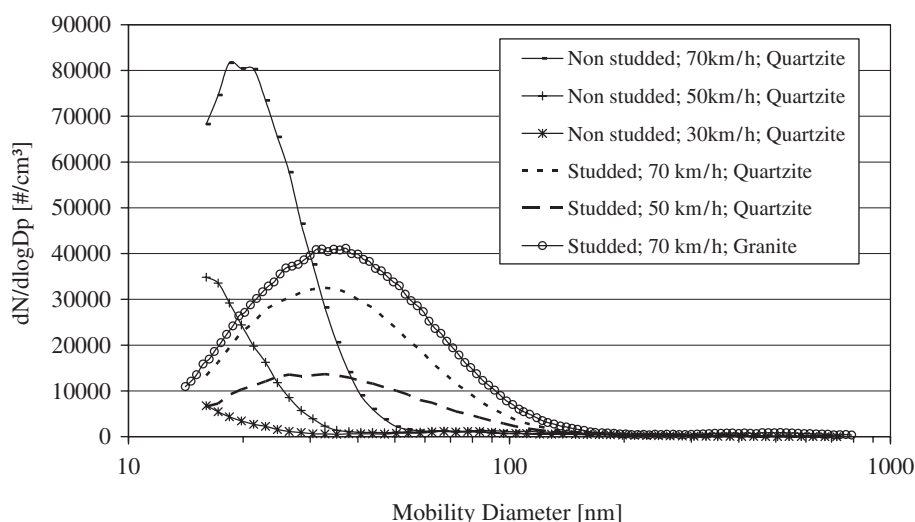


Fig. 1. Particle number size distributions of the aerosol generated at 30, 50 and 70 km h<sup>-1</sup> with non-studded tires on quartzite pavement, at 50 and 70 km h<sup>-1</sup> with the studded tires on quartzite pavement and at 70 km h<sup>-1</sup> with studded tires on granite pavement. The distributions are shown at steady-state concentrations.

time dependence:

$$N(t) = N_0 e^{-kt} + \frac{Q}{k} (1 - e^{-kt}). \quad (2)$$

Here,  $N_0 = N(t=0)$  is the initial background concentration at the time when the road simulator was turned on. In the experiments at 50 and 70 km h<sup>-1</sup>, the background concentrations were between 5 and 20% of the particle number concentrations produced by the road–tire interface at steady state (Fig. 2).

Both  $Q$  and  $k$  can be estimated by fitting Eq. (2) to the experimental particle number concentration data. Since the exact nature of the loss mechanisms is unknown, the loss rate ( $k$ ) was not interpreted. The important parameter ( $Q$ , in units of particles cm<sup>-3</sup> s<sup>-1</sup>) can nevertheless be determined and converted to particle number emission factors ( $E$ ) in appropriate units (particles km<sup>-1</sup>). This conversion from  $Q$  to  $E$  assumes that the four tires on the road simulator axles correspond to a single LDV. Furthermore, the speed of the tires over the road surface is known as well as the volume of the simulator hall (1500 m<sup>3</sup>).

Since the mixing time of the newly generated particles into the box (simulator hall) in reality is larger than zero, the calculated source strengths are likely to be upper estimates (in the observable size range > 15 nm). However, once the road simulator is turned on, conditions in the hall become very turbulent. When the road simulator runs at

70 km h<sup>-1</sup>, the air velocity is 4–6 m s<sup>-1</sup> at the sampling point in the square shaped hall, and the mixing of air is very efficient. The loss rate ( $k$ ) can be used to estimate a time constant as  $\tau = 1/k$  for the exponentially decreasing concentration of the airborne particles in the simulator hall. As expected, this time constant is shorter at a speed of 70 km h<sup>-1</sup> ( $\tau = 10$ –24 min) than at 50 km h<sup>-1</sup> ( $\tau = 25$ –45 min), since a higher speed produces more turbulence.

The derived particle number emission factors are shown in Table 1. For comparison, real-world exhaust particle emission factors from a fleet of 95% gasoline powered LDV, 5% diesel powered LDV with an average speed of 70 km h<sup>-1</sup> were estimated to be  $2.7 \pm 1.1 \times 10^{14}$  particles vehicle<sup>-1</sup> km<sup>-1</sup> by inverse modeling in a road tunnel in Stockholm, Sweden (Kristensson et al., 2004) and Ketzler et al. (2003) have estimated an emission factor of  $2.8 \pm 0.5 \times 10^{14}$  particles vehicle<sup>-1</sup> km<sup>-1</sup> for a mixed fleet of LDV and heavy duty vehicles (HDV) with an average speed between 40 and 50 km h<sup>-1</sup> in a street canyon in Copenhagen, Denmark.

The source strengths at 30 km h<sup>-1</sup> were too low for all tires and pavements to enable emission factors to be estimated. For the non studded tires, a considerable particle number fraction may be below the observable size range of the SMPS (i.e. < 15 nm). As seen in Fig. 1, more than 50% of the particle number can in fact be observed if the particles are lognormally distributed over particle

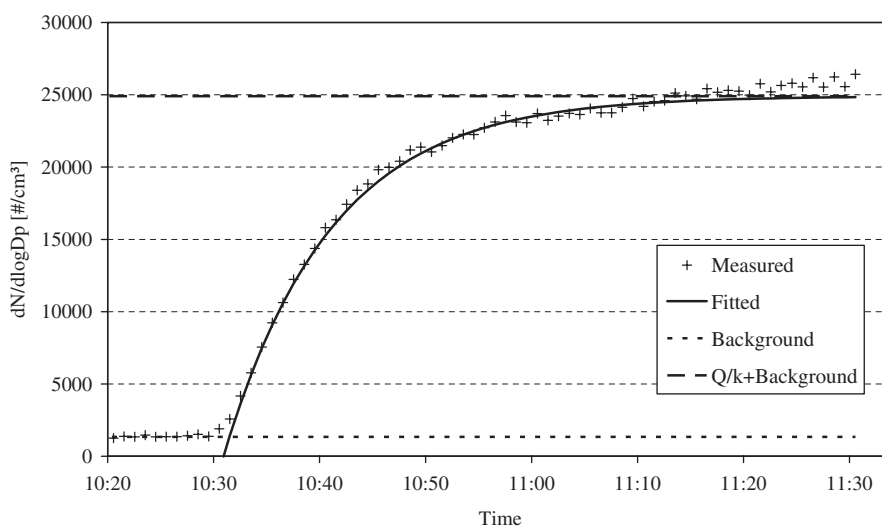


Fig. 2. Particle number concentration versus time and Eq. (2) fitted to the experimental data from the studded tire measurements on granite pavement at a speed of 70 km h<sup>-1</sup>.

Table 1

Emission factors for particles in the size interval 15–700 nm generated by the road–tire interface as observed in the VTI road simulator experiments

Tire	Road surface	Speed (km h <sup>-1</sup> )	Number of measurements	Emission factor (particles vehicle <sup>-1</sup> km <sup>-1</sup> )
Non-studded tires	Rubber	50	1	$3.7 \times 10^{11}$
Non-studded tires	Rubber	70	1	$1.1 \times 10^{12}$
Non-studded tires	Quartzite, ABS (stone mastic asphalt)	50	1	$3.8 \times 10^{11}$
Studded tires	Quartzite, ABS (stone mastic asphalt)	70	1	$1.9 \times 10^{12}$
Studded tires	Quartzite, ABS (stone mastic asphalt)	50	1	$6.1 \times 10^{11}$
Studded tires	Granite, ABT (asphalt concrete)	70	2	$3.1 \times 10^{12}$

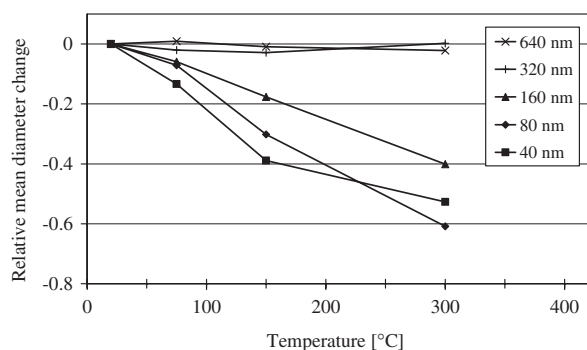


Fig. 3. Relative diameter changes of monodisperse wear particles at different TD temperatures.

diameters for speeds  $\geq 50$ –70 km h<sup>-1</sup>. The estimated emission factors for the non-studded tires are therefore at most 50% too low.

### 3.3. Thermodesorber measurements

The TD measurements were performed on-line, which means that the aerosol was characterized momentarily and not collected nor stored before the measurements. The aerosol generated in the hall with the studded tires mounted on the road simulator and quartzite pavement (combination 2) was characterized with the TD. The selected particles with original sizes of 40, 80 and 160 nm proved to be affected by the thermal conditioning, in the sense that the particle diameter decreased as the temperature rose, whereas the particle sizes 320 and 640 nm did not respond to the heating in the conditioner. Fig. 3 shows the relative particle diameter change for the different particle sizes at different TD temperatures. From this, it is evident that the 40, 80 and 160 nm particles behave

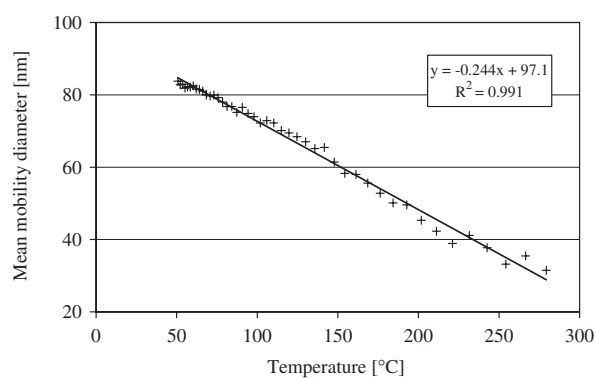


Fig. 4. Measured mean particle diameter of 80 nm wear particles versus TD temperature.

differently than the 320 and 640 nm particles. Fig. 4 shows the mean particle diameter of selected 80 nm particles after being conditioned at temperatures from 50 to 300 °C. The particle diameter appears to decrease linearly with increasing temperature. If the particle material had contained only one single substance then the response curve would have been more S-shaped. Hence, the particles most likely contain several semi-volatile components with a wide range of vapor pressures.

### 3.4. Microscopy

Fig. 5 shows examples of TEM images of wear particles from the road–tire interface, collected with an electrostatic precipitator after a DMA set at an equivalent electrical mobility diameter of 40 nm. The TEM analysis revealed essentially five major particle types:

- Type 1. Single near-spherical particles with a geometric diameter close to the selected DMA mobility diameter.

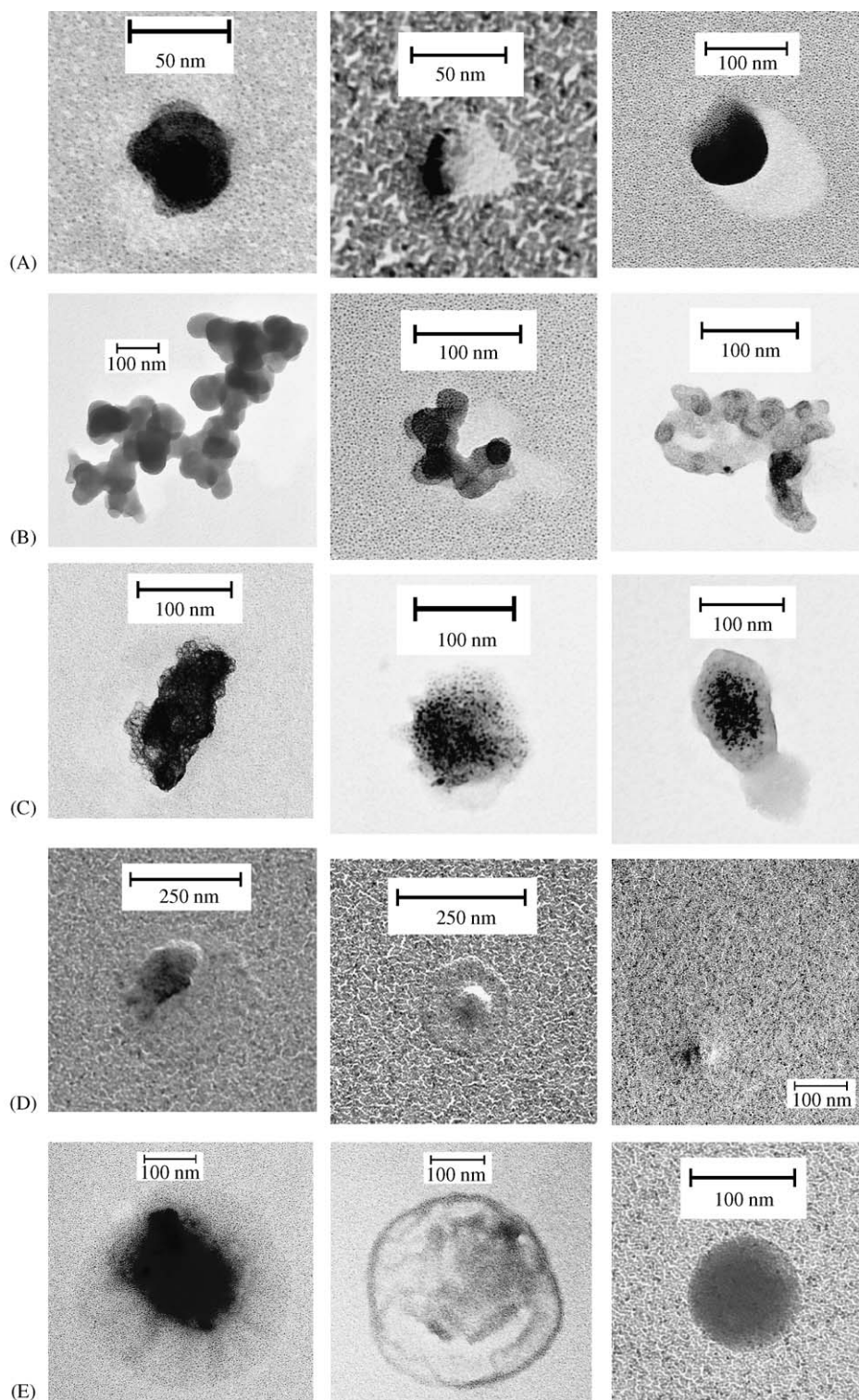


Fig. 5. Examples of particles generated by the road simulator and collected after a DMA set at 40 nm. The images were made with transmission electron microscopy (TEM). Row A: Type 1 particles. Row B: Type 2 particles. Row C: Type 3 particles. Row D: Type 4 particles. Row E: Type 5 particles.

- Type 2. Agglomerates of near-spherical particles with geometric diameters between 10–100 nm.
- Type 3. Particles that appear to have floated out on the substrate after collection, with a spotted appearance implying that they also contain considerably smaller particles.
- Type 4. Particles that appear to have floated out on the substrate after collection, containing inclusions of one or a few near-spherical particles each with a geometric diameter close to the selected DMA mobility diameter.
- Type 5. Particles that have floated out completely on the substrate after collection, not containing any observable inclusions.

Particles that appeared to be larger than the selected DMA mobility diameter can either be multiply charged or have fractal dimensions smaller than 3. Similar apparent discrepancies between selected and observed particle size were observed previously in TEM images (Park et al., 2003). The flat particles that had floated out on the substrate (particle types 3–5) were most likely liquid at the time of collection, since they left no Pt shadows.

Hypotheses regarding the nature of the observed particle types can be put forward, although no definite identification was possible. It appears likely that the near-spherical particles and their agglomerates originate from the carbon black reinforcing filler. Reinforcing fillers are essential components in all tires and are added to bind the polymer structure together to form a strong mesh. The most common filler material is carbon black (soot particles) and constitutes 30% by weight.

Another possibility is that the particles originate from small inclusions of excess ZnO or ZnS. Zinc oxide is an activator for organic accelerators that are used to speed up the vulcanization process. Typically, zinc oxide is added in concentrations that result in about 1% of Zn by weight in the final product. Zinc is mainly present in tires as excess ZnO and ZnS, but can also be found as organic zinc compounds (Fauser, 1999). Sulfur is used as a vulcanizer in nearly all rubber products and is present in tires in concentrations of typically a few percent by weight. Sulfur is therefore evenly dispersed in the rubber elastomer. Some fractions of the filler compounds were obviously sufficiently loosely bound to the rubber elastomer to cause them to detach from the tire surface when subjected to tensile stress. The tire surface heats up during driving. Thermal treatment of agglomerates tends to

cause the chain structure to contract (Friedlander et al., 2001). Since rather fractal-like agglomerates were observed, it seems that not all agglomerates were subjected to excessive heating during the release process. A further phenomenon discussed in Friedlander et al. (2001) is the curling up of the long-chain agglomerates, as they detach at one end after having been mechanically stretched. This would also produce rather dense agglomerate structures, similar to those produced from heating.

The oils used as softening fillers are a possible explanation for the liquid material observed in particles of types 4 and 5. These filler compounds have low vapor pressures and rapidly condense when cooled, if first vaporized and emitted from the tire at the elevated temperatures experienced during driving. The condensing vapors also adsorb on the surface of existing particles to create particles of type 4. The presence of nanometer-sized nuclei functioning as sites for vapor condensation could not be ruled out for particles of type 5.

The type 3 particles are more difficult to explain. These floated out on the substrate and had a spotted appearance. The nature of these spots could not be determined. While they may be very small particles (<10 nm) generated by the road simulator, it cannot be entirely ruled out that they are formed in the Pt shadowing process. If the latter is the case, there must be some mechanism by which the Pt grains become more visible inside these particles compared to the surrounding substrate (see, for instance, the images in row C of Fig. 5).

#### 4. Discussion

As seen in Table 1, the single most important factor determining the particle number emission factors is speed. The emission factors at 50 km h<sup>-1</sup> showed great similarities (between 3.7 and 6.1 × 10<sup>11</sup> particles vehicle<sup>-1</sup> km<sup>-1</sup>) for all pavements (granite, quartzite, rubber) and tires. Unfortunately, no runs that could be used to estimate emission factors were made with non-studded tires on granite or quartzite pavements at 70 km h<sup>-1</sup>. Studded tires running at 70 km h<sup>-1</sup> on the granite pavement showed the highest emission factors of all those estimated. (3.1 × 10<sup>12</sup> particles vehicle<sup>-1</sup> km<sup>-1</sup>).

The size distributions provide clues to the origin of these particles. Fig. 1 shows the distributions at steady state for studded tires and non-studded tires on the quartzite pavement. For the studded tires,



the overall shape of the size distributions remains nearly identical between 50 and 70 km h<sup>-1</sup>, and only the number concentration increases with speed. In contrast to this, the geometric median diameter of the size distributions increases considerably with speed when running the non-studded tires on the same quartzite pavement. While not entirely conclusive, this indicates that the type of tire used has the largest influence on the particles that are produced, and thus also that the particles are likely to originate from tire wear and not the pavement (bitumen). Again, the single most important factor determining the total particle number emission factors is speed.

Speed determines the amount of mechanical stress in the tire material and thus the temperature in the tire. Increased temperature leads to increased emissions of loosely bound reinforcing filler material and evaporation of semi-volatile softening oils. The mixture of oils used as softening fillers in the tires obviously affects the size of the particles that are produced. For the non-studded tires, these oils apparently cause a considerable particle number fraction to fall below the smallest observable particle size of the SMPS system used (15 nm). It can be speculated that the properties of the oil mixture determine whether or not homogeneous nucleation of gaseous precursors can produce significant quantities of nanometer-sized particles. Since the temperature in the road simulator hall was not controlled, any possible effect of ambient temperature on the nucleation rate and the particle size distribution could not be observed. This is an indication that the smallest particles with diameters <200 nm, the size range where the vast majority of the generated particles were observed, originate from the tires and not the pavement and the particles ≥320 nm that resisted thermal treatment up to 300 °C in the TD are likely to consist mostly of carbon reinforcement filler mechanically generated mineral grains from the stone material in the pavement.

The estimated particle number emission factors originating from the road–tire interface were between 0.1–1% of those observed for the tail-pipe emissions in real-world emission studies at speeds between 50 and 70 km h<sup>-1</sup>. In dynamometer test bench studies on individual LDV, powered with new engine and fuel technology, much smaller particle number emission factors was observed than for a mixed car fleet under real-world dilution conditions. Emission factors as low as

$8 \times 10^{11}$  particles vehicle<sup>-1</sup> km<sup>-1</sup> (Ristovski et al., 2005) and  $1 \times 10^{12}$  particles vehicle<sup>-1</sup> km<sup>-1</sup> (Maricq et al., 1999) have been reported and these emission factors are similar in magnitude to those originating from the road–tire interface in this laboratory study. This could mean that even though ultraclean vehicles are produced in the future, the fleet of LDV will still emit significant quantities of fine particles into the atmosphere, in particular in densely populated urban areas. These particles will be emitted in a size range where the likelihood of deposition deep in the respiratory system (the alveolar region) is at a maximum (ICRP, 1994). Furthermore, since these ultrafine particles are insoluble in the lung fluid, they are not easily removed from the alveoli and may thus constitute a significant health problem. Replacement of carbon soot with other reinforcing fillers such as SiO<sub>2</sub> as has been suggested by tire manufacturers should not be undertaken in large-scale production unless the consequences have been examined.

## 5. Conclusions

A road simulator study, originally aimed at characterizing coarse wear particles and their toxic effects, also revealed a significant source of sub-micrometer fine particles originating from the road–tire interface. The mean particle number diameters were between 15–50 nm, similar to those found in LDV tail-pipe exhaust. The estimated emission factors in the size interval 15–700 nm varied between  $3.7 \times 10^{11}$  and  $3.1 \times 10^{12}$  particles vehicle<sup>-1</sup> km<sup>-1</sup> at speeds of 50 and 70 km h<sup>-1</sup>. These source strengths are between 0.1–1% of those observed for the tail-pipe emissions in real-world emission studies at similar speeds. The total number emission factors depended more on vehicle speed than the type of tire and pavement, with higher speeds producing more particles.

Transmission electron microscopy studies of the ultrafine wear particles revealed the presence of several types of particles. Both particles that originated from the carbon reinforcing filler material (soot agglomerates) and the softening filler (mineral oils) were identified. Thermal treatment with a thermodesorber further corroborated the presence of semi-volatile compounds (oils) on the emitted particles. The importance of these findings is that even though vehicles can be produced with zero tail-pipe emissions, traffic will still continue to

be a significant source of particles also in the fine and ultrafine size range.

### Acknowledgements

This work was supported by the Swedish National Road Administration (Vägverket).

### References

- Burtscher, H., Baltensperger, U., Buckowiecki, N., Cohn, P., Hüglin, C., Mohr, M., Matter, U., Nyeki, S., Schmatloch, V., Streit, N., Weingartner, E., 2001. Separation of volatile and non-volatile aerosol fractions by thermodesorption: instrumental development and applications. *Journal of Aerosol Science* 32, 427–442.
- Dahl, A., Pagels, J., 2003. A thermodesorber for online studies of combustion aerosol particles—influence of particle diameter, residence time and mass concentration. First International Symposium on Incomplete Combustion, University of Kuopio, Finland.
- Donaldson, K., Stone, V., Clouter, A., Renwick, L., MacNee, W., 2001. Ultrafine particles. *Occupational and Environmental Medicine* 58, 211.
- Ezzati, M., Lopez, A.D., Rodgers, A., Vander Hoorn, S., Murray, C.J.L., The Comparative Risk Assessment Collaborating Group, 2002. Selected major risk factors and global and regional burden of disease. *Lancet* 360, 1347–1360.
- Fausser, P., 1999. Particulate air pollution with emphasis on traffic generated aerosols, Ph.D. Thesis, Risø National Laboratory, Roskilde, Denmark, Risø-R-1053(EN), February 1999.
- Friedlander, S.K., Ogawa, K., Ullmann, M., 2001. Elasticity of nanoparticle chain aggregates: implications for polymer fillers and surface coatings. *Powder Technology* 118, 90–96.
- Gustafsson, M., Blomqvist, G., Dahl, A., Gudmundsson, A., Ljungman, A., Lindbom, J., Rudell, B., Swietlicki, E., 2005. Inhalable particles from the interaction between tire, road surface and friction material. VTI report 520, VTI, SE-581 95 Linköping (in Swedish with English abstract).
- Hoek, G., Brunekreef, B., Goldbohm, S., Fischer, P., van den Brandt, P.A., 2002. Association between mortality and indicators of traffic-related air pollution in The Netherlands: a cohort study. *Lancet* 360, 1203–1209.
- ICRP, 1994. International Commission on Radiological Protection, Human respiratory tract model for radiological protection. *Annals of the ICRP*. Publication 66, Elsevier Science Inc., Tarrytown, NY.
- Katsouyanni, K., Touloumi, G., Samoli, E., Gryparis, A., Le Tertre, A., Monopoli, Y., Rossi, G., Zmirou, D., Ballester, F., Boumghar, A., Anderson, H.R., Wojtyniak, B., Paldy, A., Braunstein, R., Pekkanen, J., Schindler, C., Schwartz, J., 2001. Confounding and effect modification in the short-term effects of ambient particles on total mortality: results from 29 European cities within the APHEA2 project. *Epidemiology* 12, 521–531.
- Ketzel, M., Wählin, P., Berkowicz, R., Palmgren, F., 2003. Particle and trace gas emission factors under urban driving conditions in Copenhagen based on street and roof-level observations. *Atmospheric Environment* 37, 2735–2749.
- Kristensson, A., Johansson, C., Westerholm, R., Swietlicki, E., Gidhagen, L., 2004. Real-world traffic emission factors of gases and particulate matter from measurements in Stockholm, Sweden. *Atmospheric Environment* 38, 657–673.
- Kupiainen, K., Tervahattu, H., Räisänen, M., 2002. Experimental studies about the impact of traction sand on urban road dust composition. *The Science of the Total Environment* 308, 175–184.
- Maricq, M.M., Podsiadlik, D.H., Chase, R.E., 1999. Examination of the size-resolved and transient nature of motor vehicle particle emissions. *Environmental Science and Technology* 33, 1618–1626.
- Oberdorster, G., Gelein, R.M., Ferin, J., Weiss, B., 1995. Association of particulate air-pollution and acute mortality—involvement of ultrafine particles. *Inhalation Toxicology* 7, 111–124.
- Orsini, D.A., Wiedensohler, A., Stratmann, F., Covert, D.S., 1999. A new volatility tandem differential mobility analyzer to measure the volatile sulfuric acid aerosol fraction. *Journal of Atmospheric and Oceanic Technology* 16, 760–772.
- Park, K., Cao, F., Kittelson, D.B., McMurry, P.H., 2003. Relationship between particle mass and mobility for diesel exhaust particles. *Environmental Science and Technology* 37, 577–583.
- Pekkanen, J., Peters, A., Hoek, G., Tiittanen, P., Brunekreef, B., de Hartog, J., Heinrich, J., Ibaldo-Mulli, A., Kreyling, W.G., Lanki, T., Timonen, K.L., Vanninen, E., 2002. Particulate air pollution and risk of ST-segment depression during repeated submaximal exercise tests among subjects with coronary heart disease: the Exposure and Risk Assessment for Fine and Ultrafine Particles in Ambient Air (ULTRA) study. *Circulation* 106, 933–938.
- Peters, A., Douglas, W., Muller, J.E., Mittleman, M.A., 2001. Increased particulate air pollution and the triggering of myocardial infarction. *Circulation* 103, 2810–2815.
- Pope, C.A., Burnett, R.T., Thun, M.J., Calle, E.E., Krewski, D., Ito, K., Thurston, G.D., 2002. Lung cancer, cardiopulmonary mortality, and long-term exposure to fine particulate air pollution. *Journal of the American Medical Association* 287, 1132–1141.
- Ristovski, Z.D., Jayaratne, E.R., Morawska, L., Ayoko, G.A., Li, M., 2005. Particle and carbon dioxide emissions from passenger vehicles operating on unleaded petrol and LPG fuel. *Science of the Total Environment* 345, 93–98.
- WHO, 2002. World Health Report 2002. World Health Organization, Geneva.





## Particle emissions from district heating units operating on three commonly used biofuels

A. Wierzbicka<sup>a,\*</sup>, L. Lillieblad<sup>b</sup>, J. Pagels<sup>a</sup>, M. Strand<sup>b</sup>, A. Gudmundsson<sup>a</sup>,  
A. Gharibi<sup>c</sup>, E. Swietlicki<sup>c</sup>, M. Sanati<sup>b</sup>, M. Bohgard<sup>a</sup>

<sup>a</sup>*Division of Aerosol Technology, Lund University, P.O. Box 118, SE-221 00 Lund, Sweden*

<sup>b</sup>*Bioenergy Technology, Växjö University, SE-351 95 Växjö, Sweden*

<sup>c</sup>*Division of Nuclear Physics, Department of Physics, Lund University, P.O. Box 118, SE-221 00 Lund, Sweden*

Received 16 February 2004; received in revised form 6 August 2004; accepted 2 September 2004

### Abstract

The aim of this study was to characterise particle emissions from district heating units operating on three commonly used biofuels: forest residues, pellets and sawdust. Boilers used in the three district heating units were of moving grate type, with the maximum thermal output between 1 and 1.5 MW. The measurements were done after multicyclones, the only particle removal devices installed, therefore the direct emissions to ambient air were characterised. Number and mass size distributions were determined. Elemental composition of the particles was determined by particle induced X-ray emissions analysis (PIXE) and thermal-optical analysis. Particles' morphology was assessed on the basis of transmission electron microscopy (TEM). Total number concentration of emitted particles with aerodynamic diameter smaller than 5 µm (PM<sub>5</sub>) at medium operation load ranged from 6.3 to 7.7 × 10<sup>7</sup> particles/cm<sub>n</sub><sup>3</sup>, with the slightly higher values from combustion of forest residues. PM<sub>5</sub> mass concentration at medium load from low pressure impactor measurements ranged between 51 and 120 mg/m<sub>n</sub><sup>3</sup>, with the highest values from unit operating on forest residues. Both PM<sub>5</sub> mass and total number concentrations were dominated by fine mode contributions i.e. particles with aerodynamic diameter smaller than 1 µm (PM<sub>1</sub>). Elements determined by PIXE (*Z* > 12) contributed to 21–34% of PM<sub>1</sub> mass, of which K, S, Cl and Ca contributed to 18–33% of PM<sub>1</sub> mass, and Zn, Mn, Fe, Cr, Pb and Cd to 1–3%. Emitted concentrations of heavy metals depended on type of the fuel and operating load. Particulate organic (OC) and elemental (EC) carbon contribution to PM<sub>1</sub> ranged from 1–19% and 0–56%, respectively. Particulate OC concentrations strongly depended on the operation load regardless the type of the fuel, while EC concentrations seemed to depend both on load and the type of the fuel. Considering the potential public health implications of the obtained results, further research is needed to carefully assess the impact of particle emissions from biofuels combustion on human health and environment.

© 2004 Elsevier Ltd. All rights reserved.

**Keywords:** Particle emissions; Biofuel; Combustion; District heating

### 1. Introduction

Increasing use of biofuels for energy generation purposes is of particular interest nowadays because they allow mitigation of green house gases, provide

\*Corresponding author. Tel.: +46 462224014; fax: +46 462224431.

E-mail address: [aneta.wierzbicka@design.lth.se](mailto:aneta.wierzbicka@design.lth.se) (A. Wierzbicka).

means of energy independence and may even offer new employment possibilities (Loo and Koppejan (Eds.), 2002). In European Union, according to the White Paper objectives (Commission of the EC, 1997), the share of renewable energy sources in energy production is to be doubled by year 2010. The potential of biofuels in the fulfilment of these objectives was estimated as very promising (Loo and Koppejan (Eds.), 2002). Sweden provides an interesting case for studying the effects of increased biofuels combustion as the share of biofuels and peat in total energy supply increased from 9% in 1970 to 16% (97 TWh) in 2001 (Swedish Energy Agency (Ed.), 2002). In Sweden biofuels are mostly used in industrial sector and district heating; with the combustion being the most frequently used conversion technology.

There is a growing concern about emissions from biofuels combustion. It has been proved that biofuel furnaces emit relatively high quantities of particulate matter in comparison to natural gas and light fuel oil furnaces (Nussbaumer, 2001). Majority of the emitted particulates is smaller than  $10\ \mu\text{m}$  with high contribution of fine ( $< 1\ \mu\text{m}$ ) particles (Nussbaumer, 2002). These fine particles tend to be the most troublesome; in ambient air they have been associated with adverse health effects (Dockery et al., 1993; Gold et al., 2000; Kunzli et al., 2000; Lighty et al., 2000) and are difficult to capture in the available particle removal technologies (Nussbaumer, 2002).

There is an ongoing debate if the regulatory particle mass concentration limits are the most suitable to reflect potential health implications. Several studies indicated a correlation between adverse health effect and increased ambient particulate concentrations, even when the particle mass concentration was below the applicable at the time air quality standards (Lighty et al., 2000). Among reported health effects in long term exposure to PM<sub>2.5</sub> (particulate matter with aerodynamic diameter smaller than  $2.5\ \mu\text{m}$ ) are cardiopulmonary disease, lung cancer and increased mortality (Pope III et al., 1995, 2002; Dockery et al., 1993). Epidemiological studies suggest that in order to assess potential health effects, different particle characteristics should be considered such as particle number concentration, morphology, and detailed chemical speciation (Braun-Fahrländer, 2001; Lighty et al., 2000).

This study focuses on district heating units utilising various biofuels in moving grate boilers, as those become increasingly popular and in future are likely to substitute the one-family house heaters. Size of moving grate furnaces used in district heating usually range from 1 to 10 MW. For those smaller than 6 MW, multi-cyclones are usually the only used abatement technique; this is a result of economic feasibility as well as conformance with the present emission limit requirements (for the small units:  $100\text{--}150\ \text{mg}/\text{m}^3$  total particle mass concentration). 6 MW boilers and bigger are

additionally equipped with the electrostatic precipitators in order to meet the emission limits requirements.

There have been several studies attempting to characterise particle emissions from biofuels combustion in moving grate furnaces. Obernberger et al. (2001) characterised several biofuels in a pilot scale unit 0.4 MW and a large scale plant 40 MW, both of a moving grate type. Characterisation of particle emissions was done on the basis of low pressure impactor measurements combined with SEM imaging, wet chemical and SEM–EDX analyses. Particle size distribution was found to be bimodal, with one peak in fine mode and one in coarse mode. Increasing coarse mode emissions were associated with the ash content in the fuel as well as increasing operational load of the unit. Johansson (2002) studied particle emissions in two moving grate units (1.75 and 2.5 MW) fired with pellets and wood briquettes. Particle characterisation was done with an electrical low pressure impactor (ELPI) and a low pressure impactor (DLPI) measurements combined with EDX and TOF-SIMS analysis. PM<sub>10</sub> mass concentration ranged from 51 to  $240\ \text{mg}/\text{m}^3$ , PM<sub>10</sub> number concentrations varied between  $0.5 \times 10^7$  and  $6.5 \times 10^7$  particles/ $\text{cm}^3$ , and dominant compounds found in the fine mode were  $\text{K}_2\text{SO}_4$  and KCl.

In one of our previous studies Pagels et al. (2003) characterised particles from combustion of moist forest residues in a 1 and a 6 MW moving grate boilers. Number size distributions were determined using aerodynamic particle sizer (APS) and scanning mobility particle sizer (SMPS), mass size distribution was measured with DLPI. Elemental characterisation was determined by PIXE and ion chromatography. The coarse mode particle concentration was found to increase by more than one order of magnitude when the load increased from 50% to 75%. The mean diameter of fine particles, total volume and mass decreased with the increasing load. The dominant elements, among those detected by PIXE ( $Z > 12$ ) in fine mode were K, S and Cl and in the coarse mode Ca, K and S. Dominant ions found in fine mode were  $\text{K}^+$ ,  $\text{SO}_4^{2-}$  and  $\text{CO}_3^{2-}$ . The fine mode particles were found to have hygroscopic growth factors of 1.65 at RH = 90%. Strand et al. (2002) investigated penetration of biomass combustion particles through electrostatic precipitator (ESP) and a flue gas condenser in a 6 MW forest residue fired, moving grate type boiler with similar methods. Both the ESP and flue gas condenser showed size dependant particle separation efficiency. ESP removed 96% of particle number concentration and 83% of mass concentration, whereas flue gas condenser did not alter the particle number concentration significantly but reduced the mass concentration by half. Lillieblad et al. (2004) studied boiler's operation load influence on the emissions of fine particles and PAHs from biomass combustion in two moving grate boilers of

thermal capacity around 1 MW each. Boilers were fired with pellets and dry wood. ELPI was used for number size distributions determination. The boiler load was found to have little influence on the fine particles mass concentration. The total particle number concentration increased with the increased boiler load, decreased particle size was observed at that time. PAHs emissions varied by almost three orders of magnitude between studied boilers i.e. ranged from 2.8 to 2520  $\mu\text{g}/\text{m}_n^3$ .

There is a need for detailed characterisation of particle emissions from commonly used biofuels to enable development of efficient particle emissions control measures. This is done with the overall goal to ensure that emissions from biofuels combustion do not affect human health and environment.

In this study, particle emissions from combustion of the three most commonly used biofuels in Swedish district heating i.e. forest residues, sawdust and pellets were characterised. The simultaneous use of aerodynamic particle sizer and scanning mobility particle sizer allowed measurements of the fine and coarse mode number size distributions in the real time. Mass size distribution was obtained from low pressure impactor measurements. Elemental characterisation was done with PIXE. On the basis of thermal—optical method particle organic and elemental carbon content was determined in fine particles, which gave a new insight into composition of biofuel combustion particles. Particles' morphology was assessed using transmission electron microscopy.

## 2. Materials and methods

### 2.1. Measurement sites

Measurements were carried out at three district heating units in southern Sweden, which were chosen due to similar boiler design i.e. they had similar maximum thermal capacity, all were of moving grate and originated from the same manufacturer, therefore this gave a good comparative edge for studying particle emissions from combustion of three different biofuels. Unit 1 of 1.5 MW maximum thermal capacity was fired with sawdust, unit 2 of 1.5 MW was fired with pellets, and unit 3 of 1 MW was fired with forest residues. All boilers were equipped with a multicyclone as the only particle abatement measure. The multicyclones were of similar design and produced by the same manufacturer. The measurements were done after the multicyclones, when the boilers operated at various loads. The fuel feeding rate, control parameter in all boilers, was used as an indirect load measure. Due to the fact that the measurements were carried out at commercial units the load variations were limited to real heat demands at the time.

The measurements at unit 1 were made for 3 days in March 2002, at unit 2 for three days in June 2002, and at unit 3 for two days in January 2002. Additionally, collection of particles for particulate organic and elemental carbon analysis and for TEM imaging was carried out after the multicyclones at unit 4 fired with forest residues (12 MW of maximum thermal capacity). Measurements were carried out during 2 days in February 2003. Inclusion of these results enabled presentation of complementary analysis characterising particles from forest residues combustion.

### 2.2. Fuel characteristics

Moisture and ash content were determined on the basis of fuel analysis.

Forest residues consist mainly of wood chips from felling waste and by-products from the timber processing in the forest. Bark content is relatively high in this fuel. Spruce and pine are the dominant species. Moisture content was about 45% (weight), ash content on the dry basis (d.b.) was about 2.2% (weight).

Pellets are processed biofuel produced mainly from sawdust and cutter shavings from sawmill industry. They are refined and relatively homogenous with very low moisture content (7% weight), shaped into cylindrical pellets about 8 mm in diameter and with maximal length being four times the diameter. Bark content in pellets is low, ash content (d.b.) about 0.5% (weight).

Sawdust is a by-product from the local sawmill industry, it contains also cutter shavings. Moisture content was about 10% weight. Bark is not present in this biofuel, ash content (d.b.) was about 0.3% weight.

### 2.3. Sampling process

The particle emissions were sampled isokinetically from the flue gas duct using a thin-walled probe. The schematic diagram of the used sampling set up is given in Fig. 1. The flue gas sample was diluted with particle free (below 100 particles/cm<sup>3</sup>) and dry air. A two stage, ejector type of dilution system was used. In the first stage of dilution the supplied air was pre-heated to about 110 °C to prevent condensation of volatile material on the sampled particles. The flue gas temperature in the stack was between 100 °C and 175 °C. In the second stage of dilution, air at temperature between 20 °C and 23 °C was supplied. CO<sub>2</sub> measurements were used for assessment of the dilution ratio. The obtained dilution ratio was about 1:150. The total flow through the sampling system, after the diluters, was 12 l/min. The flow after diluters was split into different instruments sustaining the isokinetic sampling.

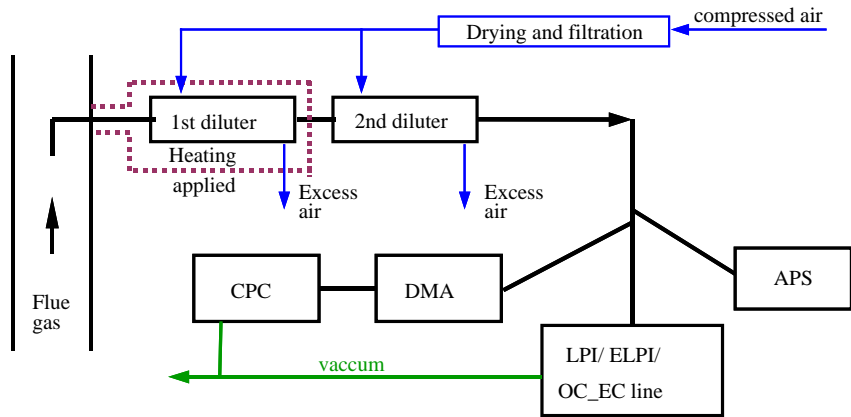


Fig. 1. Sampling set up.

#### 2.4. Particle losses

Penetration of particles through the whole sampling system (probes and diluters) was investigated experimentally. A method for penetration measurements similar to that described by Gudmundsson and Lidén (1998) was applied. A test aerosol of glass particles of  $2.45 \text{ g/cm}^3$  density were used. The penetration curve was modelled with Eq. (1) using the statistical software Origin, MicroCal Software Inc., USA. The software uses the Marquardt–Levensberg nonlinear least-squares curve fitting algorithm to estimate coefficients A, B and C. Fig. 2 presents the fitted penetration curve and experimentally measured points together with the error bars. Due to the fact, that particles with aerodynamic diameter bigger than  $5 \mu\text{m}$  had penetration lower than 0.5 in the sampling set up, only analysis of particles with aerodynamic diameter smaller than  $5 \mu\text{m}$  were considered in this study. Obtained penetration values for particles with aerodynamic diameters between 1.25 and  $5 \mu\text{m}$  were used for particle losses corrections.

$$P = A \cdot e^{-\ln(2) \left(\frac{d_{ae}}{d_{ae}^*}\right)^C}, \quad (1)$$

where  $P$  is the penetration;  $d_{ae}$  is aerodynamic particle diameter; and A, B and C are coefficients

#### 2.5. Instruments and analysis used

A scanning mobility particle sizer (SMPS 3934, TSI Inc., USA), consisting of a differential mobility analyser (DMA 3071) and condensation particle counter (CPC 3010), was used for measurements of the fine particle number size distribution (17–300 nm).

A time-of-flight instrument (APS 3320, TSI Inc., USA) was used for the determination of coarse particle number size distribution. Size range considered in this study due to particle losses in the sampling set up was

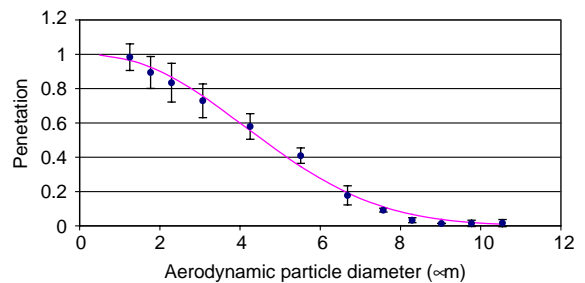


Fig. 2. Penetration through the whole sampling system (probes and diluters). Fitted penetration curve and experimentally measured points together with the error bars.

0.8– $5 \mu\text{m}$ . The instrument was used in the summing mode.

A 13-stage multi-jet low-pressure cascade impactor (DLPI, Dekati Ltd., Finland) in this study was used for determination of mass size distribution within 0.03 and  $5 \mu\text{m}$  size range. Aluminium foil collection substrates were used for gravimetric analysis. The sampled mass was determined by weighing the substrates before and after sampling. Polycarbonate substrates were used for particle induced X-ray emissions (PIXE) analysis. PIXE analysis was used for detection of elements with atomic numbers greater than 12. All substrates were coated with a low vacuum grease to prevent particle bouncing.

An electrical low-pressure impactor (Dekati ELPI) was used for number size distributions measurements at unit 1 and 2. Measured size range was similar to DLPI. The results obtained from this instrument were published in a separate article (Lillieblad et al., 2004).

In stack filter (Thimble in stack) was used for total mass concentration measurements. The probe was inserted in the duct and the flue gas was sampled isokinetically. The dust was collected on filters or in

thimbles and gravimetrically determined. The measurement time was around 1 h.

For particulate organic (OC) and elemental (EC) carbon analysis quartz filters were used. Prior to the sampling the quartz filters were pre-heated for three hours in 800 °C in order to remove organic impurities. The sampling line for particulate OC and EC analysis (Fig. 3) was split into two parallel lines after a pre-cyclone with a cut off diameter of about 1 µm, hence achieving collection of fine mode particles. In one sampling train a quartz filter (Q) was placed and in the other Teflon (T) followed by quartz backup filter (Q<sub>BCK</sub>). This enabled capturing of the particles on Teflon filter (T) while analysis of the downstream backup quartz filter (Q<sub>BCK</sub>) allowed estimation of the amount of gas phase organic vapours adsorbed onto quartz filter (positive artefact) (Turpin et al., 2000). A thermal-optical method, using a carbon analyser system developed by Sunset Laboratory Inc., was used for organic and elemental carbon analysis (Johnson et al., 1981; Turpin et al., 2000; Viidanoja et al., 2002).

Transmission electron microscopy (TEM) was used to study the morphology of fine particles. The particles were collected, with specifically designed electrostatic precipitator, directly onto electron microscopy copper grids, covered with a thin carbon substrate. The precipitator was placed between a DMA and a CPC enabling sampling of already charged particles of known

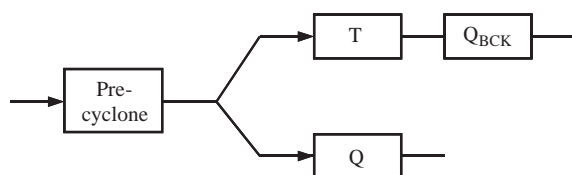


Fig. 3. Particulate organic and elemental carbon sampling line. After a pre-cyclone, with a cut off diameter of around 1 µm, the sampling train was split into two parallel lines. In one a quartz filter (Q) was placed and in the other Teflon (T) followed by quartz backup filter (Q<sub>BCK</sub>).

size, as well as control over the number of particles collected in the device. Artificial “shadows” were imposed on the collected particles before examination in the electron microscope in order to improve the contrast between small and almost electron transparent particles and the substrate. This was achieved in a vacuum chamber by firing a beam of metal atoms (Pt/Pd) onto the grids at an angle of 30°. Particle diameters could also be estimated, since the shadow remained even if the particles were volatile under the heating of electron beam during examination. Collection of particles for TEM imaging was carried out at unit 2 fired with pellets and unit 4 fired with forest residues. Samples were stored in an air-tight box filed with silica gel to reduce the relative humidity and therefore prevent humidity enforced reshaping of agglomerates.

### 3. Results and discussion

All concentrations are given as for dry gas, 13% CO<sub>2</sub>, at normal temperature (0 °C) and pressure 101.3 kPa.

#### 3.1. Number concentrations

Total number concentrations, for the three units operating at medium load, measured by SMPS and APS together with geometric mean diameters of fine particles are summarised in Table 1. Comparable number concentration for the particles with mobility equivalent diameter between 17 and 300 nm was observed for the three units with slightly higher values for unit 3 fired with forest residues. The opposite is observed for bigger particles measured with APS i.e. with aerodynamic particle diameter between 0.8 and 5 µm, where the highest number concentration is observed for unit 1 fired with sawdust and the lowest for unit 3 fired with forest residues. The total number concentrations for all the units are dominated by the fine mode, the fine mode number concentration is 4 orders of magnitude greater than the coarse mode number concentration.

Table 1

Total number concentrations measured with SMPS and APS and geometric mean diameters of fine mode. The arithmetic standard deviations of the measured values are given in brackets

Biofuel	Unit 1	Unit 2	Unit 3
	Sawdust	Pellets	Forest residues
Total number concentrations 17 < d <sub>p</sub> < 300 nm (particles/cm <sup>3</sup> )	6.7 × 10 <sup>7</sup> (±0.7 × 10 <sup>7</sup> )	6.3 × 10 <sup>7</sup> (±0.3 × 10 <sup>7</sup> )	7.7 × 10 <sup>7</sup> (±0.6 × 10 <sup>7</sup> )
GMD number 17 < d <sub>p</sub> < 300 nm (nm)	69 (±4)	79 (±2)	96 (±3)
Total number concentration 0.8 < d <sub>ac</sub> < 5 µm (particles/cm <sup>3</sup> )	8430 (±330)	4390 (±210)	3260 (±120)



Fine mode number size distributions for the three units are presented in Fig. 4. The number size distributions for unit 1 and 2 are similar, but in case of unit 3 the peak is shifted towards bigger diameters. The greatest fine mode geometric mean diameter (96 nm) was observed at unit 3 fired with forest residues, and it is bigger in comparison to those observed in units 1 and 2 (69 and 79 nm, respectively).

Number size distributions for the particles with aerodynamic diameter between 0.8 and 5  $\mu\text{m}$  are presented in Fig. 5. Number size distributions within this size range are very similar for the three units, with the only difference being slightly higher values for unit 1 fired with sawdust in comparison to the other two.

Considering previous studies in this field (Pagels et al., 2003; Strand et al., 2002; Lillieblad et al., 2004; Johansson, 2002), the gap between 0.3 and 0.8  $\mu\text{m}$  not measured by SMPS or APS is not expected to change the overall picture of number size distributions or total number concentrations.

### 3.2. Mass concentrations

Mass size distribution measured by DLPI for the three units operating at medium load is presented in Fig. 6. A significant difference of the height of the fine

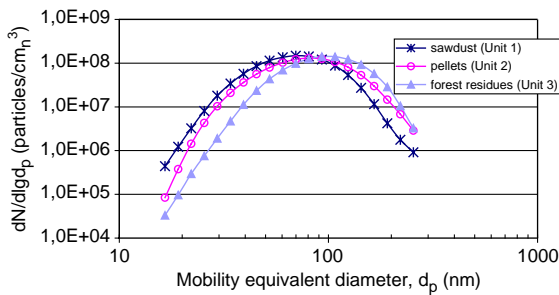


Fig. 4. Number size distributions measured with SMPS at medium operation load for the three units.

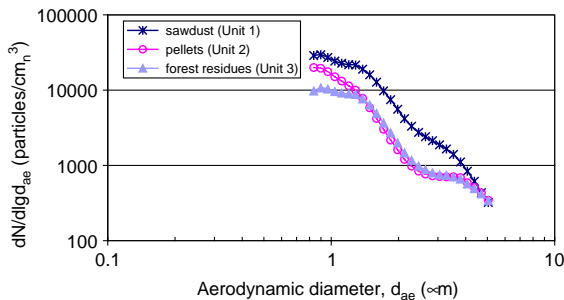


Fig. 5. Number size distribution measured APS at medium operation load for the three units.

mode peaks in mass size distribution between unit 3 fired with forest residues and the other two could be explained by the SMPS results. Higher total number concentration of fine mode accompanied with bigger geometric mean diameter, in case of unit 3 fired with forest residues, must yield much higher mass concentration in comparison to the other two.

The load variations at these commercial units were limited to real heat demands at the time. In Table 2 available DLPI and in stack filter results for the three units, presented in two other studies Lillieblad et al. (2004) and Pagels et al. (2003) are summarised. Results for unit 3 were obtained from measurements carried out in 2001, results for units 1 and 2 from the same measurement period as this study.

At medium load the greatest mass concentration (120  $\text{mg}/\text{m}_n^3$ ) for the particles with aerodynamic diameter smaller than 5  $\mu\text{m}$  (sum of PM1 and PM1-5) measured with DLPI was observed for unit 3 fired with forest residues. Obtained values are comparable with results reported in other studies. Concentration, measured with low pressure impactor, reported by Obernberger et al. (2001) for spruce and bark was within 35–105  $\text{mg}/\text{m}_n^3$  (dry gas, 13%  $\text{CO}_2$ ), in this study 41–117  $\text{mg}/\text{m}_n^3$ . Mass concentration, reported by Johansson at 1.75 MW boiler fired with pellets operating at medium load, was between 69 and 97  $\text{mg}/\text{m}_n^3$ , the lower value obtained in this study 51  $\text{mg}/\text{m}_n^3$  could be explained by considered size range in this study (only particles smaller than 5  $\mu\text{m}$  were taken into account). Total mass concentration (filter in stack) measurements, available for unit 1 and 3 at medium load, show slightly higher values maintaining the same trend i.e. greater mass concentration in case of unit 3 (153  $\text{mg}/\text{m}_n^3$ ) in comparison to unit 1 (101  $\text{mg}/\text{m}_n^3$ ).

The fine mode dominates the total mass concentration at medium load for the three units and at low load for units 1 and 3 (lack of data for unit 3 at low load). Differences between the biofuels become apparent at high load, an increase of coarse mode contribution (54%) to total mass is observed for unit 3 operating on forest residues. In unit 1 with increasing load a slight increase of coarse mode can be noticed accompanied by

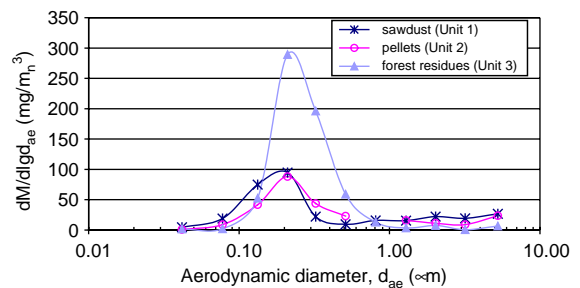


Fig. 6. Mass size distribution measured with DLPI at medium operation load for the three units.

Table 2  
Mass concentrations for the three units at different loads measured with DLPI and in stack filter

Biofuel	Load	Unit 1	Unit 2	Unit 3
		Sawdust	Pellets	Forest residues
		(mg/m <sup>3</sup> )	(mg/m <sup>3</sup> )	(mg/m <sup>3</sup> )
In stack filter measurements	Medium	101		153
Fine mode, PM1	Low	63	44	
Coarse mode, PM1-5, PM1/PM5		11 0.86	7 0.87	
Fine mode, PM1, Coarse mode, PM1-5, PM1/PM5	Medium	49 14 0.77	41 10 0.80	117 3 0.98
Fine mode, PM1, Coarse mode, PM1-5, PM1/PM5		High	44 20 0.69	

a slight decrease of fine mode contribution to total mass, but these are less pronounced than in case of unit 3 operating on forest residues. The results agree well with Hasler and Nussbaumer (1998) findings where only bark fuel showed 50% coarse mode contribution to the total mass and the total mass for other two fuels was dominated by fine mode.

### 3.3. Particulate organic and elemental carbon

Concentrations of particulate OC and EC for the three units operating at different loads together with their contribution to PM1 mass concentration (measured with DLPI) are summarised in Table 3. The correction of positive artefacts (adsorption of organic vapours onto quartz filter) was accomplished by subtraction of OC<sub>BCK</sub> organic carbon on the quartz backup filter (Q<sub>BCK</sub>, Fig. 3) from OC<sub>Q</sub> on the quartz filter (Q) placed in a parallel sampling train. Turpin et al. (2000) has shown that this method provides a good estimate of the adsorption of organic gas phase on a quartz filter. Measurements of positive OC artefacts were done at unit 2 and 4. It was estimated, on the basis of the backup to front loading ratio, that on average 78% of measured OC is due to organic gas phase adsorption on the quartz filter. This value is much higher in comparison to those reported in Turpin et al. (2000) where values between 10% and 55% are given for ambient air sampling. The difference could be due to much higher amounts of organic vapours in combustion process than in ambient air and due to heated dilution, which prevents partitioning to the particle phase. Organic vapours (OC<sub>BCK</sub>) measured in this study were between 5.6 and 12 mg/m<sup>3</sup> and are within the range of values measured by Launhardt et al. (2000) in flue gas

from domestic furnace fired with spruce, which were between 1.6 and 31 mg/m<sup>3</sup>. At times when measurements of artefacts were not performed this 78% estimation was subtracted from the measured OC<sub>Q</sub>. Uncertainty of the thermal-optical method for OC and EC analysis is about 8%, in case of used estimation about 20%.

It was observed (Fig. 7) that OC increases with increasing operation load regardless the type of the fuel. Contribution of OC to PM1 mass ranged from 1% to 19%. Contribution of OC to PM1 mass is significantly lower for unit 4 than for unit 1 at high load, again it could be explained by more stable and complete combustion in the bigger boiler at unit 4. Obtained values of particulate OC could have been underestimated due to heated primary dilution used, which likely minimises condensation of organic vapours into particle-phase normally occurring in the stack and atmosphere.

In Fig. 8, EC concentrations for the three biofuels at various loads are presented. EC concentrations varied to a great extent both with the type of fuel and operating load. Lower amounts of EC were observed during combustion of sawdust than pellets. In case of unit 1 fired with sawdust, EC decreased with increasing load and its contribution to PM1 mass concentration ranged from 0% to 8%. Much higher concentrations of EC with much greater variations were observed at unit 2 fired with pellets, its contribution to PM1 ranged from 18% to 56%, no clear dependence on the load was observed. Measurements of EC at unit 4 fired with forest residues were carried out only during high operation load, no elemental carbon was detected. Lack of EC could be explained by much better control of combustion parameters and therefore more stable and complete combustion in this significantly bigger unit.

Table 3

Concentrations of fine mode particulate organic (OC) and elemental carbon (EC) and their contribution to PM1 mass concentration (measured with DLPI). Positive artefacts of OC were corrected by subtraction of  $OC_{BCK}$  measured on the quartz backup filter ( $Q_{BCK}$ ) from  $OC_Q$  on the quartz filter (Q) in parallel sampling train. Total carbon (TC) contribution to PM1 is also given

Unit	Biofuel	Load	OC	EC	Mass conc. PM1 (DLPI)	OC/PM1	EC/PM1	TC/PM1
			( $mg/m_n^3$ )	( $mg/m_n^3$ )	( $mg/m_n^3$ )	%	%	%
1	Sawdust	Low	3.1 <sup>a</sup>	5.4	63	5	8	13
		Medium	3.9 <sup>a</sup>	0.9	49	8	2	10
		Medium	3.9 <sup>a</sup>	n.d.	49	8	0	8
		High	8.2 <sup>a</sup>	0.3	44	19	1	19
		High	5.5 <sup>a</sup>	n.d.	44	12	0	12
2	Pellets	Low	0.8	10.9	44	2	25	27
		Low	2.5	16.3	44	6	37	43
		Medium	5.8 <sup>a</sup>	7.3	41	14	18	32
		Medium	3.7 <sup>a</sup>	23.2	41	9	56	66
4	Forest residues	High	7.6	n.d.	92	8	0	8
		High	5.2	n.d.	92	6	0	6
		High	0.6	n.d.	92	1	0	1

<sup>a</sup>measurements of artefacts were not performed, estimation of 78%  $OC_Q$  was subtracted from the measured  $OC_Q$ . n.d.—not detected, method detection limit approximately  $2 \mu g m_n^{-3}$ .

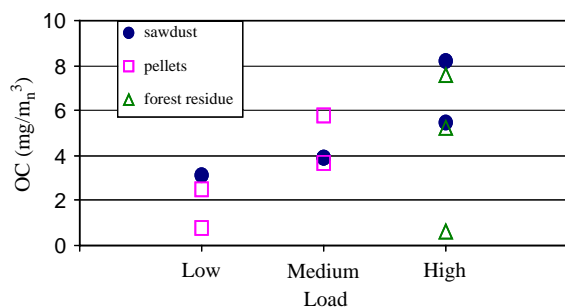


Fig. 7. Concentrations of OC at various loads for the three biofuels.

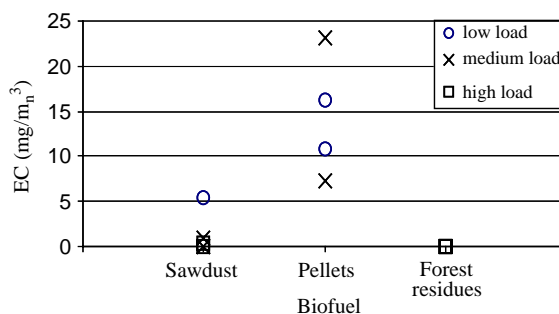


Fig. 8. Concentrations of EC for the three biofuels at various loads.

### 3.4. PIXE

Ten of the elements detected by PIXE ( $Z > 12$ ), namely (in descending contribution order): K, S, Cl, Ca, Zn, Mn, Fe, Cr, Pb and Cd contributed in average to 98% of PM5 mass quantified in the PIXE analysis.

Two distinct modes in the mass size distributions were observed. Main elements ( $Z > 12$ ) in the fine mode were K, S and Cl, and in the coarse mode Ca, K, and S. Similar particle elemental composition was observed in other elemental composition studies of biomass combustion particles (Pagels et al., 2003; Strand et al., 2002). Metals such as Zn, Cd, Pb and Cr were mostly found in the fine mode. This is the result of different particle

formation processes for the two modes (Lighty et al., 2000; Obernberger et al., 2001; Brunner et al., 2001).

Fine (PM1) and coarse mode (PM1-5) mass concentrations of four heavy metals that may have health and environmental implications, are given in Table 4 together with the PM1 contribution to PM5. From the table, it can be seen that the emitted amounts of these heavy metals are dependent on the type of the biofuel used. Biofuels with a high ash content (i.e. forest residues) tend to have high elemental concentrations, including heavy metals, in the emitted particles. Bark generally has a higher ash content than pure wood. Among studied biofuels the forest residues, with high bark content, give high emissions of Zn, Cr, Cd and Pb,



Table 4  
Mass concentrations of selected heavy metals, detected by PIXE, in fine and coarse mode and PM1 contribution to PM5

Unit	Type of fuel	Load	Zn			Cd			Pb			Cr		
			Fine mode, PM1		Coarse mode, PM1-5	Fine mode, PM1		Coarse mode, PM1-5	Fine mode, PM1		Coarse mode, PM1-5	Fine mode, PM1		Coarse mode, PM1-5
			$\mu\text{g}/\text{m}_n^3$	%	$\mu\text{g}/\text{m}_n^3$	%	$\mu\text{g}/\text{m}_n^3$	%	$\mu\text{g}/\text{m}_n^3$	%	$\mu\text{g}/\text{m}_n^3$	%	$\mu\text{g}/\text{m}_n^3$	%
1	Sawdust	Low	518	96	0	—	3	1	72	0	18	—		
		Medium	427	95	2	100	8	3	70	33	12	73		
		High	516	94	3	50	0	0	—	68	12	80		
2	Pellets	Low	806	90	201	83	15	4	80	117	53	69		
		Medium	2707	97	717	96	64	5	93	233	52	82		
		Medium	1587	99	120	98	55	1	99	586	5	99		

while pellets give the highest emissions of Zn and Cd. The lowest emissions of heavy metals come from the combustion of sawdust, which originates from the tree trunk wood and does not contain bark.

The metals were mostly found in the PM1 fraction. On average PM1 concentrations contributed to 91% of Zn detected in PM5, 85% of Cd, 83% of Pb and 81% of Cr, respectively. Particles in this size range can easily penetrate to the deepest parts of the human respiratory system. Therefore the emissions of these toxic elements from biofuel district heating units, apart from environmental impact, may pose a potential human health hazard.

In units 1 and 2 heavy metals concentrations in fine mode increased with the increasing operation load (exception Zn and Pb in Unit 1), while coarse mode concentrations (PM5) seem to remain at the same level despite the load changes.

Generally elements determined by PIXE ( $Z > 12$ ) contributed to 21–34 % of PM1 mass, of which K, S, Cl and Ca contributed to 18–33% of PM1 mass and Zn, Mn, Fe, Cr, Pb and Cd to 1–3 %.

### 3.5. TEM

In Fig. 9, typical TEM images of single particles from units 4 and 2 are presented, their sizes (as seen on images) are approximately 125, 300, 500 nm, respectively. It could be seen that particles of about 125 nm (Fig. 9a) are composed of two or three different parts, the darker the colour on the image the higher the electron density of material. The main part of the particle consists of highly electron-dense material with two attached parts composed either from less dense material or condensed vapours. The 250 nm particle (Fig. 9b) displays a more complex structure—an agglomerate in which several parts of different density are visible. Several individual particles, attached onto the larger particle, are clearly visible as well as a halo probably originating from evaporated vapours. The most complex agglomerate is visible in Fig. 9c. Fig. 9d shows an example of an elongated agglomerate collected from unit 2 fired with pellets. These latter two particles are composed of numerous smaller particles with individual diameters on the order of 20 nm. It is likely that these are soot agglomerates formed in zones with poor combustion conditions inside the boiler.

Rissler et al. (2003) showed that the particle mobility diameter decreases by around 10% when the particles are humidified to RH ~75%, indicating that the particles undergo a restructuring from agglomerates to more compact structures. In hygroscopic tandem differential mobility analyser measurements the exposure to high RH is on the order of seconds while TEM samples were stored for ~weeks (although in boxes with silica gel). Therefore, it cannot be ruled out that such

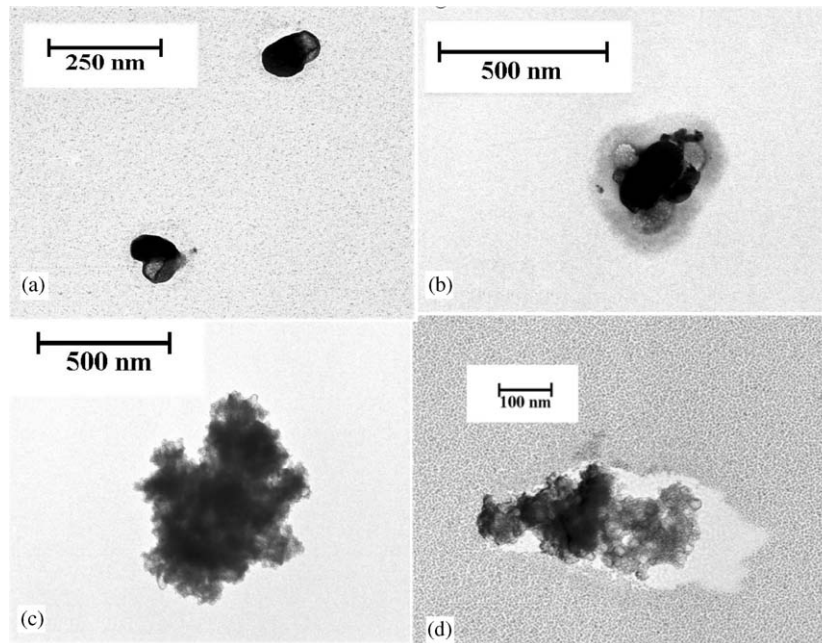


Fig. 9. Transmission electron micrographs of fine particles collected after the multicyclones emitted from unit 4 (a, b, c) and unit 2 (d).

humidity enforced restructuring did not take place, and the halo in Fig. 9b is a result of water-interaction.

It has to be also pointed out that the sizes seen on the images are not the absolute values. There are two processes taking place during TEM analysis, which may alter the size of the particle, i.e. dehydration of the specimen under high vacuum conditions and evaporation under electron beam (Mavrocordatos et al., 2002). Only a few minutes after the exposure the small particles (<100 nm) literally disappear, while bigger are most probably reduced to an inorganic residue.

In general the TEM images revealed that the most spherical particles are found in the size range around 100–150 nm, while larger particles tend to be more complex and in the form of irregularly shaped agglomerates. Similar trend was observed by Park et al. (2003) for diesel particles where with increasing size particles become more irregular and agglomerated. Although in case of diesel particles the simplest structures, comprising of few primary particles, were observed for particles about 50 nm while in this study simple structures were seen for particles about 100–150 nm.

#### 4. Conclusions

Total number concentration of particles, with aerodynamic diameters smaller than 5  $\mu\text{m}$ , emitted to the atmosphere at medium operation load ranged from 6.3 to  $7.7 \times 10^7$  particles/ $\text{cm}^3$ . PM5 mass concentration at

medium load from DLPI measurements ranged between 51 and 120  $\text{mg}/\text{m}^3$ . Higher values for both PM5 total number and mass concentrations were observed from combustion of forest residues. Both PM5 mass and total number concentrations were dominated by fine mode contributions. At high load operation, significant increase of coarse mode contribution to PM5 mass was observed only for unit operating on forest residues.

Particulate OC concentrations strongly depended on the operation load regardless the type of the fuel, while EC concentrations seemed to depend both on load and the type of the fuel. It has to be pointed out that the heated primary dilution could have decreased the condensation of the organics on the particles, which could normally occur during direct release to the atmosphere. It seems that for future studies dilution system with air at ambient temperature should be considered for particulate OC measurements.

Emitted concentrations of heavy metals depended on type of the fuel and operating load. Among studied biofuels forest residues gave high emissions of Zn, Cr, Cd and Pb, while pellets gave very high emissions of Zn and Cd. The lowest emissions of heavy metals came from the combustion of sawdust.

On the basis of PIXE and particulate OC and EC analysis it was possible to identify from 29% to 64% of PM1 mass, where PIXE analysis quantified between 21% and 34% of fine mode mass, particulate organic carbon 1–19%, elemental carbon 0–56%.

TEM images revealed that the most spherical particles were found in the size range around 100–150 nm, while larger particles tend to be more complex and in the form of irregularly shaped agglomerates.

Even though the studied district heating units meet the current mass concentration legal requirements, it has been shown that in all cases large amounts of fine particles containing heavy metals are being emitted. This might have potential public health implications as several studies indicated correlation between increased ambient fine particles concentration and adverse health effects such as cardiopulmonary disease, lung cancer and increased mortality. One has to bear in mind that this set of measurements, even though comparable to limited results published elsewhere, should not be treated as definitive. There is a need for further research to pinpoint general trends for particle emissions from biofuels combustion as a function of different type of boilers, fuels, operating conditions and efficiency of used abatement techniques. This should be done with the aim to carefully assess the impact of biofuels combustion on human health and environment, optimise the biofuel combustion technology, and provide more efficient fine particles removal devices.

### Acknowledgements

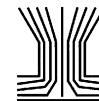
Financial support from Swedish National Energy Administration (STEM) and Swedish Research Council for Engineering Sciences (TFR) is gratefully acknowledged.

### References

- Braun-Fahrlander, C., 2001. Health effects of aerosols: what is the epidemiologic evidence? In: Nussbaumer, T. (Ed.), *Aerosols from Biomass Combustion*, International Seminar at 27 June 2001 in Zurich by IEA Bioenergy Task 32 and Swiss Federal Office of Energy, Verenum, Zurich, pp. 11–18.
- Brunner, T., Obernberger, I., Jöller, M., Arich, A., Pölt, P., 2001. Behaviour of ash forming compounds in biomass furnaces—measurement and analyses of aerosol formed during fixed-bed biomass combustion. In: Nussbaumer, T. (Ed.), *Aerosols from Biomass Combustion*, International Seminar at 27 June 2001 in Zurich by IEA Bioenergy Task 32 and Swiss Federal Office of Energy, Verenum, Zurich, pp. 75–80.
- Commission of the European Communities, 1997. *Energy For The Future: Renewable Sources Of Energy*, White Paper for a Community Strategy and Action Plan, COM(97)599 final (26/11/1997). European Commission (Ed.), Brussels.
- Dockery, D.W., Pope, C.A., Xu, X., Spengler, J.D., Ware, J.H., Fay, M.E., Ferris, B.G., Speizer, F.E., 1993. An association between air pollution and mortality in six US cities. *The New England Journal of Medicine* 329 (24), 1753–1759.
- Gold, D.R., Litonjua, A., Schwartz, J., Lovett, E., Larson, A., Nearing, B., Allen, G., Verrier, M., Cherry, R., Verrier, R., 2000. Ambient pollution and heart rate variability. *Circulation* 101, 1267–1273.
- Gudmundsson, A., Lidén, G., 1998. Determination of cyclone model variability using a time-of-flight instrument. *Aerosol Science and Technology* 28, 197.
- Hasler, P., Nussbaumer, T., 1998. Particle size distribution of the fly ash from biomass combustion. In: *Proceedings of the 10th European Conference and Technology Exhibition*, June 8–11, 1998, Murzburg, Germany, pp. 1330–1333.
- Johansson, L., 2002. *Characterisation of particle emissions from small-scale biomass combustion*. Licentiate Thesis, Chalmers University of Technology, Göteborg, Sweden.
- Johnson, R.L., Shah, J.J., Cary, R.A., Huntzicker, J.J., 1981. An automated thermal-optical method for the analysis of carbonaceous aerosol. In: Macias, E.S., Hopke, P.K. (Eds.), *In Atmospheric Aerosol: Source/Air Quality Relationships*, vol. ACS Symposium, Series No. 167. American Chemical Society, Washington, DC, pp. 223–233.
- Kunzli, N., Kaiser, R., Medina, S., Studnicka, M., Chanel, O., Filiger, P., Herry, M., Horak, F., Puybonniex-Texier, V., Quenel, P., Schneider, J., Seethaler, R., Vergnaud, J., Sommer, H., 2000. Public-health impact of outdoor and traffic-related air pollution: a European assessment. *The Lancet* 356, 795–801.
- Launhardt, T., Thoma, H., 2000. Investigation on organic pollutants from domestic heating system using various biofuels. *Chemosphere* 40, 1149–1157.
- Lighty, J.S., Veranth, J.M., Sarofim, A.F., 2000. Combustion aerosols: factors governing their size and composition and implications to human health. *Journal of the Air and Waste Management Association* 50, 1565–1618.
- Lillieblad, L., Szpila, A., Strand, M., Pagels, J., Rupar-Gadd, K., Gudmundsson, A., Swietlicki, E., Bohgard, M., Sanati, M., 2004. Boiler operation influence on the emission of submicron particles and PAHs from biomass fired grate boilers. *Energy and Fuels* 18, 410–417.
- Loo, S., Koppejan, J. (Eds.), 2002. *Handbook of Biomass Combustion and Co-Firing*. Prepared by Task 32 of the Implementing Agreement on Bioenergy Under the Auspices of the International Energy Agency. Twente University Press, Enschede, The Netherlands.
- Mavrocordatos, D., Kaegi, R., Schmatloch, V., 2002. Fractal analysis of wood combustion aggregates by contact mode atomic force microscopy. *Atmospheric Environment* 36, 5653–5660.
- Nussbaumer, T. (Ed.), 2001. *Aerosols from biomass combustion*. International Seminar at 27 June 2001 in Zurich by IEA Bioenergy Task 32 and Swiss Federal Office of Energy, Verenum, Zurich.
- Nussbaumer, T., 2002. *Aerosols from biomass combustion—overview on activities in IEA Bioenergy Task 32*. In: *Proceedings of the 12th European Biomass Conference 2002, Biomass for Energy, Industry and Climate Protection*, Amsterdam, The Netherlands, vol. 2, pp. 917–921.
- Obernberger, I., Brunner, T., Joller, M., 2001. Characterisation and formation of aerosols and fly-ashes from fixed-bed biomass combustion. In: Nussbaumer, T. (Ed.), *Aerosols from biomass combustion*. International Seminar at 27 June

- 2001 in Zurich by IEA Bioenergy Task 32 and Swiss Federal Office of Energy, Verenum, Zurich, pp. 69–74.
- Pagels, J., Strand, M., Lillieblad, L., Gudmundsson, A., Szpila, A., Bohgard, M., Swietlicki, E., Sanati, M., 2003. Characteristics of aerosol particles formed during grate combustion of moist forest residue. *Journal of Aerosol Science* 34, 1043–1059.
- Park, K., Cao, F., Kittelson, D.B., McMurry, P.H., 2003. Relationship between particle mass and mobility for diesel exhaust particles. *Environmental Science and Technology* 37 (3), 577–583.
- Pope, C.A. III, Thun, M.J., Namboodiri, M.M., 1995. Particulate air pollution as a predictor of mortality in prospective study of US adults. *American Journal of Respiratory and Critical Care Medicine* 151, 669–674.
- Pope, C.A. III, Burnett, R.T., Thun, M.J., Calle, E.E., Krewski, D., Ito, K., Thurston, G.D., 2002. Lung cancer, cardiopulmonary mortality, and long-term exposure to fine particulate air pollution. *JAMA* 287 (9), 1132–1141.
- Rissler, J., Szpila, A., Lillieblad, L., Strand, M., Pagels, J., Swietlicki, E., Bohgard, M., Sanati, M., 2003. Hygroscopic behaviour of flue gas particles emitted from a 1.5 MW biomass fired grate boiler. *Proceedings of European Aerosol Conference 2003*, Faculty of Medicine, Universidad Complutense de Madrid, Spain.
- Strand, M., Pagels, J., Szpila, A., Gudmundsson, A., Swietlicki, E., Bohgard, M., Sanati, M., 2002. Fly ash penetration through electrostatic precipitator and flue gas condenser in a 6 MW biomass fired boiler. *Energy and Fuels* 16, 1499–1506. Swedish Energy Agency (Ed.), 2002. *Energy in Sweden 2002*, ET20:2002, Multitryck, [www.stem.se](http://www.stem.se).
- Turpin, B.J., Saxena, P., Andrews, E., 2000. Measuring and simulating particulate organics in the atmosphere: problems and prospects. *Atmospheric Environment* 34, 2983–3013.
- Viidanoja, J., Sillanpää, M., Laakia, J., Kerminen, V., Hillamo, R., Aarnio, P., Koskentalo, T., 2002. Organic and black carbon in PM<sub>2.5</sub> and PM<sub>10</sub>: 1 year of data from an urban site in Helsinki, Finland. *Atmospheric Environment* 36, 3183–3193.

V



## Laboratory and Field Test of a Sampling Method for Characterization of Combustion Aerosols at High Temperatures

M. Strand,<sup>1</sup> M. Bohgard,<sup>2</sup> E. Swietlicki,<sup>3</sup> A. Gharibi,<sup>3</sup> and M. Sanati<sup>1</sup>

<sup>1</sup>*Division of Bioenergy, Växjö University, Växjö, Sweden*

<sup>2</sup>*Division of Ergonomics and Aerosol Technology, Lund University, Lund, Sweden*

<sup>3</sup>*Division of Nuclear Physics, Lund University, Lund, Sweden*

---

The objective of this study was to design and experimentally examine a sampling method for high-temperature aerosols from biomass combustion, in which nucleation and condensation from fly ash forming vapors is controlled. The sampling method includes a high-temperature probe in which the hot gas is diluted and then cooled. Laboratory results from sampling a model aerosol with known concentrations of SiO<sub>2</sub> particles and KCl vapor showed that when using a high dilution ratio, the KCl vapor was effectively separated from the aerosol by deposition onto the probe walls. When a lower dilution ratio was used, the KCl vapor generated a distinct nucleation mode when cooled in the probe. The sampling method was also used for sampling flue gas from a circulating fluidized bed boiler fired with forest residues. The results suggest that the major fractions of Ca, K, S, and Zn were present as particles at 780°C, whereas most of the Cl and Pb were present as gases. The field results are consistent with results previously reported and indicate that the method can be used for efficient and precise characterization of high-temperature combustion aerosols containing inorganic vapors.

---

### INTRODUCTION

Combustion of biomass for heat and power production in medium-scale-to-large-scale units is today a well-established and growing activity in several regions of the world. Potential solid biomass fuels, such as wood and various agricultural by-products, usually contain a substantial fraction of ash-forming inorganic compounds that might be detrimental to process and plant, causing operational problems such as corrosion and blockage (Miles et al. 1996; Baxter et al. 1998; Michelsen et al. 1998).

Some of the material will be transported through the boiler, subsequently being released as particulate emissions to the ambient atmosphere. The submicron fraction of the particulate emissions from combustion processes have a long residence time in the atmosphere and might be associated with adverse health effects due to their penetration and deposition in the lower respiratory tract, and their enrichment of potentially toxic components (Lighty et al. 2000).

Large-scale combustion of wood has been shown to produce a fly-ash mass size distribution with two distinct modes. (Hasler and Nussbaumer 1998; Valmari et al. 1998; Obernberger et al. 2001; Strand et al. 2002; Pagels et al. 2003). The particles in the two modes have different chemical compositions due to separate mechanisms of formation. The fine-mode particles in the submicron size range (<1 μm) are formed mainly from constituents that are vaporized during combustion of the fuel, e.g., K, S, Cl, and heavy metals. The vaporized components are subject to homogenous chemical reaction and might form vapors with low saturation vapor pressure, leading to gas-to-particle conversion at high temperatures. During combustion of straw, the main constituents of the submicron particle fraction were potassium sulphate and chloride (Christensen et al. 1998). A theoretical analysis indicated that the gas-to-particle conversion occurs during the cooling of the flue gas by homogeneous nucleation of K<sub>2</sub>SO<sub>4</sub> particles, which act as condensation nuclei for the subsequent condensation of KCl. The supermicron particles (>1 μm) are formed mainly from ash particles entrained from the fuel bed, and they consequently have a higher concentration of refractory ash components such as Ca, P, and Mn.

Pulverized coal combustion generally generates a fine-particle mode around 0.1 μm. Coal contains only low concentrations of volatile alkali compounds, but in the high temperature and reducing atmosphere surrounding the char particle the refractory oxides (e.g., Si, Al, Fe, and Mg) can undergo

---

Received 17 December 2003; accepted 27 May 2004.

Address correspondence to Michael Strand, Växjö University, IBP, Department of Bioenergy Technology, SE-351 95 Växjö, Sweden.  
E-mail: michael.strand@ibp.vxu.se

a reduction to more volatile suboxides or metal compounds that might vaporize (Flagan and Seinfeld 1988). It is not fully investigated if a fine-particle mode can be formed also during biomass combustion by reduction of refractory oxides close to the burning char. When firing bark in a moving-grate, 450 KW boiler, considerable amounts of Ca were found in the submicron mode (Obernberger et al. 2001). For other fuels the concentration of Ca was much lower. The authors assumed that a release of Ca to the vapor phase was not possible and that the Ca-containing submicron particles were released directly from the fuel.

In order to achieve a deeper understanding of the particle formation process in biomass combustion, it is desirable to have a method for characterization of combustion aerosols at high temperatures, where a fraction of the ash-forming material is still present as inorganic vapors. There are certain properties that must be considered when sampling and measuring aerosols of high concentration and high temperature, since a number of dynamic physicochemical processes are in progress in the aerosol system. If a sampling and cooling device is used, it must be designed to quench all aerosol dynamics and chemistry in order to obtain a representative measurement. Quenching will constitute a specific problem when the combustion aerosol contains inorganic vapors, e.g., alkali or heavy metal vapors. These vapors generally have a negligible vapor pressure at the temperature prevailing at the probe outlet. Consequently, they will condense as the gas temperature is decreased in the probe, which might affect the original particle phase. The condensing vapors might contribute to the particle phase by deposition on the surface of the original particles and by forming a nucleation mode. In both cases, the use of the sampling device will alter the original size distribution and particle composition.

Recently there has been increasing interest in dilution effects from internal combustion engines, especially diesel engines (Kittelson 1998). When sampling the exhaust aerosols, temperature, concentration, and humidity must generally be decreased upstream from the instruments. When diluted, condensing species, e.g., volatile organic and sulphuric compounds, might form high number concentrations of ultrafine particles. The present interest in the dilution effects is not only a matter of conserving the particle concentration in the hot exhaust gas but also of simulating the aerosol dynamics at the tailpipe outlet. In one study, a two-stage diluter was used when sampling the exhaust from a diesel engine (Kittelson and Abdul-Khalek 1999). The primary diluter was designed to produce high saturation ratios by diluting with cool gas. The second diluter was used in order to quench the aerosol dynamics. The results showed that the formation of ultrafine particles depended on dilution ratio and temperature as well as concentration of particles and particle precursors.

Diffusion denuders have been used frequently in order to separate condensable gas components prior to the cooling of the aerosol (Willeke et al. 1993). Traditionally designed diffusion denuders are not suitable for high-temperature (>600°C)

biomass combustion applications, since the temperature as well as the complexity of the gaseous components makes it difficult to design appropriate adsorption coatings.

There have been a few attempts to characterize high-temperature aerosols from biomass combustion. Valmari et al. (1998) studied fly-ash particles formation and fly-ash deposition during fluidized bed (CFB) combustion of willow at 650°C. The mass size distribution was measured using an in-duct, 11-stage, multijet, Berner-type, low-pressure impactor. The author's interpretation of the results was that the mass size distribution included inaccuracies since the collection substrates gained mass due to reactions with components of the hot flue gas.

In another study of ash behavior during CFB combustion of biomass, Valami et al. (1999a) investigated the gas- and particle-phase concentration of ash-forming compounds at 800–850°C. The particles were collected in an in-duct sampling system consisting of a precyclone and a quartz filter. After the quartz filter, the flue gas sample was quenched with cool air using a porous tube in order to minimize sampling losses. During quenching, the vapors formed fine particles that were collected on a polycarbonate filter. The elemental composition of the gas phase was determined by analyzing the particles collected on the second filter. The deposited particles were composed mainly of K and Cl. Sulphur was not found in significant amounts, indicating that the sulphur was present mainly as particles collected on the first filter or as gases (SO<sub>2</sub>) not condensed during quenching. According to the authors the vapor fraction might be underestimated because some of the vapors might have reacted with the first quartz filter and been erroneously counted as particles.

In order to understand the behavior of fly-ash-forming constituents at high temperatures, it is desirable to have a simple method of investigating how the fly-ash-forming compounds are distributed between vapor phase and particles phase, as well as between particles of different size fractions. The method should allow for efficient and reliable vapor-particle separation at positions close to the burning fuel, where the ratio of vapor to particle concentration is expected to be high. Moreover, the method should allow for transient measurements using on-line instruments, as enhanced variations in concentration and size distribution can be expected at positions of early particle formation.

The objective of this study was to investigate experimentally the possibility of using a high-temperature dilution-deposition probe in order to control the separation the fly-ash-forming vapors from flyash particles at high temperatures. The method was examined using a laboratory setup where a well-defined model aerosol was generated and sampled. The sampling technique was also tested in the field, characterizing particles and vapors at 780°C in a 104 MW CFB boiler fired with wood chips. The results show that using a high-temperature dilution probe is a feasible method for sampling aerosols in biomass-fired boilers, enabling online characterization at high temperatures.

## EXPERIMENTAL

### The High-Temperature Dilution Probe

The sampling probe consists of two coaxial quartz tubes (Figure 1). The length of the outer tube is 0.8 m, with an inner diameter (i.d.) of 28 mm. At the hot side of the outer tube, there is a contraction ending with a 25 mm long, 5 mm i.d. inlet tube. At the cold end of the 28 mm tube there is a contraction in order to seal the outer tube around the inner tube using a rubber ring sealing. At the cold end there is also a perpendicular 8 mm inlet tube for the dilution gas. The inner tube (i.d. 9 mm) is centered inside the outer tube by a sleeve. The inner tube can be slid axially, varying the width of the circular slit that is formed between the tip of the inner tube and the hot side contraction of the outer tube. During sampling the slit width was kept below 1 mm in order to accomplish proper mixing conditions in the mixing zone. The dilution air was fed through the perpendicular inlet and heated by tube walls as it was transported towards the dilution position at the hot end of the probe. In the dilution and mixing section the gas from the inlet tube was diluted with the heated dilution air. The diluted gas was then cooled to about 200°C by the walls before exiting the probe. The gas was further cooled to 25°C before being split between the instruments using a copper tube cooled in a water bath. Dried and filtered compressed air was used as dilution gas, and the flow rate was controlled using a calibrated mass flow controller

(Bronkhorst HI-TEC). The outlet flow to the instruments was 10 l/min.

In order to control the dilution ratio, the mass flow controller was first set to 11 l/min, which produced a net flow of dilution air out of the probe tip. By decreasing the rate of dilution air stepwise until the instruments started to indicate particles, the point of zero-flow through the inlet tube could be established. By further decreasing the flow rate of dilution air, the flow rate of undiluted gas through the inlet tube could be controlled, and the desired dilution ratio could be set. The procedure of establishing the zero-flow was necessary in order to produce high dilution ratios, since the flows through the mass flow controller and the instruments might vary slightly due to drift and changes in ambient pressure and temperature. Nevertheless, by initiating each measurement with establishing the zero-flow, a stable flow difference as low as 0.1 l/min could be produced, yielding a dilution ratio of 1:100 with an accuracy of 30%.

When sampling from the CFB boiler, an additional insulating jacket was used. The jacket could be slid along the probe in order to obtain an appropriate temperature profile in the probe, even when a large part of the probe was exposed to the hot flue gas.

### Particle Characterization

An electrical mobility spectrometer (SMPS; 3934, TSI Inc.) incorporating a condensation particle counter (CPC;

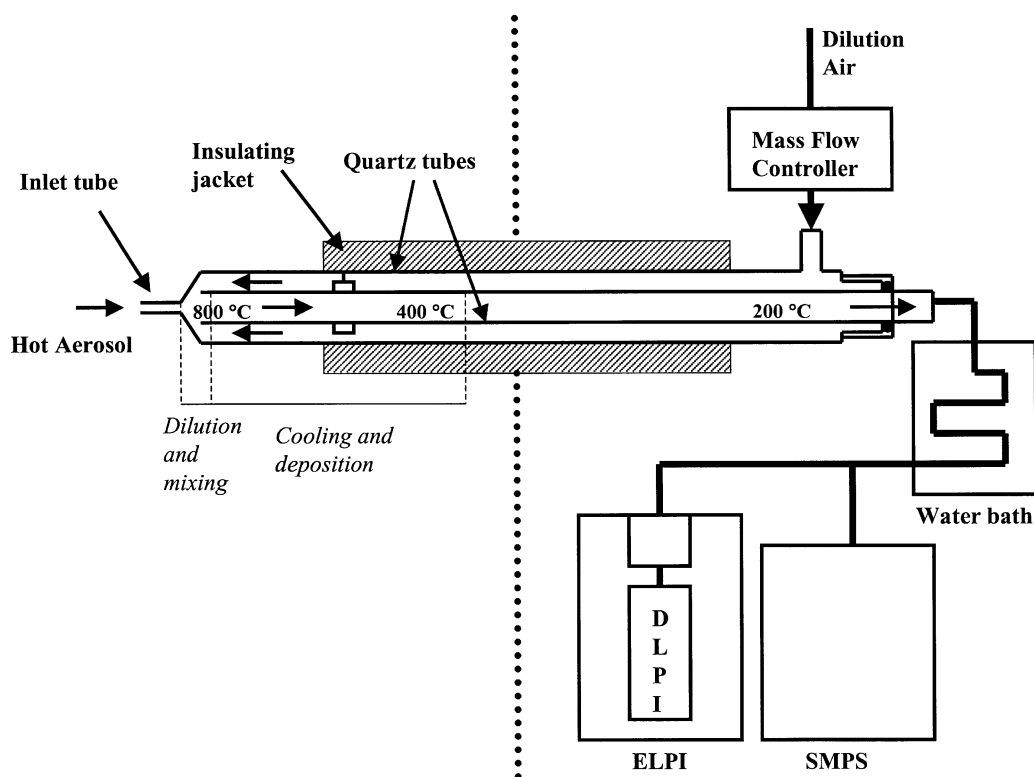


**Figure 1.** The sampling system used for high-temperature aerosol characterization. The aerosol was diluted and cooled inside the probe. Particle samples were collected using the DLPI, and the number size distributions were measured using the SMPS system.



model 3022, TSI Inc.) was used for determining the particle number size distribution. The size interval studied was in the range of 17–550 nm. In addition to the SMPS, an electric low-pressure impactor (ELPI; Dekati Ltd.) was used. The ELPI system used gives a size distribution in the 0.03–10  $\mu\text{m}$  range in 12 channels. Because of the low channel resolution in the 30–100 nm range, the ELPI was not suitable for accurately determining the size distribution of the nucleation mode. However, the ELPI has a high time resolution and a constant flow of about 10 l/min, and the ELPI instrument was therefore used for establishing the zero flow and the dilution ratio as well as for providing a constant flow through the dilution probe.

In order to obtain size-classified particle samples from the CFB boiler for elemental and gravimetric analysis, the internal ELPI Dekati low-pressure multijet cascade impactor (DLPI) was used. The DLPI classifies the aerosol particle into 13 size fractions ( $d_{50}$  0.03–10  $\mu\text{m}$ ). The sampling was carried out by first establishing the desired dilution ratio, operating the ELPI in the ordinary online sampling mode. Then the internal corona charger and the ion trap were turned off, allowing the ELPI to be used as an ordinary DLPI. The high-dilution samples and the low-dilution samples were collected subsequently within a period of 4 h. Only the first 7 stages of the impactor, corresponding to the submicron particle fraction, were analyzed. Greased polycarbonate foils were used as impactor substrates. Particle-induced X-ray emission analysis (PIXE) was used for elemental analysis of the impactor substrates. Approximately 30 elements were analyzed. Since PIXE is not suitable for elements with an atomic number less than 13, ash components such as Na and Mg were not analyzed.

### The Laboratory Setup

A model aerosol with  $\text{SiO}_2$  particles and KCl vapor was generated in the laboratory setup (Figure 2). The  $\text{SiO}_2$  particles were generated by decomposition of Hexamethyldisiloxane at 650°C in tubular furnace (reactor 1). The atomizer was used to generate a spray of KCl dissolved in water. The KCl solution droplets were mixed with the aerosol from reactor 1 before being

fed into the second tubular furnace reactor (reactor 2). In reactor 2 the KCl solution droplets were dried and then evaporated at 900°C. The aerosol with  $\text{SiO}_2$  particles and KCl vapor was sampled inside reactor 2 at a temperature of 900°C, using the high-temperature dilution probe. The dilution ratio in the probe was varied in order to investigate the dilution effect. Measurements were carried out when generating  $\text{SiO}_2$  particles or KCl vapor only, as well as when generating both particles and KCl vapor.

### The CFB Boiler Setup

The flue gas was sampled in a boiler fired with forest residues mixed with about 10% peat. The boiler is a circulating fluidized bed type with a thermal effect of 104 MW. The flue gas sample was extracted from the duct between the process cyclone and the super-heater at a temperature of about 780°C. The sample was taken perpendicular to the direction of the flue gas flow in order to avoid overloading and clogging by coarse fly-ash particles and bed material. Only the particle fraction  $<1 \mu\text{m}$  was studied. The inlet efficiency of the probe was estimated to be close to 1 for particles smaller than 0.5  $\mu\text{m}$ .

## RESULTS AND DISCUSSION

### Results from Laboratory Setup

The number size distributions obtained for different dilution ratios are given in Figure 3a. All size distributions given in all figures are corrected for dilution. When feeding  $\text{SiO}_2$  particles only, and using a dilution ratio of 1:10, the number size distribution was unimodal, with a geometric mean diameter (GMD) of 110 nm and a number concentration of  $4 \times 10^5$  particles/ $\text{cm}_n^3$  ( $1 \text{ cm}_n^3 = 1 \text{ cm}^3$  at 0°C, 1 atm). When adding 20  $\text{mg}/\text{m}_n^3$  of KCl vapor to the reactor, and using the same dilution ratio (1:10), a distinct nucleation mode around 30 nm was generated in addition to the original mode. As the dilution ratio was increased to 1:33 when feeding both  $\text{SiO}_2$  and KCl, the number concentration decreased slightly, and the modal diameter of the nucleation mode decreased to 15 nm. When using a dilution ratio

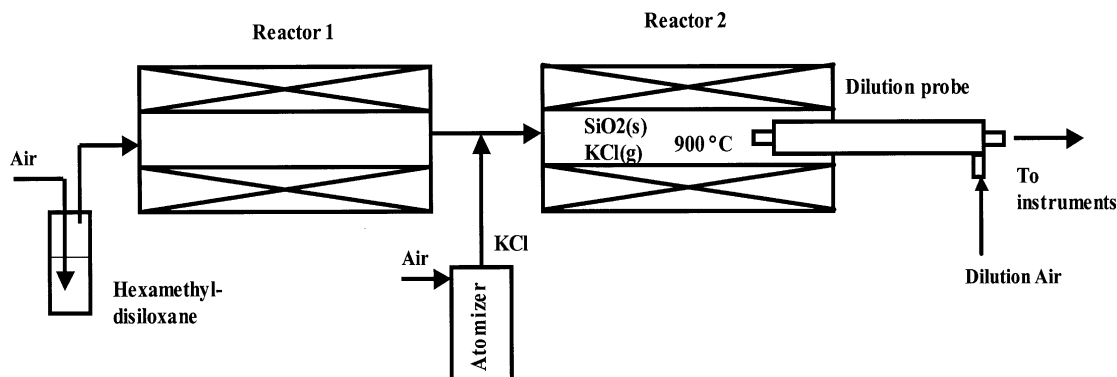


**Figure 2.** The model-aerosol-generating system.  $\text{SiO}_2$  particles were generated in the first reactor and KCl vapor was generated in the second reactor.

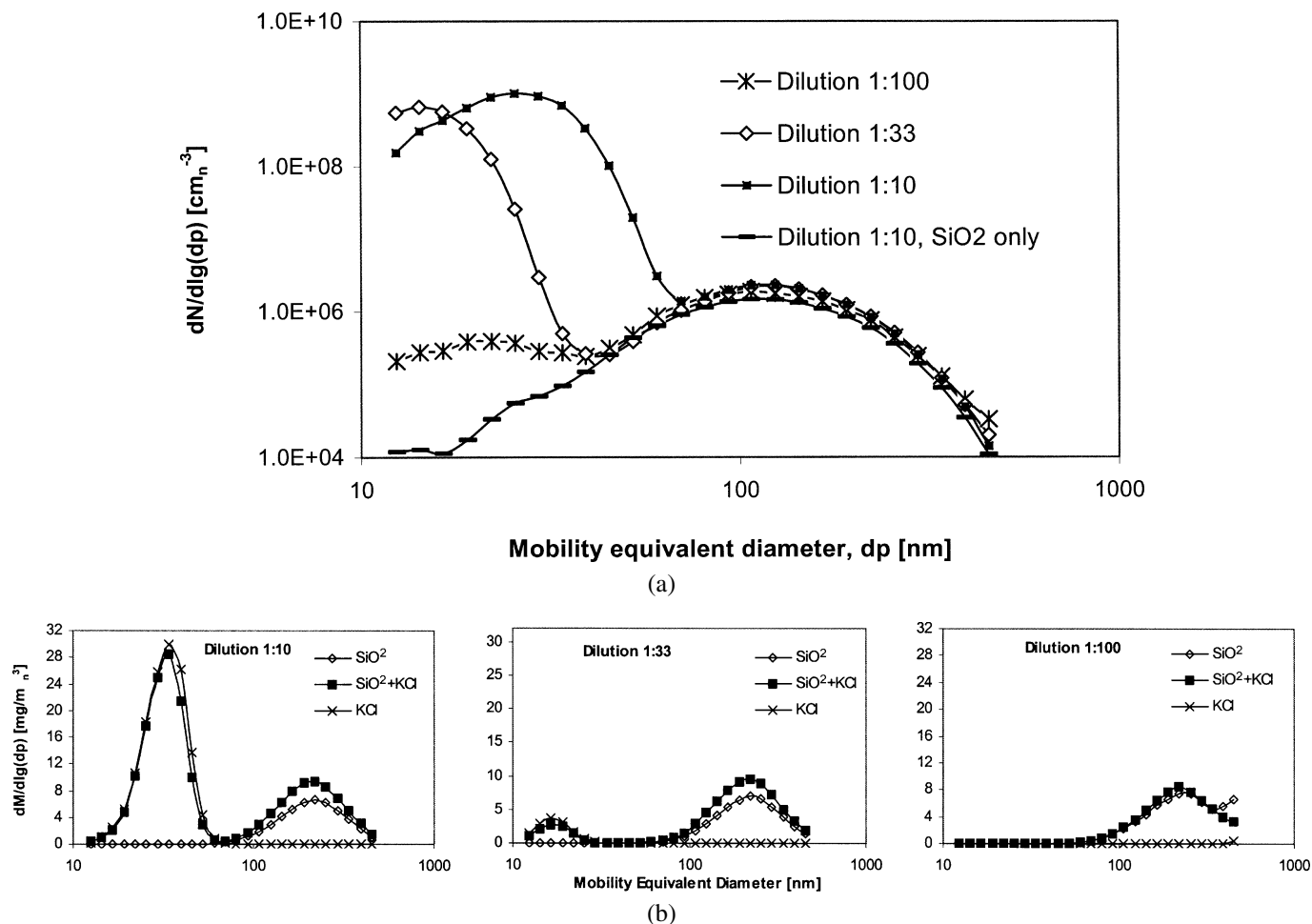


**Figure 3.** (a) Particle number size distribution of the laboratory generated aerosol, using different probe dilution ratios. (b) Particle mass size distribution of laboratory-generated aerosol, using different precursor compositions and dilution ratios.

of 1:100 the nucleation mode vanished almost completely. The size distribution above 70 nm was not affected by adding KCl or by using different dilution ratios. The mass size distributions calculated from the SMPS data are given in Figure 3b. An effective particle density of 2 g/cm<sup>3</sup> was assumed. When using the 1:10 dilution ratio and feeding KCl vapor only, a distinct nucleation mode around 35 nm was generated. When adding the SiO<sub>2</sub> particles, an additional mode around 220 nm was generated. When closing down the KCl feed, the nucleation mode disappeared, while the 220 nm mode decreased slightly. When repeating the same procedure, using a dilution ratio of 1:33, the KCl-induced nucleation mode decreased by a factor of 10. When increasing the dilution ratio to 1:100, the nucleation mode was further decreased by a factor of about 1000. These results indicate that raising the dilution ratio will effectively prevent KCl vapor from affecting the original SiO<sub>2</sub> particle distribution. The total mass of the SiO<sub>2</sub> mode decreased slightly when the KCl feed was closed, but the particle size did not increase. This indicates that no significant condensation on the existing particles occurred. The slight decrease in concentration is prob-

ably an effect of fewer losses in the reactor and in the sampling system when KCl vapor was present, e.g., by neutralization of the highly charged SiO<sub>2</sub> particles by ionized KCl in the hot reactor.

There are several possible mechanisms, which may explain the enhanced separation of KCl vapor at high dilution ratios, including:

1. Increased ratio of wall condensation to particle formation.
2. Formation of smaller KCl nuclei, which are exceedingly lost by deposition onto the probe walls and tubing, by means of diffusion.
3. A nucleation mode below 10 nm is formed, which is not detectable by the instruments used.

The separation effect might be a result from a combination of the listed mechanisms. The first mechanism allows for a more complete and controlled separation process, and therefore the subsequent discussion will be focused on this. The last two mechanisms are rather straightforward and will not be discussed further.

Upstream from the cooling section, directly after dilution, KCl will be present as a vapor due to the high temperature of the dilution gas. When the aerosol is transported down the probe it will be cooled by the walls. As the gas temperature drops below 400°C, the vapor pressure of KCl is close to zero and the KCl will be present as solid phase material. There are two competing routes for the condensing material. Firstly, the vapors might condense on the internal surfaces of the probe. Secondly, the gaseous KCl might undergo gas-to-particle formation by nucleation, coagulation, and particle surface condensation, thereby contributing to the total aerosol particle mass. Gas-to-particle conversion by condensation will occur only in volumes where the KCl saturation ratio (the ratio of partial pressure to vapor pressure) exceeds unity, and homogenous nucleation is expected to place at nucleation fronts where the saturation ratio is much higher than unity. From the results given in Figure 3b, it is clear that when using low dilution ratios, homogenous nucleation is the dominating gas-to-particle route, and that only a small fraction of the KCl will deposit on the SiO<sub>2</sub> particles. According to the classical nucleation theory, the rate of particle formation  $J$  (m<sup>-3</sup> s<sup>-1</sup>) is given by (Seinfeld and Pandis 1998)

$$J = \left( \frac{2\sigma}{\pi m_1} \right)^{1/2} \frac{v_1 N_1^2}{S} \exp \left( - \frac{16\pi v_1^2 \sigma^3}{3(k_B T)^3 (\ln S)^2} \right) \quad [1]$$

where  $\sigma$  (J m<sup>-2</sup>) is the surface tension;  $m_1$  (kg) and  $v_1$  (m<sup>3</sup>) are the molecular mass and volume, respectively;  $N_1$  (m<sup>-3</sup>) is the concentration of monomers;  $S$  is the saturation ratio;  $k_B$  (J K<sup>-1</sup>) is Boltzmann's constant; and  $T$  (K) is the gas temperature.

When the dilution ratio is increased, the KCl vapor concentration, and consequently also the saturation ratio, will be decreased at any specific position upstream from the nucleation front. As indicated by Equation (1), the nucleation rate, and therefore also the position of the nucleation front, has a strong dependence on the saturation ratio. Consequently, the nucleation front will be displaced and nucleation will take place at lower temperatures as the dilution ratio is raised. This will allow for a larger fraction of the vapor to condense onto the walls of the probe, diminishing the fraction available for particle formation.

In order to estimate the position of the nucleation front, the axial temperature profile in the inlet tube and the cooling tube was measured using a thermocouple inserted in the probe. The axial temperature profile along the dilution probe center is given in Figure 4. Varying the dilution ratio had only minor effects on the temperature profile, since most of the heat transport in and out of the dilution probe was through the probe walls.

The zero position in the figure corresponds to the entrance of the cooling tube and the -5 cm position to the probe inlet. The temperature measurements are approximate because the thermocouple is exposed to radiation exchange with the surrounding surfaces. For simplicity, no radial temperature gradient is assumed and the tube wall is regarded as a concentration sink. In the laboratory experiments, when adding 20 mg/m<sup>3</sup> of KCl in the reactor it might be assumed that a nucleation front in the

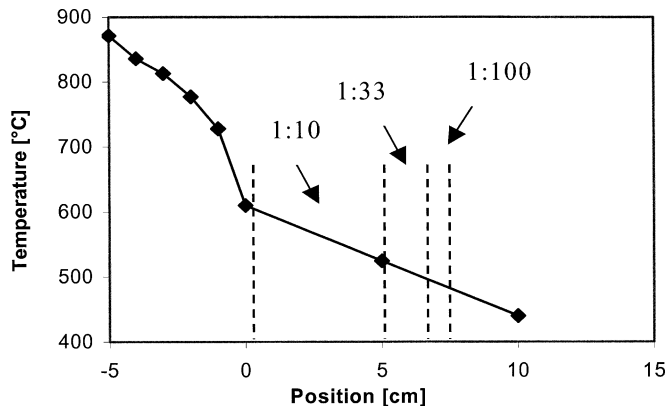


**Figure 4.** Axial temperature distribution in the dilution probe. The given position is from the tip of the cooling section. The positions between the dashed lines correspond to positions where the saturation ratio of 1–30 might be expected.

dilution probe will appear at a position in the cooling section where the saturation ratio is between 1 and 30. This was calculated from thermodynamic data to correspond to a position 0–5 cm in the cooling section, when a dilution ratio of 1:10 was used, and assuming that all KCl vapor is transported to the nucleation front. For dilution ratios of 1:33 and 1:100, the nucleation front would appear at slightly lower temperatures in the 5–7 cm and 7–8 cm sections, respectively. The assumed positions of the nucleation fronts are very close, especially for the two highest dilution ratios used. Now, all KCl vapor will not be transported to the nucleation front, but a fraction will condense on the cooled probe walls. Assuming that the walls are perfect sinks, the fraction of KCl vapor penetrating to the nucleation front may be approximated by the expression (Willeke et al. 1993)

$$\eta_{diff} = \exp \left( - \frac{\pi d L V_{diff}}{Q} \right) \quad [2]$$

where  $d$  is the diameter of the tube,  $L$  is the nucleation front position,  $V_{diff}$  is the deposition velocity, and  $Q$  is the volumetric flow. Since the estimated positions of nucleation fronts for the dilution ratios used are very close, the fraction of material available for nucleation should be similar, at least for the two highest dilution ratios used. This is opposed by the experimental results, where it seems that nucleation is actually completely suppressed when a dilution ratio of 1:100 is used, and there must be some other mechanism to account for this effect. According to Equation (1), the nucleation rate in the probe is thermodynamically determined mainly by the saturation ratio in the exponential term. However, since the initial vapor concentration is very low, and the cooling rate is high, the nucleation might be determined not only thermodynamically but also by the collision frequency of the monomers and clusters formed. In the collision-controlled regime, the nucleation rate and consequently also the nucleation front position will be more linearly dependent on concentration.

Therefore, the fraction of material available for particle formation at the nucleation front will be inversely dependent on the exponential of the inlet concentration according to Equation (2). This is more in line with the experimental results obtained.

There are probably several options of optimizing the sampling method in order to control the deposition and nucleation process better. These options include changing the probe design and flow conditions. They also include optimizing axial and radial temperature distributions. Probe design, flow conditions, and rates of mass-heat transport are complexly and strongly coupled properties, and any optimization will be facilitated by a more thorough analysis of the transport phenomena and aerosol dynamics involved. The system also needs to be calibrated for particle-size-dependent losses in order to establish a truly quantitative method. However, optimization and calibration is not within the scope of this investigation.

When sampling hot aerosols with high humidity, or gases containing volatile and semivolatile compounds, dilution is often used in order to avoid condensation. This is accomplished by decreasing the partial pressure of the vapors to assure that the saturation ratio is kept below unity, also after cooling the gas. It should be stressed that this mechanism is not at hand for avoiding condensation of most fly ash precursors because the vapor pressure of, e.g., KCl, is close to zero below 400°C.

### Results from Field Measurements

The flue gas was sampled at 780°C in the CFB boiler using low and high dilution ratios of 1:6 and of 1:60, respectively. The number and mass size distributions using the two different dilution ratios (corrected for dilution) are shown in Figure 5. The high dilution ratios (1:60) needed for suppression of the nucleation mode in the CFB boiler was slightly lower than what was used in the laboratory experiments (1:100). This was probably an effect of a lower inorganic vapor concentration in the boiler than what was used in the experimental setup. In fact, the main problem during the field measurements was not to suppress the nucleation mode but to produce it by using a sufficiently low dilution ratio. Probably a more distinct nucleation mode would have appeared if a dilution ratio lower than 1:6 could have been

used. However, a lower dilution ratio was prevented by the high water content of the flue gas, because lower dilution ratios would have caused condensation of water in the sampling line.

One alternative to produce the nucleation mode is to use a porous dilution probe for the low dilution sampling. In the porous dilution probe the gas is cooled and diluted through the walls of a sintered tube, and the losses to the walls are minimized. A setup with parallel sampling lines including a high-dilution probe and a porous dilution probe will probably facilitate the investigation of the particle-vapor distribution, especially the quantitative analysis.

The number concentration for the high dilution sample was  $1.2 \times 10^7$  particles/cm<sup>3</sup>, the GMD was 68 nm, and the GSD was 1.47. When using the low dilution, a nucleation mode around 40 nm was generated and the number concentration was  $2.2 \times 10^7$  particles/cm<sup>3</sup>. The GMD was 52 nm and the GSD was 1.61. The mass size distribution given by the gravimetric analysis of the DLPI substrates are not highly accurate due to the small mass of the particles deposited on the substrates, especially during the high dilution sampling. Nevertheless, the DLPI results are consistent with the SMPS results, and the nucleation mode is exposed as an enhanced mass on the first impactor stage ( $d_{ae} = 40$  nm) when using the low dilution ratio. The total fine particle mass concentration ( $d_{ae} < 1000$  nm) was 7.7 mg/m<sup>3</sup> when using the high dilution ratio, and 9.2 mg/m<sup>3</sup> when using the low dilution ratio. The total particle mass was also calculated from the SMPS data, using an effective particle density of 2 g/cm<sup>3</sup>. The calculated mass concentration was 8.8 mg/m<sup>3</sup> and 10.3 mg/m<sup>3</sup> for the low and high dilution ratios, respectively. The nucleation mode appearing during the low dilution sampling is most probably formed from vapors nucleating in the dilution probe. When the high dilution ratio is used, the main part of the vapors will deposit on the internal walls of the probe, and the result is more correctly representing the actual particle size distribution in the hot flue gas inside the boiler. The concentration of the condensing material seems to be much lower than what would be expected for wood-based fuels at 780°C, i.e., alkali chlorides present as vapors. This is most likely an effect of the high sulphur content in the fuel, which will favor the formation of alkali

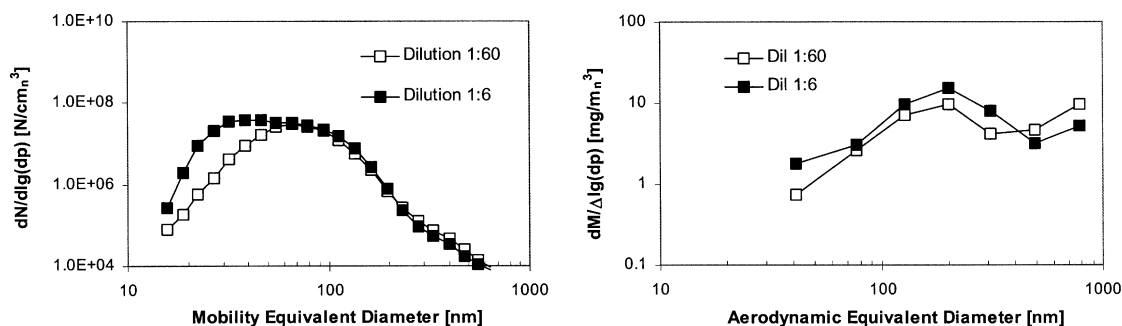


**Figure 5.** Particle number size distributions and mass size distributions of flue gas from the CFB boiler, using two different dilution ratios.

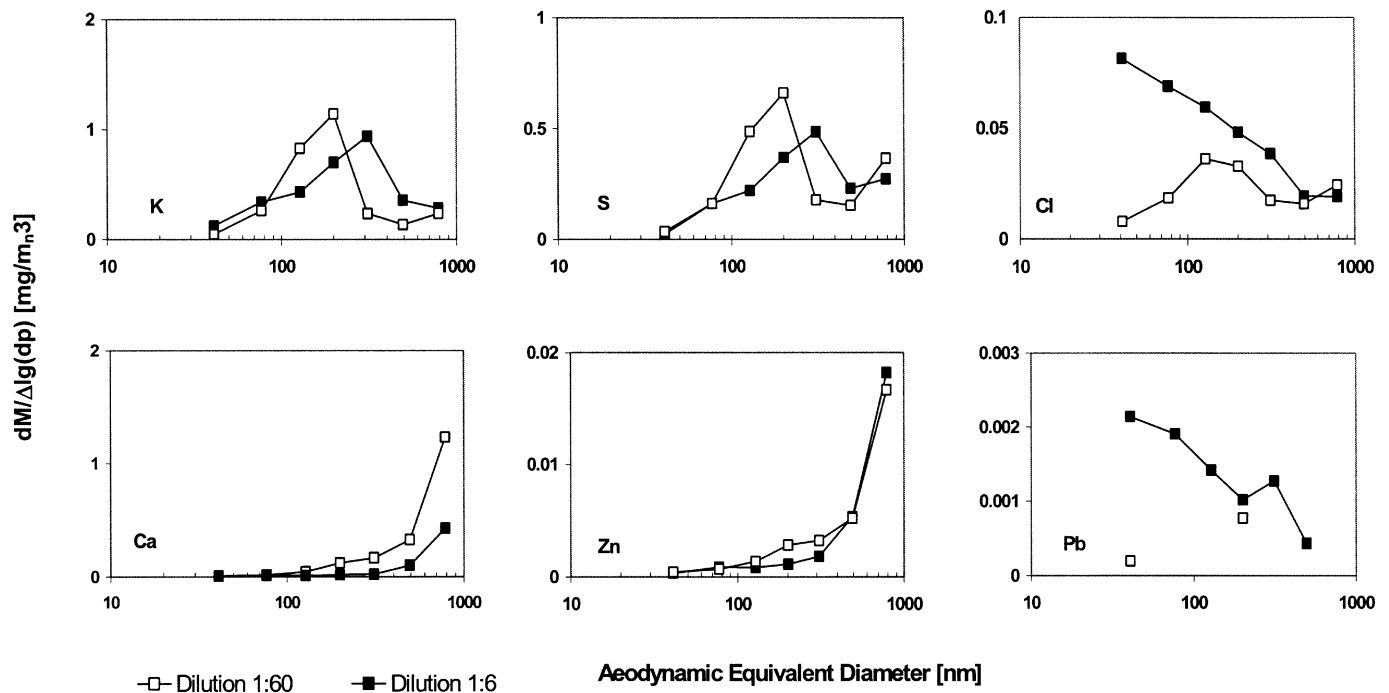


**Figure 6.** Elemental mass size distributions of the flue gas from the CFB boiler, using two different dilution ratios.

sulphates that have a much lower vapor pressure at 780°C than the corresponding chlorides.

The elemental mass size distribution as given by PIXE analysis of the impactor substrates is shown in Figure 6. When using the high dilution ratio (1:60), the elemental size distributions can be sorted into two types. The first one is represented by the distribution of K, S, Cl, and possibly Pb, where the mass is concentrated in a single mode around 200 nm. This type of elemental size distribution indicates that the elements contribute to the particle phase by gas-to-particle conversion inside the boiler, upstream from the probe position. The unimodal distribution, i.e., the absence of any nucleation mode, also indicates that there was no nucleation of these elements close to sampling position. The second distribution type is represented by the distribution of Ca and Zn, where the elemental mass is increasing monotonously with particle size in the submicron size range, indicating a single mode in the supermicron range. This type of size distribution indicates that the elements are mainly associated with a supermicron fraction of refractory components that were not vaporized during the combustion process, but transported through the boiler as fly ash particles.

When changing to the low dilution ratio (1:6), the elemental size distribution for K, S, Ca, and Zn were unaltered, showing that the major fraction of these elements were present as particles at the sampling position. In contrast, the Cl and Pb size distributions changed dramatically, indicating a nucleation mode that was formed from vapors nucleating inside the probe. The results suggest that more than half of the Cl and almost all Pb was

present as inorganic vapors at the sampling position. According equilibrium calculations made using a commercial software (HSC Chemistry, Outokumpu Research Oy, Pori, Finland), Cl should be present as alkali chloride vapors or HCl gas at 780°C, and the relatively high fraction of Cl in the particle phase was not anticipated. Further investigations are needed in order to establish if Cl might be associated with some other elements, e.g., calcium, which might form submicron particles by gas-to-particle conversion at higher temperatures.

## CONCLUSIONS

The objective of this study was to design and experimentally examine a sampling method for high-temperature aerosols from biomass combustion in which nucleation and condensation from gas-to-particle phase is avoided. The sampling method included a high-temperature dilution probe in which the sampled gas is diluted and then cooled. Experimental results from sampling of an aerosol with a known concentration of SiO<sub>2</sub> particles and KCl vapor, showed that when using a high dilution ratio the KCl vapor was effectively separated from the aerosol by condensation onto the cooled probe walls. When a lower dilution ratio was used, the KCl vapor generated a nucleation mode. The sampling method was also used in a CFB boiler fired with forest residues. The results indicated that the major fraction of Ca, K, S, and Zn were present as particles at 780°C, whereas substantial fractions of Cl and Pb were present as gases. These results are in line with previous experimental and theoretical results, and indicate that

the method can be used for efficient and precise characterizing of high-temperature combustion aerosols containing inorganic vapors. The method allows for measurements of transients using online instruments as well as for extracting time-averaged samples using filters and impactors.

## REFERENCES

- Baxter, L. L., Miles, T. R., Jenkins, B. M., Milne, T., Dayton, D., Bryers, R. W., and Oden, L. L. (1998). The Behavior of Inorganic Material in Biomass-Fired Power Boilers: Field and Laboratory Experiences, *Fuel Proc. Technol.* 54:47–78.
- Christensen, K. A., Stenholm, M., and Livbjerg, H. (1998). The Formation of Submicron Aerosol Particles, HCl and SO<sub>2</sub> in Straw-Fired Boilers, *J. Aerosol Sci.* 29:421–444.
- Flagan, R. C., and Seinfeld, J. (1988). *Fundamentals of Air Pollution Engineering*, Englewood Cliffs, New Jersey, Prentice Hall.
- Hasler, P., and Nussbaumer, T. (1998). Particle Size Distribution of the Fly Ash from Biomass Combustion, *Biomass for Energy and Industry, 10th European Conference and Technology Exhibition*, 8–11, June, Wurtsburg, Germany, 1330–1333.
- Kittelson, D. B. (1998). Engines and Nanoparticles: A Review, *J. Aerosol Sci.* 29:575–588.
- Kittelson, D. B., and Abdul-Khalek, I. (1999). Formation of Nanoparticles During Exhaust Dilution, *EFI Members Conference: Fuels, Lubricants Engines, & Emissions*, 18–20, January.
- Lighty, J. S., Veranth, J. M., and Sarofim, A. F. (2000). Combustion Aerosols: Factors Governing Their Size and Composition and Implications to Human Health, *J. Air Waste Manag. Assoc.* 50:1565–1618.
- Michelsen, H. P., Frandsen, F., Dam-Johansen, K., and Larsen, O. H. (1998). Deposition and High Temperature Corrosion in a 10 MW Straw Fired Boiler, *Fuel Proc. Tech.* 54:95–108.
- Miles, T. R., Baxter, L. L., Bryers, R. W., Jenkins, B. M., and Oden, L. L. (1996). Boiler Deposits from Firing Biomass Fuels, *Biomass Bioenergy* 10:125–138.
- Obernberger, I., Brunner, T., and Jöller, M. (2001). Characterisation and Formation of Aerosol and Fly-Ashes from Fixed-Bed Biomass Combustion, *International IEA Seminar* 27 June 2001, Zurich, Switzerland.
- Pagels, J., Strand, M., Rissler, J., Szpila, A., Gudmundsson, A., Bohgard, M., Lillieblad, L., Sanati, M., and Swietlicki, E. (2003). Characteristics of Aerosol Particles Formed During Grate Combustion of Moist Forest Residue, *J. Aerosol Sci.* 34:1043–1059.
- Seinfeld, J., and Pandis, S. (1998). *Atmospheric Chemistry and Physics*, John Wiley & Sons, Inc., New York.
- Strand, M., Pagels, J., Szpila, A., Gudmundsson, A., Swietlicki, E., Bohgard, M., and Sanati, M. (2002). Fly Ash Penetration Through Electrostatic Precipitator and Flue Gas Condenser in a 6 MW Biomass Fired Boiler, *Energy Fuels* 16:1499–1506.
- Valmari, T., Kauppinen, E. I., Kurkela, J., Jokiniemi, J. K., Sfiris, G., and Revitzer, H. (1998). Fly Ash Formation and Deposition During Fluidized Bed Combustion of Willow, *J. Aerosol Sci.* 29:445–459.
- Valmari, T., Lind, T. M., Kauppinen, E. I., Sfiris, G., Nilsson, K., and Maenhaut, W. (1999a). Field study on Ash Behavior During Circulating Fluidized-Bed Combustion of Biomass. 1. Ash Formation, *Energy Fuels* 13:379–389.
- Valmari, T., Lind, T. M., Kauppinen, E. I., Sfiris, G., Nilsson, K., and Maenhaut, W. (1999b). Field Study on Ash Behavior During Circulating Fluidized-Bed Combustion of Biomass. 2. Ash Deposition and Alkali Vapor Condensation, *Energy Fuels* 13:390–395.
- Willeke, K., and Baron, P. (1993). *Aerosol Measurement: Principles, Techniques, Applications*, John Wiley & Sons, New York.